Karlsruhe Institute of Technology

Faculty of Physics
Institute of Experimental Particle Physics

Model Building and Search for keV-Scale Sterile Neutrinos with the KATRIN-Experiment

Master Thesis of

Leonard Köllenberger

at the Department of Physics
Institute of Experimental Particle Physics (ETP)

Reviewer:	Prof. Dr. G. Drexlin (KIT)
Second Reviewer:	Prof. Dr. S. Mertens (MPP)
Advisor:	M.Sc. A. Huber (KIT)
Second advisor:	M.Sc. M. Korzeczek (KIT)

28th of February 2018 – 1st of March 2019

Erklärung zur Selbstständigkeit

Ich versichere wahrheitsgemäß, die Arbeit selbständig verfasst, alle benutzten Hilfsmittel vollständig und genau angegeben und alles kenntlich gemacht zu haben, was aus Arbeiten anderer unverändert oder mit Änderung entnommen wurde sowie die Satzung des KIT zur Sicherung guter wissenschaftlicher Praxis in der jeweils gültigen Fassung beachtet zu haben. (Nach der Studien- und Prüfungsordnung 2015 für den Masterstudiengang Physik, §14 Absatz 5)

Karlsruhe, den August 30, 2019, _____

Leonard Köllenberger

Als Prüfungsexemplar genehmigt von

Karlsruhe, den August 30, 2019, _____

Prof. Dr. G. Drexlin

Abstract

The KArlsruhe TRItium Neutrino experiment (KATRIN) is designed to determine the effective neutrino mass by kinematic measurements of the endpoint of the tritium β-spectrum, with a sensitivity of 200 meV at a 90 % CL. Extending the measuring range, the KATRIN experiment can also be used to search for keV-scale sterile neutrinos.

Sterile neutrinos in the keV-range are a well motivated extension of the standard model and present a promising candidate for dark matter. Modelindependent measurements of the sterile neutrino mass and mixing amplitude therefore have a major impact in astro- and particle physics. Within the tritium spectrum, sterile neutrinos would be manifested as a kink in the spectrum. The kink position corresponds to the sterile neutrino mass m_{heavy} and is contributing to the spectrum with the mixing amplitude $\sin^2(\theta)$.

In June 2018, during the "first tritium" campaign, the KATRIN experiment was tested and operated with tritium for the first time. Furthermore, first dedicated sterile neutrino measurements down to 4 keV below the endpoint were performed. The main focus of this work is the analysis of these dedicated sterile neutrino measurements, using the custom analysis tool Fitrium. Data quality and data selection is discussed and energy dependent corrections for the detection efficiency are included in the final analysis.

Sensitivity studies are presented, determining the statistical sensitivity that can be expected from the measured data. Furthermore, the effects of systematic uncertainties are discussed, identifying the uncertainty on the DT-concentration as a major systematic uncertainty. Finally a sensitivity study of possible further measurements, assuming the same systematics and an effective measurement time on the order of days is shown.

Based on the measured data, an exclusion limit is presented for the single runs, as well as when stacking the data of the two runs. Analysing single runs results in an exclusion limit down to a mixing angle of $\sin^2(\theta)_{\mathrm{min}} \approx 1.4 \times 10^{-2}$ at $\nu_{\mathrm{heavy}} \approx 1.3\,\mathrm{keV}$ with a 90 % CL. When stacking the runs an exclusion limit with a minimum mixing angle of $\sin^2(\theta)_{\mathrm{min}} \approx 0.9 \times 10^{-2}$ at $\nu_{\mathrm{heavy}} \approx 1.3\,\mathrm{keV}$ can be achieved with a 90 % CL. The analysis has shown that with a measurement time of only $\sim 3\,\mathrm{h}$ of dedicated sterile neutrino measurements, a limit comparable to other experiments can already be achieved.

An additional part of this thesis concerns a new convolutional approach describing the measured tritium spectrum in an extended energy range. In the SSC-sterile model, various experimental components and effects are described via response matrices. In this work, the detector response matrix, as well as a response matrix describing the backscattering, are derived and presented.

Zusammenfassung

Das KArlsruhe TRItium Neutrino Experiment (KATRIN) ist ausgelegt um durch Präzisionsmessungen des Tritium β-Zerfallspektrums die effektive Neutrino Masse mit einer bisher unerreichten Sensitivität von 200 meV (90 % CL) zu bestimmen. Durch Erweiterung des Messbereichs und Anpassung der Quellstärke, bietet das KATRIN-Experiment darüber hinaus die Möglichkeit, nach sterilen Neutrinos im keV-Bereich zu suchen.

Rechtshändige sterile Neutrinos sind eine minimale Erweiterung des Standard Modells, mit der sich die kleine Masse der Neutrinos erklären lässt. Sterile Neutrinos im keV-Massenbereich sind zudem ein vielversprechender Kandidat für Dunkle Materie. Eine modellunabhängige Bestimmung der sterilen Neutrino Parameter in einem Laborexperiment ist somit von großer Bedeutung für die Teichen- und Astrophysik. Der Einfluss von Sterile Neutrinos würde sich bei Messungen des Tritium Spektrums als ein Knick im Spektrum offenbaren, wobei die Position des Knicks direkt mit der Masse des sterilen Neutrinos m_{s} in Verbindung gebracht werden kann, sowie die Stärke des zusätzlichen Signals mit der Mischungsamplitude $\sin^2(\theta)$.

Im Juni 2018 wurde das KATRIN-Experiment während der „First Tritium" Kampagne das erste Mal mit Tritium in der Quelle in Betrieb genommen und getestet. Neben ersten Messungen des Tritium Spektrums im Bereich des Endpunktes, wurden zusätzlich spezielle Messungen für sterile Neutrinos bis 4 keV unter den Endpunkt durchgeführt. Ein Schwerpunkt dieser Arbeit is die Analyse dieser tiefen Messungen des Spektrums mithilfe des speziell für KATRIN entwickelten Fitrium Softwarepakets. In dieser Arbeit wird zusätzlich die Datenqualität, sowie die Datenauswahl diskutiert. In den Analysen werden Energie und Pixel abhängige Korrekturen der Detektionseffizienz berücksichtigt.

Sensitivitätsstudien werden vorgestellt, basierend auf den Messeinstellungen. In weiteren Studien, wird zudem der Einfluss von systematischen Unsicherheiten beschrieben, wobei sich die Unsicherheit auf die DT-Konzentration als einer der Maßgeblichen Systematiken identifizieren lässt.

Auf Grundlage der zwei dedizierten sterilen Neutrino Messungen, werden für beide einzelnen Messungen Ausschlussgrenzen gezeigt, wobei ein minimaler Mischungswinkel von $\sin^2(\theta)_{\mathrm{min}} \approx 1.4 \times 10^{-2}$ bei $\nu_{\mathrm{heavy}} \approx 1.3\,\mathrm{keV}$ mit einem 90 % CL ausgeschlossen werden kann. Eine kombinierte Analyse beider Messungen, liefert einen minimalen Mischungswinkel von $\sin^2(\theta)_{\mathrm{min}} \approx 0.9 \times 10^{-2}$ bei einer sterile Neutrino Masse von $\nu_{\mathrm{heavy}} \approx 1.3\,\mathrm{keV}$, mit einem 90 % CL.

Die Analyse zeigt, dass sich bereist mit nur etwa 3 h Messzeit Ausschlussgrenzen erzielen lassen, die vergleichbar mit anderen Experimenten sind. Durch Erhöhung der effektive Messzeiten zu Tagen, lassen sich somit mit dem KATRIN-Experiment bereits in der aktuellen Konfiguration neue Ausschlussgrenzen auf die sterilen neutrino Parameter setzen.

Ein weiterer teil der Masterarbeit ist verbunden mit dem SSC-Sterile Modell. Das SSC-Sterile Modell, konzipiert für sterile Neutrinos, wurde entwickelt um das gemessenen Tritium Spektrum des KATRIN-Experiments zu beschreiben. Das Modell basiert auf einer Faltung verschiedener physikalischer Effekte mit dem theoretischen Tritium β-Spectrum. Physikalische Effekte lassen sich einzeln betrachten und werden durch Response-Matrizen im Modell berücksichtigt. Im Zuge dieser Arbeit wird die den Detektor beschreibende Response-Matrix berechnet. Weiterhin wird eine Response-Matrix vorgestellt, die das Spektrum von Elektronen beschreibt, die vom Detektor zurückgestreut werden.

Contents

Abstract v

Zusammenfassung vii

1 Introduction 1

2 Neutrino physics 3

2.1 History of neutrino physics . . . 3
2.2 Neutrinos in the standard model . . . 4
2.3 Neutrino oscillation . . . 6
2.4 Neutrino mass generation . . . 10
2.5 Neutrino mass determination . . . 12
2.6 Neutrino dark matter . . . 16
2.7 keV-scale sterile neutrinos and their imprint on the β-spectrum . . . 18

3 The KATRIN experiment 21

3.1 Working principle of a MAC-E filter . . . 21
3.2 Setup of the KATRIN experiment . . . 23
3.2.1 Source and Transport Section (STS) . . . 23
3.2.2 Spectrometer and detector section (SDS) . . . 26
3.3 The TRISTAN project . . . 29

4 Search for keV-scale sterile neutrino in "first tritium" at KATRIN 31

4.1 Challenges finding keV-scale sterile neutrinos . . . 31
4.2 "First tritium" campaign . . . 32
4.3 Physics model . . . 33
4.3.1 The β-decay model . . . 33
4.3.2 Source and spectrometer response . . . 34
4.3.3 Detector response . . . 37
4.4 Analysis strategy . . . 38
4.4.1 Likelihood estimation and minimisation . . . 38
4.4.2 Fitrium software . . . 39

4.4.3 Exclusion limit settings . . . 40
4.5 Systematic uncertainties . . . 40
4.5.1 Uncertainty of the pixel dependent detection efficiency . . . 40
4.5.2 Scale of uncertainties . . . 45
4.5.3 Treatment of uncertainties . . . 46
4.6 Results . . . 49
4.6.1 Sensitivity of KATRIN based on Monte Carlo . . . 51
4.6.2 Exclusion based on data . . . 52
4.6.3 Influence of systematics . . . 53
4.7 Outlook . . . 54

5 Convolutional model for KATRIN - SSC-sterile 57
5.1 SSC-sterile model . . . 57
5.2 Detector response . . . 59
5.3 Backscattering response . . . 61
5.4 Outlook . . . 61

6 Conclusion and outlook 63

Appendix 65

List of acronyms 74

List of figures 76

List of tables 77

Bibliography 79

1. Introduction

Experiments have shown, that neutrinos oscillate between their flavour eigenstates [27, 68], proving that the neutrino possesses a non-zero mass in contradiction to the standard model.

Based on cosmological observations, which are strongly depending on the underlying model, the current limit on the neutrino mass is given by $\sum m_{\nu_i} \leq 0.11\,\text{eV} - 0.72\,\text{eV}$, with a 95 % CL [54]. So far laboratory experiments were only able to give an upper limit on the effective electron antineutrino mass of $m_{\nu_e} < 2\,\text{eV}$, such as given by the Mainz and Troitsk experiments [19, 76]. Determining the neutrino mass via measurements of β-decay spectra are providing stringent model independent results.

Measuring the β-decay spectrum of tritium, the KArlsruhe TRItium Neutrino experiment (KATRIN) is designed to deliver an unprecedented sensitivity of 200 meV at a 90 % CL for measuring the neutrino mass in a laboratory experiment [71]. Hence providing a better sensitivity by one order of magnitude. The KATRIN experiment has been commissioned and first measurements with reduced tritium concentration have been successfully performed during the "first tritium" campaign in June 2018. The KATRIN collaboration is currently preparing for tritium measurements, using the full source strength, with an exceptional decay rate of $\sim 10^{11}$ decays/s [78], planning to reach the 1 eV limit by the end of this year.

The KATRIN experiment, in addition to measuring the neutrino mass, also fulfils the requirements to be able to measure sterile neutrinos within the tritium spectrum, when measuring in lower energy ranges. By utilising the current setup with adapted settings, it is already possible to get a first insight deeper into the spectrum. To be able to take advantage of the full source activity in the whole energy range, a new detector system is needed. For this purpose a new detector and readout system is currently being developed. High statistics sterile neutrino measurements are further planed in the future, by extending the KATRIN experiment with the new TRISTAN (tritium beta decay investigation on sterile to active neutrino mixing) detector and readout system. These sterile neutrino measurements are planned to follow the neutrino mass measurements, prospectively in 2025 [84].

The focus of this work is on measurements of keV-scale sterile neutrinos. The standard model, as it is today, does not explain the comparably small mass scale of neutrinos. Thus extensions are needed to be able to explain this phenomenon. By introducing sterile neutrinos to the standard model, it is possible to explain the small mass scale of neutrinos. Furthermore, sterile neutrinos in the keV mass-scale are a promising candidate for dark matter, because they would contribute significant mass content to the universe.

During the "first tritium" campaign first dedicated keV-scale neutrino measurements have been performed. The main focus of this work is the analysis of these dedicated measurements, measuring 4 keV into the spectrum, including studies of the effects of statistical and systematic uncertainties on the sensitivity. For sterile neutrino search, it

is important to be able to precisely describe the spectrum in the whole energy range. Therefore an alternative approach combining different effects via convolution of different responses is currently being developed, called SSC-sterile. An additional component of this work is the calculation and construction of a model describing the detector response included in the SSC-sterile model.

The work presented here is structured as follows: In chapter 2 an overview to the topic of neutrino physics and cosmology, with focus on dark matter, followed by an introduction to sterile neutrinos is given. In chapter 3 the working principle of the KATRIN experiment is outlined, as well as a more detailed description of its components. Furthermore the TRISTAN detector will be presented, giving an outlook on sterile neutrino measurements with KATRIN in the future. In chapter 4, first dedicated sterile neutrino measurements during the "first tritium" campaign are described and analysed, giving first insight on the potential of the KATRIN experiment measurements of sterile neutrinos. Comparing the measured data to sensitivity studies, effects of statistical and systematic uncertainties are discussed. In chapter 5 an alternative convolutional approach of model building that could be applied when looking deeper into the spectrum is described. The detector response will further be explained more in detail.

This work is a first step on the way to the determination of an exclusion limit on the sterile neutrino parameters. Furthermore a first outlook on future sterile neutrino measurements with the KATRIN experiment and the subsequent future with the TRISTAN detector is given.

2. Neutrino physics

Neutrino physics is one of the most relevant topics in current particle physics research. Since its conceptual proposal 89 years ago by Pauli [92], there are still unanswered questions regarding the nature of neutrinos - such as their mass - leading to physics beyond the standard model. As neutrinos could play a significant role in the structural formation of the universe, it is crucial to get insight into their nature and properties, to construct and refine the cosmological model from the Big Bang to today. The following sections introduces the discovery of neutrinos, the mechanism of mass generation and neutrino oscillation, as well as various possibilities to determine the neutrino mass. The current standard model of particle physics still has two major flaws: The neutrino is massless and there are right handed partners to every particle, except the neutrinos. By introducing right handed neutrinos to the standard model, the neutrino mass generation can be explained. Furthermore these right handed sterile neutrinos are potential candidates for dark matter, influencing the structural formation of the universe. Therefore, subsequently the idea of a heavy sterile neutrino is introduced and the effects of sterile neutrinos are discussed.

2.1 History of neutrino physics

The first radioactive decays were observed in 1896 by H. Becquarel [18] and later distinguished by E. Rutherford and F. Soddy into three types of radiation: α-, β- and γ-radiation [102]. In 1914 J. Chadwick was able to measure the β-spectrum of radium with a detector developed by H. Geiger in 1908, today known as a Geiger counter.

Until then, it was thought that the β-decay was a two body decay, which would result in a characteristic mono energetic spectrum similar to the α- spectrum. Contrary to the expectations, the measurements by J. Chadwick showed a continuous β-spectrum [25], which would result in a violation of energy conservation, according to the status of knowledge at that time.

The problem persisted unresolved until W. Pauli proposed the involvement of a new particle in a famous open letter to L. Maitner and the "Radioactive Ladies and Gentlemen" in 1930 [92]. With a third decay constituent he was able to explain the continuous spectrum.

$$ {}^{\mathrm{A}}_{\mathrm{Z}}\mathrm{X} \longrightarrow {}^{\mathrm{A}}_{\mathrm{Z+1}}\mathrm{Y} + \mathrm{e}^{-} + \overline{\nu}_{\mathrm{e}}. \tag{2.1} $$

Conservation of charge, energy, momentum, and spin lead to the proposal of a massive, neutral particle with spin $1/2$ which he called "neutron", thus explaining the β-decay spectral shape.

In 1932 J. Chadwick found a particle with neutral charge, in experimental measurements, as a nuclei constituent, with a similar mass to the protons mass which since then is known as the neutron [26]. Encouraged by Chadwick's experimental findings and W. Paulis theory

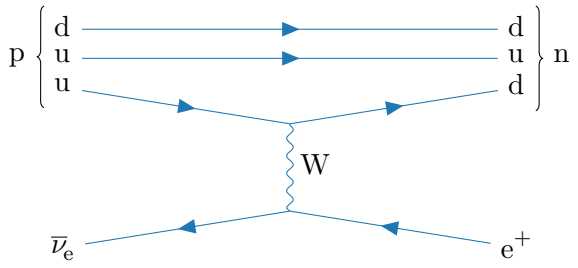

Figure 2.1: Feynman diagram of the inverse β-decay, where a proton (duu) interacts with an electron antineutrino ($\overline{\nu}_e$) via W-boson exchange, resulting in a neutron (ddu) and a positron (e^+).

of a massless neutral particle, E. Fermi was able to formulate a mechanism to explain the β-decay as a three body decay, as represented in equation 2.2. In Fermi's theory of the β-decay a heavy neutron (n) decays into a positive proton (p), an electron (e^-), and a massless neutral particle, the neutrino (ν). To be more precise into an electron antineutrino ($\overline{\nu}_e$).

$$n \longrightarrow p + e^- + \overline{\nu}_e. \tag{2.2}$$

To solve the name conflict with Chadwick's neutron, Fermi called the neutral particle neutrino, which means for "little neutral one" [43]. Pauli stated that neutrinos could likely not be detected experimentally, since they possess no electric charge and only interact via weak force. It took another 9 years for the first proposal of a possible mechanism to detect neutrinos in 1933. A method to detect the neutrino was the inverse β-decay, suggested by K. C. Wang in 1942 [114]. The mechanism is illustrated in figure 2.1, following

$$p + \overline{\nu}_e \longrightarrow n + e^+. \tag{2.3}$$

Subsequently, in an experimental setup by C. Cowan and F. Reines in 1956 the neutrino could be observed for the first time [98]. In the experiment, named Poltergeist Project in Los Alamos National Laboratory, an electron antineutrino is caught by a proton, which then decays into a neutron and a positron. The positron afterwards annihilates with an electron by producing a characteristic γ-ray, which then was detected. In these first experiments only electron antineutrinos were detected. It took another nine years until the existence of a different neutrino flavour, the muon neutrino ν_μ, was observed in 1962 by L. Lederman, M. Schwarz, and J. Steinberger in an experiment at the Brookhaven National Laboratory [29], which was rewarded with a physics Nobel Prize in 1988 [87]. The discovery was based on the π-meson decay into a muon μ and a muon neutrino ν_μ,

$$\pi \longrightarrow \mu + \nu_\mu. \tag{2.4}$$

In the experiment, the primary muons were absorbed by steel shielding, whereas the muon neutrinos passed the shielding and produced secondary muons in an aluminium target, which could be detected.

After the discovery of a third lepton, the τ-lepton in 1975, a third neutrino flavour was predicted. The tau neutrino ν_τ was indirectly detected, by the DONUT collaboration at Fermilab, proving its existence in 2001 [35].

2.2 Neutrinos in the standard model

The standard model (SM) of elementary particle physics is the state of the art model of particle physics. A graphical overview of the standard model is shown in figure 2.2. It

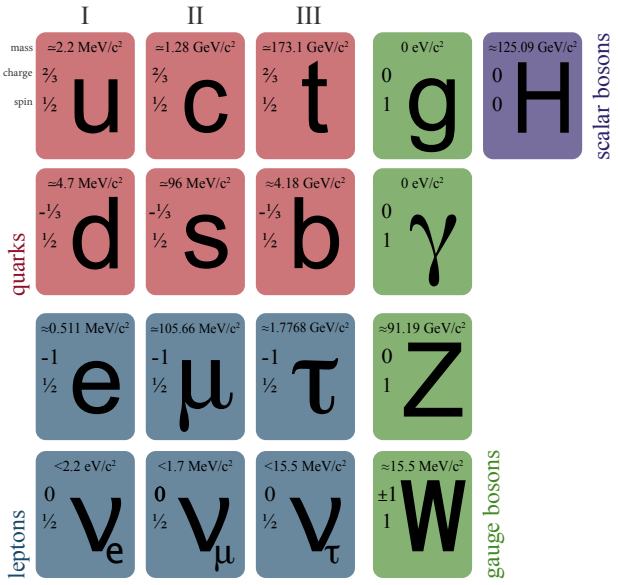

Figure 2.2: The standard model of elementary particle physics. Each tile contains the symbol for the according particle, as well as the spin, the charge, and the mass. The standard model can be divided into four groups. Quarks, listed in red and leptons, listed in blue. Both quarks and leptons can be distinguished into three generations depending on their mass. The third group contains the gauge bosons, coloured in green, which combines all spin 1 bosons. The only scalar boson, the Higgs boson, is highlighted in purple (figure adapted from [86]).

combines all known elementary particles and describes three fundamental interactions, the weak, the strong, and the electromagnetic interaction. The only force that is not described by the standard model is the gravitational force. The standard model can be described as a Lagrange density, invariant under $\mathrm{SU}(3)_C \times \mathrm{SU}(2)_{T_3} \times \mathrm{U}(1)_Y$ symmetry transformations. The theory combines the quantum chromodynamics $\mathrm{SU}(3)_C$ and the gauge group $\mathrm{SU}(2)_{T_3} \times \mathrm{U}(1)_Y$ for electroweak interactions, generated by the weak hypercharge, describing the weak interaction. Each symmetry corresponds to a conservational quantity, as stated by the Noether theorem. being the colour charge C, the weak isospin T_3, the hyper charge Y, and the electric charge.

All elementary particles of the standard model can be grouped into four categories, the quarks, the leptons, the gauge bosons, and the Higgs boson. Quarks and leptons are both fermions, which means their spin is of value $1/2$. Whereas bosons posses an integer spin value. Gauge bosons function as exchange particles of the fundamental interactions. Photons (γ) mediate electromagnetic interactions, $\mathrm{W}^{\pm}$- and Z^0-bosons mediate the weak force, and gluons (g) are the exchange particles of the strong force. The Higgs bosons (H) arises from spontaneous symmetry breaking of the Higgs field. Massive particles obtain their mass, by interactions with the Higgs field.

As the neutrinos have no colour charge, they are grouped as leptons. There are three generations of leptons, according to their masses. The leptons consist of charged leptons and neutrinos. Charged leptons are electrons (e^-), muons (μ^-), and tau leptons (τ^-). They form $\mathrm{SU}(2)_{T_3}$ doublets with their neutral lepton partners: the electron neutrino ν_e, muon neutrino ν_μ, and the tau neutrino ν_τ. For every particle in the standard mode, there exist an antiparticle with the same mass and opposite physical charges.

All interactions where neutrinos are involved are exclusively weak interactions, as they

do not carry a colour charge nor an electric charge. The weak force is mediated by $W^{\pm}$- and Z^0-bosons. These gauge bosons couple to left-handed particles and right-handed antiparticles.

In the Weinberg-Salam $SU(2)_{T_3} \times U(1)_Y$ theory [104, 115], combining the electromagnetic and the weak interaction, it is predicted that the three neutrino flavours are not expected to have a mass, as only a left handed component of the neutrino is employed in interactions, whereas a right handed component is preconditioned not to exist. Another constraint is, that the lepton number has to be conserved. Violating either of these conditions would lead to a neutrino mass different to zero [81]. Contrary to this is the observation of the neutrino oscillation, indicating a neutrino mass $m_\nu > 0$. As the standard model is not flawless, there are extensions, explaining the existence of the neutrino mass. The following sections will depict the mechanisms of neutrino mass generation and neutrino oscillation, as well as a possible Majorana[1] nature of neutrinos.

2.3 Neutrino oscillation

One of the pioneer experiments of neutrino physics was the Homestake experiment, in operation from 1970 to 1994 [27]. The experiment was designed to measure the total solar electron neutrino flux due to nuclear fusion in the sun. The experiment surprisingly showed that there were consistently only one third of the number of neutrinos which were expected from the CNO cycle, based on calculations by J. N. Bahcall [16]. These unexpected results caused unease in the community. Subsequently the Kamiokande-II experiment was able to independently reproduce the Homestake results. In 1988, T. Kajita and the Kamiokande-II collaboration released their results [68]. This lead to the construction of a number of subsequent experiments to solve the solar neutrino problem, such as Super-Kamiokande and SNO. In investigations by A. McDonald and the Sudbury Neutrino Observatory (SNO), the ν_e flux was also measured in ratio to the total solar neutrino flux, demonstrating the oscillation of neutrinos [107]. Both T. Kajita and A. McDonald were honoured with the physics Nobel Prize in 2015 "for the discovery of neutrino oscillations, which shows that neutrinos have mass" [88]. The experimental measurements of the neutrino oscillation will be described more in detail in section 2.3.

The first idea of neutrino oscillation had been proposed by B. Pontecorvo in 1957 [94]. He published a paper stating the possibility of neutrinos being a particle mixture and therefore an oscillation of neutrinos into antineutrinos might be possible.

A more advanced theory of neutrino oscillation was published by Z. Maki, M. Nakagawa, and S. Sakata in 1962 [80], proposing a flavour oscillation of the neutrino flavour eigenstates. In the model the three flavour eigenstates of weak interaction (ν_e, ν_μ, and ν_τ) form an orthonormal basis for the observable neutrino states of the standard model. The eigenbasis of these neutrino flavour eigenstates is given by the neutrino mass eigenstates (ν_1, ν_2, and ν_3), each with a discretely defined mass. Neutrinos are propagated in their mass eigenstates, while they interact in their flavour eigenstates. The relationship between flavour eigenstates and mass eigenstates is given by equation 2.5.

$$|\nu_i\rangle = \sum_\alpha U_{\alpha i} |\nu_\alpha\rangle \Leftrightarrow \begin{pmatrix} \nu_e \\ \nu_\mu \\ \nu_\tau \end{pmatrix} = \begin{pmatrix} U_{e1} & U_{e2} & U_{e3} \\ U_{\mu 1} & U_{\mu 2} & U_{\mu 3} \\ U_{\tau 1} & U_{\tau 2} & U_{\tau 3} \end{pmatrix} \cdot \begin{pmatrix} \nu_1 \\ \nu_2 \\ \nu_3 \end{pmatrix}, \tag{2.5}$$

[1] Majorana particles, are particles that are their own antiparticle at the same time. The most prominent Majorana particles is the photon.

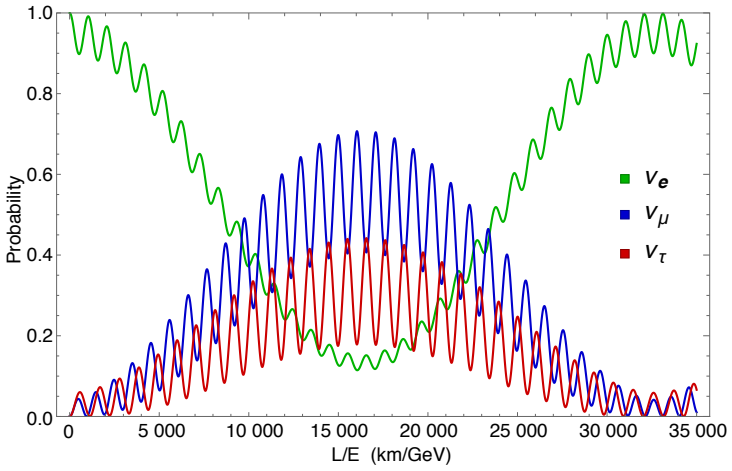

Figure 2.3: A depiction of the probability for neutrino oscillation. Starting with an electron neutrino (green), between $^{L}/_{E}$ ~11 000 kmGeV^{-1} and $^{L}/_{E}$ ~22 000 kmGeV^{-1} the probability is higher to observe a muon neutrino or a tau neutrino than an electron neutrino (figure adapted form [17]).

with the so called Pontecorvo-Maki-Nakagawa-Sakata-matrix (PMNS) U, describing the matrix propagation of the mass eigenstates. The PMNS-matrix is given by the product of a mixing between mass eigenstates ($|\nu_1\rangle \leftrightarrow |\nu_2\rangle$), ($|\nu_1\rangle \leftrightarrow |\nu_3\rangle$), and ($|\nu_2\rangle \leftrightarrow |\nu_3\rangle$), each given by a (3×3) matrix, resulting in

$$U = \begin{pmatrix} 1 & 0 & 0 \\ 0 & c_{23} & s_{23} \\ 0 & -s_{23} & c_{23} \end{pmatrix} \cdot \begin{pmatrix} c_{13} & 0 & s_{13}e^{-i\delta_{CP}} \\ 0 & 1 & 0 \\ -s_{13}e^{i\delta_{CP}} & 0 & c_{13} \end{pmatrix} \cdot \begin{pmatrix} c_{12} & s_{12} & 0 \\ -s_{12} & c_{12} & 0 \\ 0 & 0 & 1 \end{pmatrix} \tag{2.6}$$

$$= \begin{pmatrix} c_{12}c_{13} & s_{12}c_{13} & s_{13}e^{-i\delta_{CP}} \\ -s_{12}c_{23} - c_{12}s_{23}s_{13}e^{i\delta_{CP}} & c_{12}c_{23} - s_{12}s_{23}s_{13}e^{i\delta_{CP}} & s_{23}c_{13} \\ s_{12}s_{23} - c_{12}c_{23}s_{13}e^{i\delta_{CP}} & -c_{12}s_{23} - s_{12}c_{23}s_{13}e^{i\delta_{CP}} & c_{23}c_{13} \end{pmatrix}, \tag{2.7}$$

where $c_{ij} = \cos(\theta_{ij})$ and $s_{ij} = \sin(\theta_{ij})$, with the corresponding mixing angles θ_{ij} between the mass eigenstates ν_i and ν_j, and the CP-violating phase δ_{CP}.

The neutrino flavour eigenstate of a ν_e, starting at $t = 0$, changes over time [83]

$$|\nu_e(t > 0)\rangle = U^*_{e1}e^{-iE_1 t}\,|\nu_1\rangle + U^*_{e2}e^{-iE_2 t}\,|\nu_2\rangle + U^*_{e3}e^{-iE_3 t}\,|\nu_3\rangle \neq |\nu_e(t = 0)\rangle\,, \tag{2.8}$$

with a defined energy E_i corresponding to a momentum p_i. The probability P to find a neutrino ν_α with the flavour α in the flavour eigenstate ν_β after a certain amount of time t, can be calculated by projecting $|\nu_\alpha\rangle$ onto $|\nu_\beta\rangle$ [83]:

$$P(\nu_{\alpha\to\beta}(t)) = \left|\left\langle \nu_\beta \middle| \nu_\alpha(t) \right\rangle\right|^2 = \left|\sum_k U^*_{\alpha k}e^{-iE_k t}U_{\beta k}\right|^2 \tag{2.9}$$

$$= \sum_{k,l} U^*_{\alpha k}U_{\beta k}U_{\alpha l}U^*_{\beta l}e^{-i(E_k - E_l)t}. \tag{2.10}$$

In the ultra relativistic case, E_k can be approximated as $p = E$, which leads to the following

expression

$$P(\nu_{\alpha\to\beta}(L,E)) = \sum_{k,l} U^*_{\alpha k} U_{\beta k} U_{\alpha l} U^*_{\beta l} e^{-i\left(\frac{\Delta m^2_{kl}\cdot L}{2E}\right)}, \tag{2.11}$$

where L is the distance between the point of generation and observation, E is the corresponding energy, and $\Delta m^2_{kl} = m^2_k - m^2_l$ the squared mass difference between the mass eigenstates ν_k and ν_l. A visualisation for the changing probabilities due to the oscillation is illustrated in figure 2.3.

Neutrino mass hierarchy

There are two possible hierarchies for the neutrino mass eigenstates. While the absolute mass difference of the mass eigenstates was determined by a number of experiments, the absolute mass scale is still unknown. The mass hierarchy is also influenced by the sign of $\Delta m_{31(32)}$, which is unknown as well. There are two possible ordering scenarios for the mass eigenstates. The so called normal mass hierarchy ($m_{\nu_1} < m_{\nu_2} < m_{\nu_3}$) and the inverted mass hierarchy ($m_{\nu_3} < m_{\nu_1} < m_{\nu_2}$). Both mass hierarchies are illustrated in 2.4. The mass difference of the solar neutrino doublet (ν_1, ν_2) is referenced as $\Delta m_{\text{sol}} = \Delta m_{12}$ and the mass difference of the atmospheric neutrinos (ν_3) corresponds to $\Delta m_{\text{atm}} = \Delta m_{31(32)}$.

Measuring one of the eigenstates could reveal which hierarchy is correct. This underlines the importance and the urgency to measure the neutrino mass.

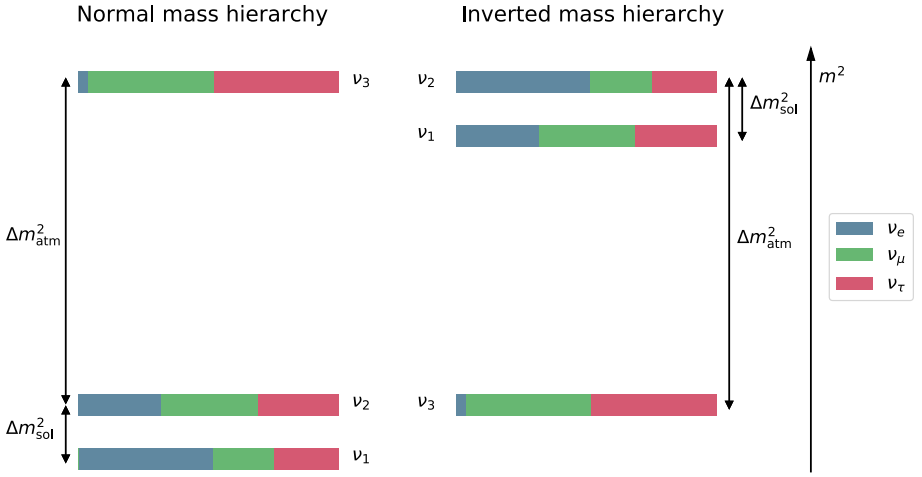

Figure 2.4: Graphical representation of the neutrino mass hierarchy, showing the two possible mass ordering scenarios. In the normal mass ordering (left) the sign of Δm^2_{31} is negative whereas in the inverted mass ordering (right) the sign is positive.

Experimental measurements of the neutrino oscillation parameters

In the beginning of section 2.3 it is described how neutrino oscillation was discovered historically. There are three ways to measure the neutrino oscillation and the corresponding neutrino oscillation parameters ($\sin^2(\theta_{ij})$ and Δm_{ij}). The measurements can be differentiated into detection of solar, atmospheric, or accelerator neutrinos.

Solar neutrinos originate from nuclear fusion processes in the sun. One of the primary reactions is the fusion of four protons into a helium nucleus, two positrons, and two electron neutrinos. The neutrinos generated are electron neutrinos, with an energy range of up to 15 MeV. Figure 2.5a shows an overview of the neutrino spectra from fusion processes in the

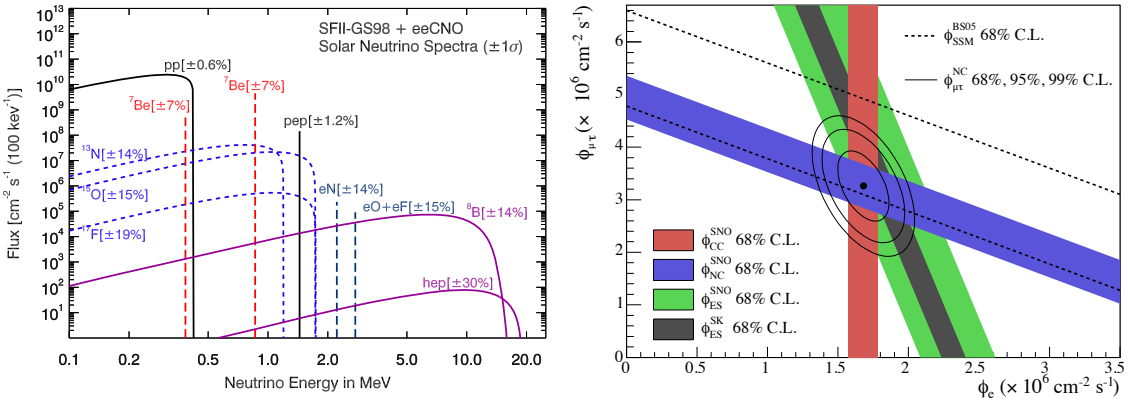

(a) Solar neutrino spectrum **(b)** Solar neutrino flux

Figure 2.5: (a) Solar neutrino spectrum of various fusion chains, given by the SFII-GS98 standard solar flux model [105]. Depending on the process, the neutrino spectrum is mono energetic or continuous. Each of the colours can be assigned to a fusion or decay process: pp chain (black), ^{7}Be chain (red), CNO cycle (blue), and ^{8}B chain (violet). **(b)** Combined results from SNO and Super-Kamiokande of the solar neutrino flux. The plot shows the $\nu_\mu + \nu_\tau$ flux versus the ν_e flux for the different mechanisms: CC, NC, and ES (figure taken from [54], original figure by [15]).

sun, including the ^{8}B solar neutrino model, marked in violet. Due to neutrino oscillation, their flavour can change as they propagate through space. Using equation 2.11 and the known distance from the Earth to the Sun, the neutrino oscillation parameters can be derived from the neutrino flux ratios measuring all flavours. The SNO experiment was one of the first experiments to measure the solar neutrino flux [106]. The experimental setup is located approximately 2000 m below the surface of the Earth and thus is well shielded from cosmic rays. The centrepiece of the detector is a spherical acrylic tank with a diameter of 12 m and filled with 1000 t of heavy water (D_2O). It is surrounded by 10 000 photomultipliers, able to detect the Cherenkov radiation[2] emitted when the neutrinos generate an electron inside the tank, which is faster than the speed of light in the medium. Not only the charged currents (CC) from the conversion of neutrons and neutrinos into protons and electrons can be detected, but also neutral currents (NC), over neutrinos disintegrating protons and neutrons, as well as elastic scattering (ES) of neutrinos with electrons [15]. Consequently, the SNO experiment is able to measure electron neutrinos and the total neutrino flux, containing ν_e, ν_μ, and ν_τ. The results prove unequivocally the existence of neutrino oscillation and the measured total neutrino flux is congruent with predictions given by the standard model. The SNO experiment also was able to give values for $\sin^2(\theta_{12})$ and Δm^2_{12}. Combined with the data of the Borexino [108] and the Super-Kamiokande [4] experiment, the results were confirmed and further improved. Figure 2.5b shows the results of SNO and Super-Kamiokande combined.

On the contrary, atmospheric neutrinos are generated in the Earths' upper atmosphere. High energy cosmic rays, in the range of GeV/nucleon, interact with the atoms of the atmosphere. The cosmic rays mainly consist of protons and helium nuclei. As a result of these high energy interactions, a significant number of pions are created, decaying preferably

[2] Cherenkov radiation i a type of electromagnetic radiation emitted when a charged particle passes through a dielectric medium with a velocity, greater than the speed of light inside the medium.

into electrons or positrons, as well as neutrinos:

$$\pi^- \rightarrow \mu^- + \overline{\nu}_\mu \tag{2.12}$$

$$\pi^+ \rightarrow \mu^+ + \nu_\mu. \tag{2.13}$$

The muons are unstable and decay as follows:

$$\mu^- \rightarrow \mathrm{e}^- + \overline{\nu}_\mathrm{e} + \nu_\mu \tag{2.14}$$

$$\mu^+ \rightarrow \mathrm{e}^+ + \nu_\mathrm{e} + \overline{\nu}_\mu. \tag{2.15}$$

One experiment able to measure the neutrino flux originating from the cascades, was the Kamiokande-II experiment [61], followed by the Super-Kamiokande experiment [46]. Similar to the SNO experiment, the centrepiece of the Kamiokande and Super-Kamiokande experiment is an enormous water tank. In the case of Super-Kamiokande the detector is cylindrical, with a height of 41.1 m and a diameter of 39.3 m. Weighing 50 000 t in total, the detector has a fiducial mass of 22 500 t and is surrounded by 11 200 photomultipliers. By measuring the Cherenkov rings, it is possible to detect and distinguish ν_e and ν_μ. The Cherenkov rings also provide information about the direction from where the neutrinos have originated and thus one can conclude where they entered the atmosphere. The baseline can vary from 10 km to 12 700 km depending on the direction and thus, the oscillating parameters can be estimated from the directional deficiencies [67].

Apart from cosmic rays, muon neutrinos can be created with fixed target experiments. There are numerous accelerator neutrino experiments, such as the OPERA experiment with the CNGS beam (CERN Neutrinos to Gran Sasso) [89], as well as MiniBooNE [8] experiment with a neutrino beam from Fermilab. In the case of the long baseline experiment, CNGS 400 GeV protons are aimed at a graphite target, producing pions and kaons which are then focused and subsequently decay into muons and muon neutrinos inside a 1 km long evacuated tube. The generated neutrinos are then detected in the Laboratori Nazionali del Gran Sasso, located approximately 730 km away from the source. In the case of the short baseline experiment MiniBooNE, the flux of muon neutrinos and electron neutrinos are detected in a distance of only 30 m from the source. By comparing the flux ratios, the oscillation parameters can then be determined. Usually accelerator experiments are used to study the transition form ν_μ to ν_τ, giving information about θ_{23} and Δm^2_{23} and the transition ν_μ into ν_e, providing information about θ_{21} and Δm^2_{21}. However ν_μ to ν_e transitions analyses are more complicated, as CP-violation and mixing of ν_1 and ν_3 has to be taken into account.

By now, a number of experiments have measured and confirmed the mixing parameters, summarised in tables 2.1 and 2.2, with the latest results published by the Particle Data Group (PDG) [54]. The CP-violating phase δ_{CP} could not yet be measured with a 3σ confidence. The CP-violating phase would be differing from zero, if neutrino oscillation would violate CP-symmetry.

2.4 Neutrino mass generation

Theories explaining the neutrino mass generation require an extension of the SM and have only been constructed in the past twenty years [85]. The mechanism is based on electroweak symmetry breaking [30] confirmed by the CMS and ATLAS experiment at CERN [12, 28]. Analogue to the mass generation of the charged leptons, right handed neutrinos need to be introduced to the standard model as SU(2) singlets ($(\nu_\mathrm{e})_\mathrm{R}$, $(\nu_\mu)_\mathrm{R}$, $(\nu_\tau)_\mathrm{R}$). Assuming a pure

Table 2.1: Summary of the results for the neutrino mixing parameters. The mass hierarchy and the sign of Δm^2_{32} are not known to date, therefore four different values are given for $\sin^2(\theta_{23})$, each assuming a different hierarchy and sign [54].

Parameter	Value	Comments
$\sin^2(\theta_{12})$	$0.307\,^{+0.013}_{-0.012}$	Results by KamLAND + global solar: Assuming 3ν
$\sin^2(\theta_{23})$	$0.421\,^{+0.033}_{-0.025}$	Results by PDG: Assuming Inverted ordering, $\Delta m^2_{31(32)} > 0$
$\sin^2(\theta_{23})$	$0.592\,^{+0.023}_{-0.030}$	Results by PDG: Assuming Inverted ordering, $\Delta m^2_{31(32)} < 0$
$\sin^2(\theta_{23})$	$0.417\,^{+0.025}_{-0.028}$	Results by PDG: Assuming Normal ordering, $\Delta m^2_{31(32)} > 0$
$\sin^2(\theta_{23})$	$0.597\,^{+0.024}_{-0.030}$	Results by PDG: Assuming Normal ordering, $\Delta m^2_{31(32)} < 0$
$\sin^2(\theta_{13})$	2.21 ± 0.08	Averaged by PDG: Combination of Daya Bay, RENO, and Chooz

Table 2.2: Summary of the results for the mass difference of the neutrino mass eigenstates. As the sign of Δm^2_{32} is not known to date the result is given assuming inverted mass hierarchy (negative) and normal mass hierarchy (positive) [54].

Parameter	Value (in eV^2)	Comments
Δm^2_{21}	$(7.53 \pm 0.18) \times 10^{-5}$	Results by KamLAND + global solar + SBL + accelerator: Assuming 3ν
Δm^2_{32}	$(-2.56 \pm 0.04) \times 10^{-3}$	Results by PDG: Assuming inverted mass hierarchy
Δm^2_{32}	$(2.51 \pm 0.05) \times 10^{-3}$	Results by PDG: Assuming normal mass hierarchy

Dirac nature of the neutrino, the mass term is given by:

$$\mathcal{L}_D = -m_D \left(\bar{\nu}_\mathrm{L}\nu_\mathrm{R} + \bar{\nu}_\mathrm{R}\nu_\mathrm{L}\right), \tag{2.16}$$

with the Dirac mass $m_\mathrm{D} = y_D v$, given by the Yukawa coupling y_D and the Higgs field expectation value $v = 174\,\mathrm{GeV}$. Due to the large mass difference of neutrinos in comparison to charged leptons, the Yukawa coupling term would have to be very small $y_\mathrm{D} \leq 10^{-11}$. Assuming the Majorana nature of neutrinos where the neutrino is equivalent to its CP-conjugation, $(\nu_\mathrm{L} \equiv \bar{\nu}^c_\mathrm{R})$ and $(\nu_\mathrm{R} \equiv \bar{\nu}^c_\mathrm{L})$, the Lagrangian can be written as:

$$\mathcal{L}_M = -\frac{1}{2} M_\mathrm{L} \left(\bar{\nu}_\mathrm{L}\nu^c_\mathrm{R} + \bar{\nu}^c_\mathrm{R}\nu_\mathrm{L}\right) - \frac{1}{2} M_\mathrm{R} \left(\bar{\nu}_\mathrm{R}\nu^c_\mathrm{L} + \bar{\nu}^c_\mathrm{L}\nu_\mathrm{R}\right). \tag{2.17}$$

Combining the Dirac and Majorana Lagrangian, leads to the full neutrino mass term:

$$\mathcal{L}_\nu = \mathcal{L}_\mathrm{D} + \mathcal{L}_\mathrm{M} = \frac{1}{2} \begin{pmatrix} \bar{\nu}_\mathrm{L} & \bar{\nu}^c_\mathrm{R} \end{pmatrix} \begin{pmatrix} M_\mathrm{L} & m_\mathrm{D} \\ m_\mathrm{D}^T & M_\mathrm{R} \end{pmatrix} \begin{pmatrix} \nu^c_\mathrm{L} \\ \nu_\mathrm{R} \end{pmatrix} + \mathrm{h.c.}. \tag{2.18}$$

This mechanism would violate the lepton number conservation. One way to realise this is the (type-I) seesaw mechanism with $M_\mathrm{L} = 0$ and $M_\mathrm{R} \gg m_\mathrm{D}$. It also explains the rather small neutrino mass compared to the corresponding lepton mass, avoiding unnatural small Yukawa coupling [5]. The complete extension of the standard model Lagrangian is then written as:

$$\mathcal{L}_\nu = \frac{1}{2} \begin{pmatrix} \bar{\nu}_\mathrm{L} & \bar{\nu}^c_\mathrm{R} \end{pmatrix} \begin{pmatrix} 0 & m_\mathrm{D} \\ m_\mathrm{D}^T & M_\mathrm{R} \end{pmatrix} \begin{pmatrix} \nu^c_\mathrm{L} \\ \nu_\mathrm{R} \end{pmatrix} + \mathrm{h.c.}. \tag{2.19}$$

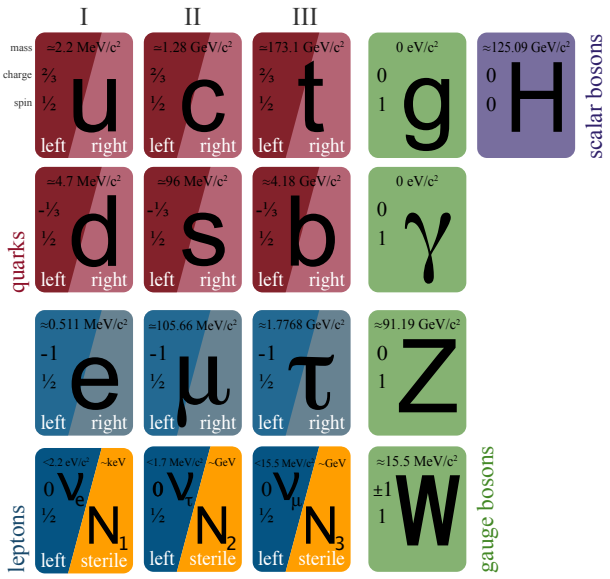

Figure 2.6: νMSM extension of the standard model, including right handed heavy neutrinos. In this case, there is one heavy sterile eigenstates to each light active neutrino (figure adapted from [51, 86]).

The neutrino mass term, including the Majorana mass term has two sets of mass eigenvalues M_i. One corresponds to active light neutrino doublets, whereas the second represents a sterile heavy neutrino gauge singlets and thus predicts a heavy neutrino:

$$\text{active}: \quad |M_1| \sim \frac{m_D^2}{M_\mathrm{R}}, \qquad \text{sterile}: \quad M_2 \sim M_\mathrm{R}. \tag{2.20}$$

Mixing of the light and the heavy sterile neutrino is given by the mixing matrix

$$\theta = m_\mathrm{D} M_\mathrm{R}^{-1} \tag{2.21}$$

A possible prediction for the M_I is the minimal seesaw mechanism. It suggests one right handed neutrino for each light neutrino. If $(m_{\nu_1}, m_{\nu_2}, m_{\nu_3}) \neq 0$, there are a minimum of tree heavy neutrinos. An extension of the minimal standard model by a right handed heavy neutrinos (the νMSM) is depicted in figure 2.6.

2.5 Neutrino mass determination

The proof that neutrinos have non zero mass, was provided by the discovery of neutrino oscillation. However these observations can only provide a mass difference between the mass eigenstates and no absolute mass scale. Thus, numerous experiments are currently trying to determine the neutrino mass. The measurement approaches can be divided into three major categories. First there are direct neutrino measurements, such as the endpoint determination of the single β-decay. Another approach is the half-life measurements of the neutrinoless double β-decay. The third method is indirect determinations from cosmological observations. The following three sections will give an overview of each strategy.

Single β-decay

The most direct method to measure the neutrino mass is by measuring the spectrum of the β-decay. In experiments such as Mainz [76], Troitsk [19], and the current KATRIN

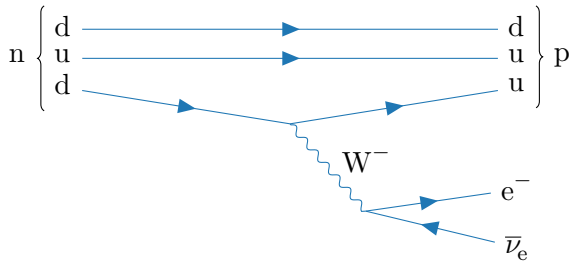

Figure 2.7: Feynman diagram for the β^--decay, where a neutron (dud) decays into a proton (duu), an electron (e^-), and an electron antineutrino ($\overline{\nu}_e$).

experiment the neutrino mass is determined by precise measurements of the tritium decay spectrum. The sources of these experiments is tritium, therefore it is crucial to know the exact shape of the tritium spectrum. Hereby a neutron in the tritium nucleus decays into a proton bound in a helium nucleus, an electron, and an electron antineutrino.

$$T_2 \rightarrow THe^+ + e^- + \overline{\nu}_e \tag{2.22}$$

$$n \rightarrow p + e^- + \overline{\nu}_e. \tag{2.23}$$

The corresponding Feynman diagram for a neutron decay is illustrated in figure 2.7. According to the conservation of momentum and energy, the energy is distributed over the three daughter particles of the decay. Hereby the electron antineutrino is holding an energy of:

$$E_{\overline{\nu}_e} = \sqrt{m_{\overline{\nu}_e}^2 c^4 + p_{\overline{\nu}_e}^2 c^2} \tag{2.24}$$

As neutrinos are holding an non zero mass, the energy of the resulting neutrino is $> 0\,\mathrm{eV}$. This manifests itself in a distortion of the tritium spectrum, in the endpoint region, whereas the endpoint is shifted by the neutrino mass to lower energies. Section 4.3.1 gives a more detailed description of the theoretical β-decay spectrum of tritium.

Figure 2.8 illustrates the influence of the neutrino mass on the differential tritium spectrum for the KATRIN experiment. With larger neutrino masses, the endpoint shifts to lower energies compared to E_0. The plot shows, that the endpoint is shifted by the neutrino mass itself and can therefor be determined directly. Another great advantage of this method is its model independence, compared to estimations via cosmological observations.

Double β-decay

The double β-decay describes the simultaneous β-decay of two nuclei. There are two possible types of double β-decay, the ordinary double β-decay ($2\nu\beta\beta$-decay) and the neutrinoless double β-decay ($0\nu\beta\beta$-decay). As the name suggests, the ordinary $2\nu\beta\beta$-decay is a simultaneous decay of two neutrons, emitting two protons, two electrons, and two electron antineutrinos. Apart from a decay of two neutrons in the nucleus, it is also possible that two protons decay simultaneously in a nucleus. If the simultaneous proton decay absorbs two orbital electrons, the mechanism is known as a double electron capture Starting from the Bethe-Weizsäcker formula, nuclei with the same mass number are a quadratic function of the nuclear charge number. For some isotopologues like ^{76}Ge, the parabolas of odd/odd and even/even nuclear states, split up due to the nuclear pairing force. A first order weak interaction (single β-decay) can be forbidden, as it is a more energetic state. On the other hand a second order weak decay can be allowed when it is energetic preferable, isolating the double β-decay from the single β-decay.0 The spectrum of the double β-decay

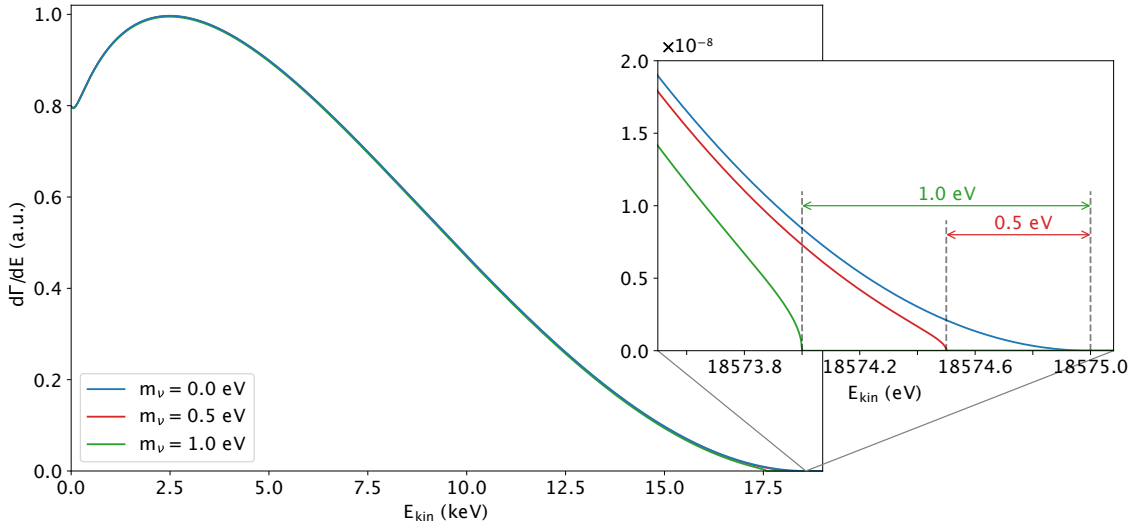

Figure 2.8: Influence of the neutrino mass on the endpoint of the differential tritium spectrum for the KATRIN experiment. Larger neutrino masses shift the endpoint to lower energies. Measuring the endpoint gives direct conclusions about the neutrino mass.

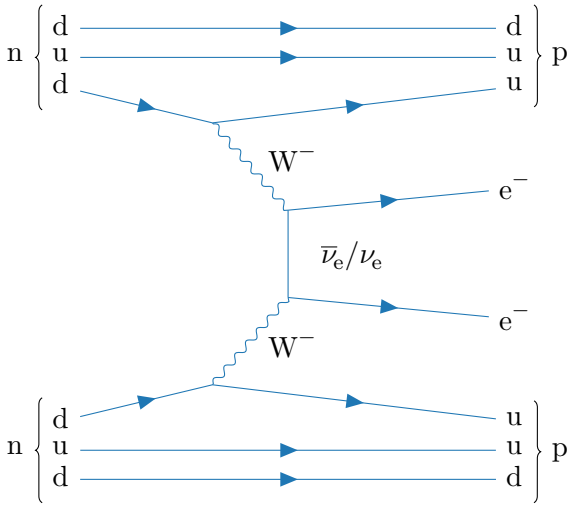

Figure 2.9: Feynman diagram of a neutrinoless double β-decay. Two neutrons (ddu) decay into two protons (duu), by releasing W^--bosons. One of the W^--bosons decays into an electron (e^-) and an electron antineutrino ($\overline{\nu}_e$), which then is absorbed by the other W^--boson, resulting in a second electron (e^-). A premise for this mechanism would be that the neutrino behaves like a Majorana particle $\nu_e = \overline{\nu}_e$.

is a continuous electron spectrum, similar to the single beta decay, with an endpoint shift by double the electron neutrino mass. By now there are 35 nuclei, known to be able to decay via a double β-decay, like ^{76}Ge [59]. So far however, only ($\beta^-\beta^-$)-decays and double electron captures have been observed [91].

The neutrinoless double β-decay or $0\nu\beta\beta$-decay is theoretically possible, if the neutrino is a Majorana fermion. This means that the neutrino is its own antiparticle. Figure 2.9 shows the Feynman diagram of a $0\nu\beta\beta$-decay process. As illustrated, the neutrino emitted by one of the β-decays, is absorbed by the second β-decay. By absorbing the neutrino in the secondary decay, the energy is conserved, which would result in a characteristic mono energetic peak at the endpoint of the spectrum.

According to the standard model the conservation of the lepton number is violated in this mechanism and therefore would be prohibited. This could only be explained by physics beyond the standard model. The $0\nu\beta\beta$-decay rate is proportional to the Majorana mass $m_{\beta\beta}$, and thus follows:

$$m_{\beta\beta} = \left| \sum_{i=1}^{3} U_{ei}^2 m_i \right|. \tag{2.25}$$

By measuring the decay spectrum of ^{76}Ge, the MAJORANA experiment and the GERDA experiment, are both trying to measure the $0\nu\beta\beta$-decay. Current upper limits on the effective Majorana mass by GERDA are $m_{\beta\beta} \leq (0.12 - 0.26)\,\text{eV}$ [7]. The MAJORANA project, released an upper limit on the effective Majorana mass in the range of $m_{\beta\beta} \leq (0.24 - 0.52)\,\text{eV}$ [1].

Cosmology

To describe the evolution of the universe from the Big Bang to today, most successful is the ΛCDM-model also known as the standard model of cosmology. The ΛCDM-model is derived from cosmological observations and can recreate the formation of the universe with six free parameters: the Hubble constant H_0, the baryon density parameter Ω_b, the matter density parameter Ω_m, the optical depth to the reionization τ, the curvature fluctuation amplitude A_s, and scalar spectral index n_s. It is in good agreement with three main cosmological observations: the anisotropy of the cosmic microwave background, the accelerated expansion of the universe, and large-scale structures in the distribution of galaxies. Today the content of the universe is comprised of 68.5 % dark energy (Ω_Λ), 26.6 % dark matter (Ω_m-Ω_b), and only 4.9 % matter (Ω_b) [93].

Baryonics and charged leptons make up the observable matter. Further, there are photons, which can be observed in the cosmic microwave background (CMB), remnants of the period of recombination – 380 000 years after the Big Bang [20]. The model is in good agreement with the measured CMB and the visible polarisation. Included in the model are also neutrinos, decoupling from primordial plasma when the Hubble parameter became bigger than the annihilation rate, approximately 1 s after the Big Bang. The current cosmic neutrino background (CνB) density is $336\,\text{cm}^{-3}$ with an estimated black body temperature of 1.945 K [116].

Since neutrinos of the CνB have low energy and small cross sections, no direct detection of the CνB could be observed to date. Studies on the other hand show, that the neutrino mass is significantly connected to the structure of the universe. Figure 2.10 illustrates how small scale structures are washed out with a greater neutrino mass, whereas large structures are less effected. By comparing simulations with cosmological observations, an upper limit on the total neutrino mass can be established. The latest Planck results give

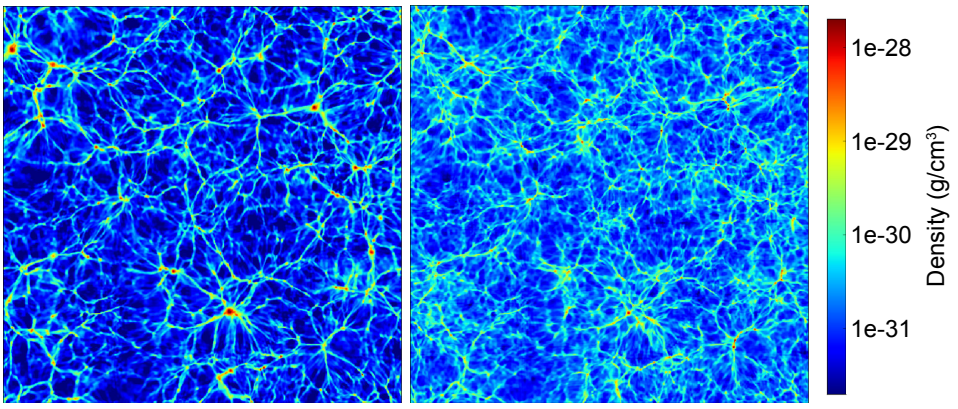

(a) $\sum m_\nu = 0\,\mathrm{eV}$. **(b)** $\sum m_\nu = 1.9\,\mathrm{eV}$.

Figure 2.10: Simulated distribution of the baryonic matter in a $200\,\mathrm{h}^{-1}$Mpc slice, with a cell size of $\sim 391\,\mathrm{h}^{-1}$kpc. **(a)** Simulations were performed with $\sum m_\nu = 0\,\mathrm{eV}$ neutrinos. **(b)** As well as simulations assuming neutrinos with $\sum m_\nu = 1.9\,\mathrm{eV}$. Raising the total neutrino mass, smears out small structures and makes large structures less distinguishable (figure adapted from [6]).

an upper limit in the range of $\sum_\nu m_\nu < (0.340 - 0.715)$ eV, 95 % CL [90]. It should be noted that all limits on the neutrino mass given by cosmological observations are strongly model dependent. Again, this underlines the importance of the neutrino and that the mass has to be measured by model-independent experiments.

Dark matter is introduced to the ΛCDM-model to explain the structural formation and the gravitational effects on small-scales, such as rotation of galaxies or gravitational lensing effects. The model assumes cold dark matter (CDM), a non-barionic matter with a low velocity, which is not dissipating energy via photons [5].

Dark energy is postulated as a non vanishing vacuum energy, explaining the accelerating expansion of space. In the ΛCDM-model, dark energy is represented by the cosmological constant Λ.

2.6 Neutrino dark matter

Dark matter plays an important role in the structural formation of the universe. A possible candidate for dark matter are sterile neutrinos [22]. The objective of this thesis is to analyse KATRIN data in regard to a keV-scale sterile neutrino, thus the effects of dark matter and the imprint of sterile neutrinos will be discussed more in detail in the subsequent sections.

As described in the previous section, the ΛCDM-model incorporates cold dark matter. Satellite missions such as the Wilkinson Microwave Anisotropy Probe (WMAP) [21] and the Planck-mission were able to determine a value for the amount of dark matter in the universe. Latest results by the Planck collaboration estimate that the universe has a dark matter content of 26.6 % and thus makes up 84 % of the total mass [93]. The hypothesis of dark matter emerged in the 1933 by theories from F. Zwicky [117]. Zwicky observed the rotation of Coma clusters and determined that according to the rotational velocity of the outer parts of the Coma cluster, the mass was estimated to be 400 times higher than the visually observable mass. Therefore, non baryonic mass had to be contributing to ∼90 % of the Coma clusters mass. Dark matter can be divided into tree different groups, cold dark matter (CDM), hot dark matter (HDM), and warm dark matter (WDM). Each group has a different power spectrum and therefore a different free streaming length $\lambda_f s$. The

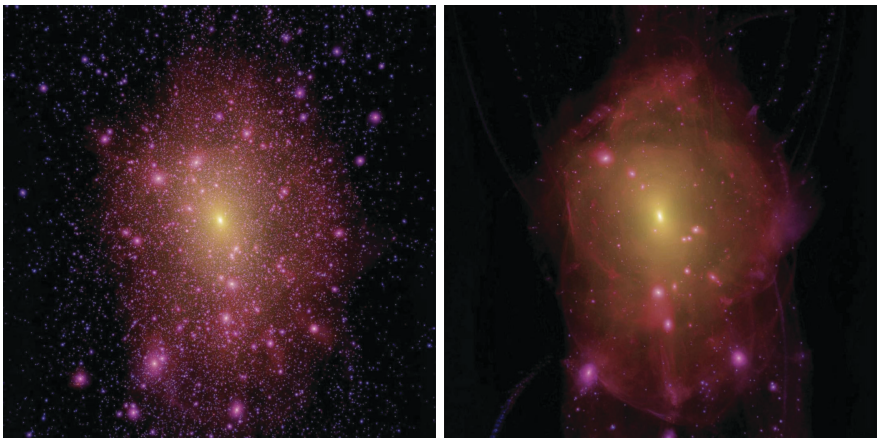

(a) CDM. **(b)** WDM.

Figure 2.11: Halo simulations assuming the CDM as well as WDM. Each window shows a 1.5 Mpc sector. **(a)** Assuming the CDM power spectrum. **(b)** Assuming a WDM power spectrum. Caustics are sharper and more pronounced in the case of WDM [79].

free streaming length is determined by the mass and the speed after the decoupling and the particles nature, thus describes how far the particles can travel without interacting. A large streaming results in the suppression of small scale density fluctuations, as particles can travel long distances through matter without interacting.

Cold dark matter is the candidate favoured most in the ΛCDM-model. CDM is in the mass range of ∼GeV. As mentioned in the previous section dark matter has a large influence on the structural formation of the universe. In the case of CDM, small structures gradually accumulate first, whereas larger structures such as galaxies and galaxy clusters are formed later. A promising candidate for CDM are weakly interacting massive particles (WIMP) [55]. WIMPs are theorised in the minimal supersymmetric standard model (MSSM).

Hot dark matter on the other hand would have a mass in the order of eV and a free streaming length of ∼Mpc. In contrary to CDM, HDM would influence the formation in such a way, that large structures are created first, and later smaller structures are formed. However galaxy clusters have been observed which are older than the galaxy they are a part of, thus contradicting the scenario of HDM.

Another possibility would be the contribution of warm dark matter. WDM, in the range of ∼keV, is in between CDM and HDM and thus agrees with large and small scale formations. Comparing the power spectra of CDM and WDM, the WDM power spectrum has a cut off, whereas the CDM power spectrum is continuous for higher energies [79]. Simulations show, that WDM, like CDM, would comply the requirements by the CMB, since for large scales WDM and CDM are almost indistinguishable. However the effects on structural formation are distinguishable on the scales of dwarf galaxies (≤∼Mpc). Figure 2.11 compares halo simulations on the scale of 1.5 Mpc assuming a CDM power spectrum (figure 2.11a) and a WDM power spectrum (figure 2.11b). For simulations with the assumption of WDM, caustics are shown higher in contrast. WDM would also be able to solve tensions on small cosmological scales and resolve the missing satellite problem[3] [38,79] . A possible candidate for WDM could be a keV-scale sterile neutrino, as for example given by the νMSM.

[3] In the missing satellite problem, the observed occurrence of dwarf galaxies is lower by one order of magnitude than suggested by simulations with CDM.

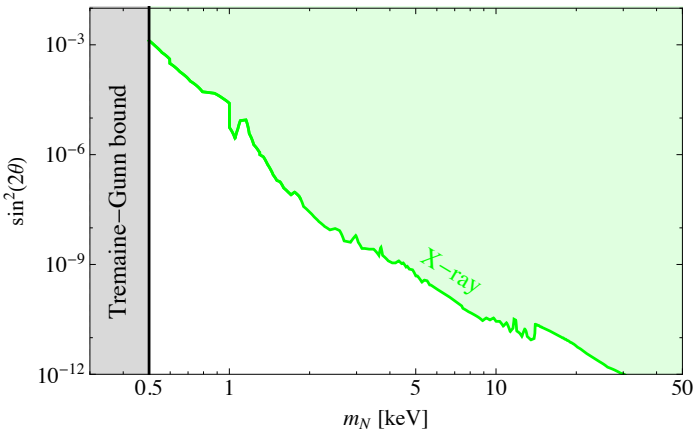

Figure 2.12: Current constrains on a keV-scale sterile neutrino given by the Termain-Gunn bound and the X-ray bound. Coloured ares can be excluded (figure adapted from [38]).

2.7 keV-scale sterile neutrinos and their imprint on the β-spectrum

As described in section 2.4, the rather small mass of the neutrino can be explained by introducing a right handed, sterile neutrino, that can mix with the light, active SM neutrinos. One possible sterile neutrino could be in the keV-mass scale. Assuming, for example, an active light and a heavy sterile neutrino, mixing of the neutrino eigenstates could be expressed as:

$$\text{light}: \quad \sum_{i,\,\text{light}} \left|U_{ei}^2\right| =: \cos^2(\theta). \tag{2.26}$$

$$\text{heavy}: \quad \sum_{i,\,\text{heavy}} \left|U_{ei}^2\right| = 1 - \sum_{i,\,\text{light}} \left|U_{ei}^2\right| = \sin^2(\theta). \tag{2.27}$$

In the case of three light mass eigenstates, equation 4.5 is summed over the three eigenstates [39]. Accordingly, equation 4.6 represents the mixing amplitude of the sterile neutrino in the generic case of one heavy, sterile neutrino. This would be necessary in the νMSM, including three different sterile neutrinos. In comparison to the differential spectrum, discussed in 2.5, the differential decay spectrum would change as follows:

$$\frac{\mathrm{d}\Gamma}{\mathrm{d}E} = \cos^2(\theta) \cdot \frac{\mathrm{d}\Gamma}{\mathrm{d}E}\left(m_{\text{light}}\right) + \sin^2(\theta) \cdot \frac{\mathrm{d}\Gamma}{\mathrm{d}E}\left(m_{\text{heavy}}\right). \tag{2.28}$$

Figure 2.13 and 2.14 shows the influence of a sterile neutrino on the differential tritium spectrum. The spectrum includes a $m_{\text{heavy}} = 9.0\,\text{keV}$ sterile neutrino, with a mixing angle of $\theta = 20°$. In the differential spectrum a sterile neutrino would manifest as a kink. The position of the kink is given by the mass of the sterile neutrino and the amplitude is given by the mixing amplitude $\sin^2(\theta)$. keV-scale neutrinos could function as WDM, with a free streaming length in the order of $\sim$ kpc. The simplest production mechanism for these sterile neutrinos would be via mixing with an active light neutrino in the primordial plasma [31]. Figure 2.12 show current constrains on a keV-scale sterile neutrino, given by the Tremaine-Gunn bound and by non observations of X-rays induced by the decay of satellite neutrinos [38]. The Tremaine-Gunn bound is obtained from phase space analysis, limiting the phase space density via the Pauli principle. Depending on the production mechanism of sterile neutrinos, the currently lowest bound is 0.4 keV [109].

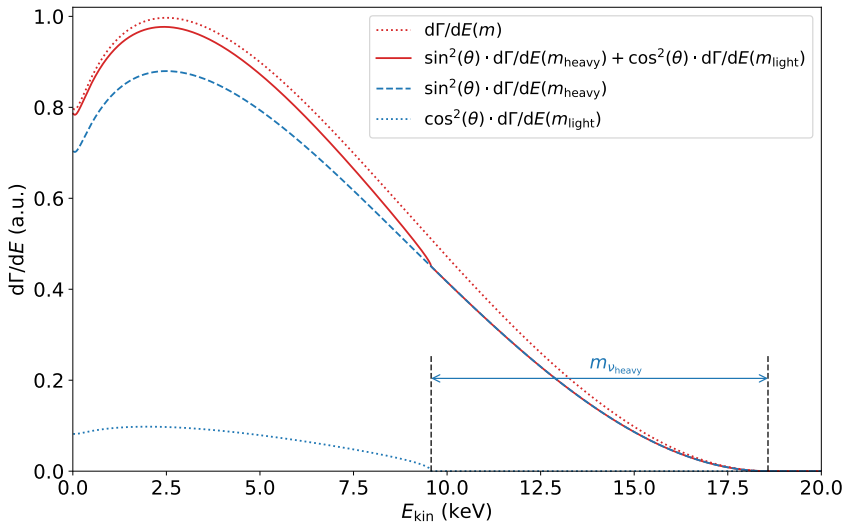

Figure 2.13: Imprint of a heavy sterile neutrino on the shape of the tritium decay spectrum. The plot includes a $m_{\text{heavy}} = 9.0\,\text{keV}$ sterile neutrino with a mixing angle of $\theta = 20°$. The involvement of a sterile neutrino can be observed by a kink in the spectrum. Shape of the tritium decay spectrum without a sterile neutrino (dashed red) and with a sterile neutrinos (solid red). The component of the tritium spectrum caused by the light neutrino (dashed blue) and the heavy sterile neutrino (dotted blue) is also shown.

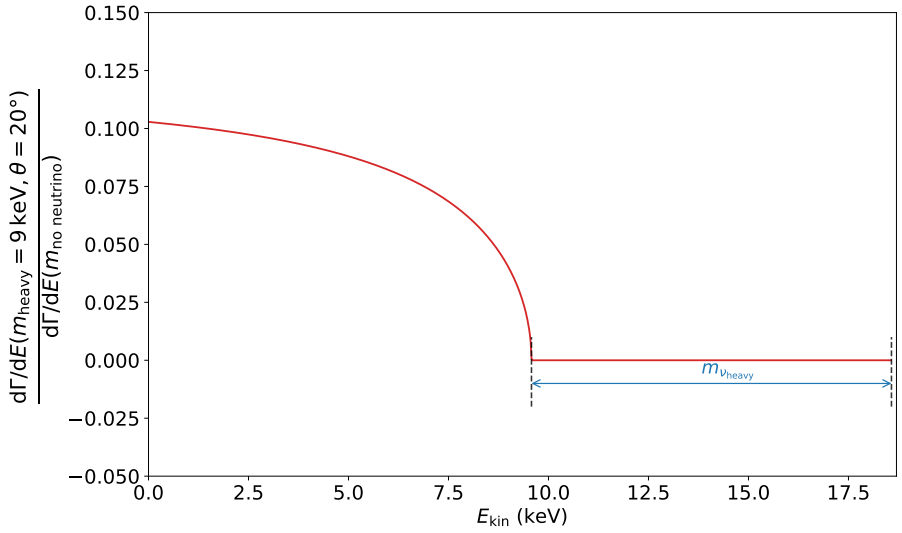

Figure 2.14: Ratio of the decay spectrum with a sterile neutrino and a spectrum without a sterile neutrino. The ratio has been shifted to zero in the region above the kink. Analogue to the previous figure, the plot includes a $m_{\text{heavy}} = 9.0\,\text{keV}$ sterile neutrino with a mixing angle of $\theta = 20°$ (figures similar to [33]).

3. The KATRIN experiment

The KATRIN experiment is one of the most ambitious experiments for direct neutrino mass measurements. With an exceptionally high source strength and a high sensitivity close to the endpoint it is possible to determine the neutrino mass with a sensitivity of $m_\nu = 200\,\mathrm{meV}$ (90 % CL) via spectral measurements of the tritium decay kinematics. In this chapter the fundamental concepts of the measurement technique are discussed, followed by a description of the experimental setup. The unprecedented statistical sensitivity on the neutrino mass will be also discussed, as well as the future KATRIN sterile neutrino search with the TRISTAN project.

3.1 Working principle of a MAC-E filter

Magnetic adiabatic collimation combined with an electrostatic filter (MAC-E filter) is a special combination of magnetic and electric fields to guide charged particles and filter them according to their kinetic energy. A schematic illustration of the electron motion is depicted in figure 3.1. In general electrons in a magnetic field travel with cyclotron motion along their flight direction. The kinetic energy of electron E_{kin} thus can be described as an energy component transversal E_{t} and longitudinal E_{l} to the magnetic field lines [64]. The pitch angle θ of the electrons is given by:

$$\sin(\theta) = \frac{E_{\mathrm{t}}}{E_{\mathrm{l}}}. \tag{3.1}$$

The electric field inside a MAC-E filter is generated by electrodes with a gradient from each end with $U = 0\,\mathrm{kV}$ to the centre $-U_{\mathrm{max}}$. Both the electric and magnetic field lines are therefore in parallel. Only electrons with a longitudinal energy component greater than the retarding energy, are able to overcome the electric field. Electrons with a lower energy are back reflected. In figure 3.1 track 1 corresponds to the track of an electron with an energy higher than the retarding energy and therefore is transmitted, whereas track 2 represents an electron with an energy lower than the retarding energy and thus is decelerated and reflected. To analyse the total kinetic energy, the transversal energy component has to be transformed into the longitudinal direction. Transformation of the transversal component can be achieved via the magnetic field. For an adiabatic process, the transversal component in relation to the magnetic field is constant:

$$\frac{E_{\mathrm{t}}}{B} = \text{constant}. \tag{3.2}$$

Collimation can be obtained by guidance along an adiabatic decreasing magnetic field. The magnetic field is generated by magnets at the inlet and outlet of the filter vessel. Due to

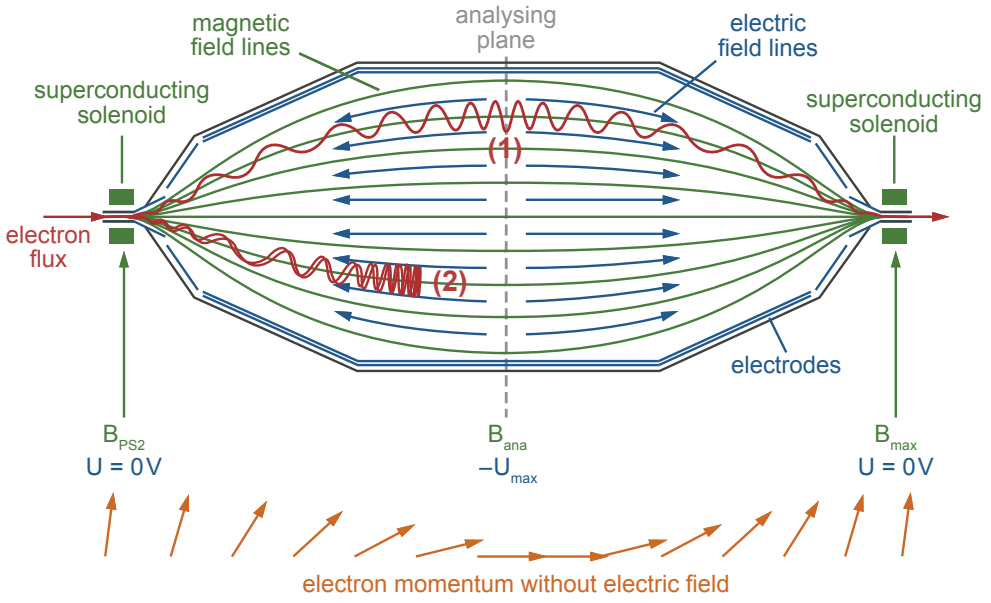

Figure 3.1: Illustration of the working principle of a MAC-E filter. Magnetic fields are created by superconducting solenoids at both ends of the vessel (green). Electric fields are created by electrodes (blue) and are oriented in parallel to the magnetic field lines. Electrons entering the vessel are guided with cyclotron motion along the magnetic field lines. If their energy is higher than the retarding energy they are transmitted (1) otherwise they are reflected (2).

conservation of magnetic flux Φ,

$$\Phi = \int_A \vec{B} \cdot \mathrm{d}\vec{A} = \text{constant}, \tag{3.3}$$

the flux tube widens between the magnets, while reducing the magnetic field strength. To maintain magnetic guidance, the magnetic field in the analysing plane has to be ≥ 0. For this reason, a small fraction of the transversal energy remains, which can not be transformed. The minimum of the magnetic field in the analysing plane is limited by the dimension of the filter vessel. This also gives the maximum energy resolution:

$$\frac{\Delta E}{E} = \frac{B_{\mathrm{ana}}}{B_{\mathrm{max}}} = \frac{r_{\mathrm{ana}}}{r_{\mathrm{max}}}, \tag{3.4}$$

where r is the radius of the flux tube cross section. When the magnetic field is again increased towards the end of the vessel, part of the longitudinal energy is transformed back into the transversal energy component, thus increasing the pitch angle. For large magnetic fields, the $\theta \to 90°$, resulting in a back reflection of the electrons. The maximum acceptance angle is given by:

$$\theta_{\mathrm{max}} = \arcsin\left(\sqrt{\frac{B_{\mathrm{source}}}{B_{\mathrm{max}}}}\right), \tag{3.5}$$

where B_{source} is the magnetic field inside the source . In the KATRIN experiment, the maximum acceptance angle is $\theta_{\mathrm{max}} = 50.77°$.

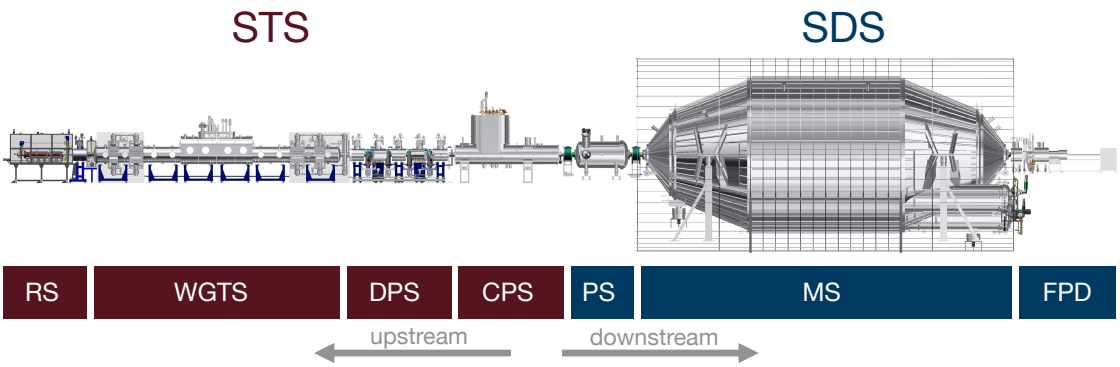

Figure 3.2: Side view of the 70 m long KATRIN experiment. STS consists of the rear section (RS), the windowless gaseous tritium source (WGTS), and the pumping sections, the differential pumping section (DPS) and the cryogenic pumping section (CPS). SDS consists of the pre-spectrometer (PS), the main spectrometer (MS) filter, the monitor spectrometer in parallel, and the focal-plane detector system (FPD) at the downstream end of the experimental setup.

3.2 Setup of the KATRIN experiment

The 70 m long KATRIN experiment can be divided into two sections. The source and transport section (STS) and the spectrometer and detector section (SDS). The STS consists of three main components: The rear section (RS), the windowless gaseous tritium source (WGTS) and the pumping section, which itself can be divided into the differential pumping section (DPS) and the cryogenic pumping section (CPS). The SDS consists of the pre-spectrometer (PS), the main spectrometer vessel (MS), functioning as a MAC-E filter, a detector system at the end of the beamline and a monitor spectrometer connected in parallel. In addition the MS is surrounded by an air-coil system. The MS is followed by the detector system which contains the focal-plane detector (FPD) in its centre. In parallel to the MS, connected via a voltage divider, the monitor spectrometer monitors the high voltage stability. An overview of the setup with the position of each component can be seen in figure 3.2. In the following section the different parts will be described more in detail.

3.2.1 Source and Transport Section (STS)

The main requirement of the β-electron source in the KATRIN experiment is it's high activity and precise stability. High activity is required, to have a sufficient number of β-decays with an energy close to the endpoint which reduces the statistical uncertainty. To realise a high decay rate with small fluctuations, as well as retaining a high vacuum in the spectrometer vessel, a complex source system has been developed.

The tritium gas is injected into the centre of the WGTS, at the beginning of the source transport section. To monitor the stability, several monitoring systems are installed inside the rear section, as well as inside the WGTS and beamtube. To realise a windowless source, necessary to avoid scattering and energy losses of the electrons, and achieving an ultra high vacuum at the end of the STS, a two step pumping system, consisting of a differential pumping section (DPS) and a cryogenic pumping section (CPS) are required. The following sections will describe the main STS components and their functions.

Windowless gaseous tritium source (WGTS)

The WGTS is a 10 m long tritium source, open to both ends, providing the experiments β-electron flux. A graphical representation of the WGTS can be seen in figure 3.3. In the

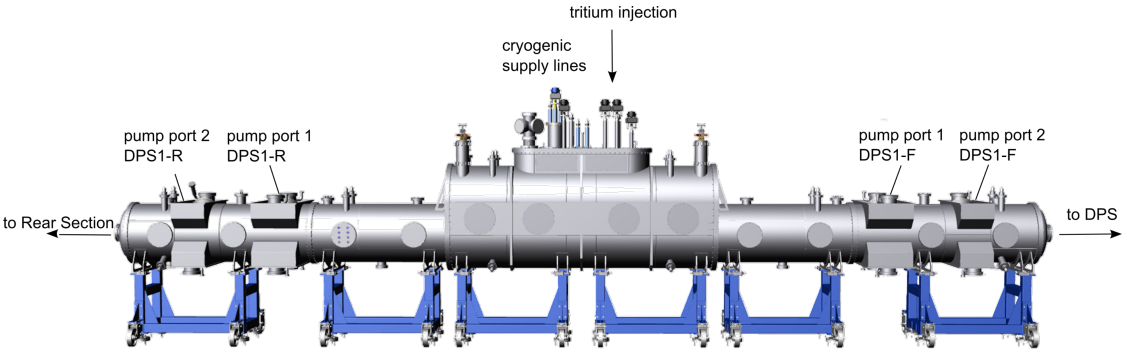

Figure 3.3: CAD model of the WGTS. In the source tritium decays isotropically, supplying the experiment with a sufficient β-electron rate. The tritium is injected into the centre of the WGTS, flowing to each end where it is pumped out by turbo molecular pumps (DPS1) [78].

WGTS mainly tritium molecules are constantly, isotropically decaying, such as:

$$T_2 \rightarrow THe^+ + e^- + \overline{\nu}_e \tag{3.6}$$

The generated electrons are then guided magnetically through the source, downstream into the transport section.

To supply the source with a stable tritium rate and pressure, it is connected to a gas cycle called the inner LOOPS system [96], constantly injecting tritium through capillaries into the centre of the WGTS. At each end of the WGTS two turbo molecular pumps are located, DPS1-R and DPS1-F, each via two pump ports, in order to reduce the pressure by a first step. The LOOPS-cycle purifies the partially decayed gas and reinjects the gas into the centre, ensuring a constant tritium concentration and pressure. The system is able to provide a stable pressure and thus a stable decay rate on the 0.1 % level. Both, the gas concentration and the activity are constantly monitored. The concentration is monitored by the LARA system (Laser Raman spectroscopy system) [44], whereas the activity is monitored by the FBM (forward beam monitor) and the BIXS (beta induced X-ray spectrum) system, these systems are described in detail in the following two sections.

To minimise thermal Doppler broadening, the gas is cooled to a stable temperature of (30.0 ± 0.3) K [53]. This is achieved with a two stage neon cooling.

In the nominal setting, the WGTS is operated with a column density of $5 \times 10^{17}\,\mathrm{cm}^{-2}$, referring to the number of tritium molecules per square centimetre, with an injection pressure of 3.35×10^{-3} mbar. With these technical framework conditions, the WGTS provides a constant decay rate of $\sim 10^{11}\,\mathrm{s}^{-1}$ [78, 83].

Rear section (RS)

The rear section is at the upstream end of the KATRIN experiment. There are three main components built in to monitor and calibrate the experiment. Only a fraction of all created electrons make it through the entire experimental beamline. All remaining electrons are reflected and sent back into the rear section. By interactions with nuclei in the rear wall, the electrons emit X-rays. From these X-rays one can deduce the count rate and therefore use the X-ray spectrum to monitor the source activity. Monitoring is realised with the BIXS system (Beta induced X-ray spectrometry) [100, 101]. Furthermore the rear section is used to give the reference potential for the back of the experiment as well as to define

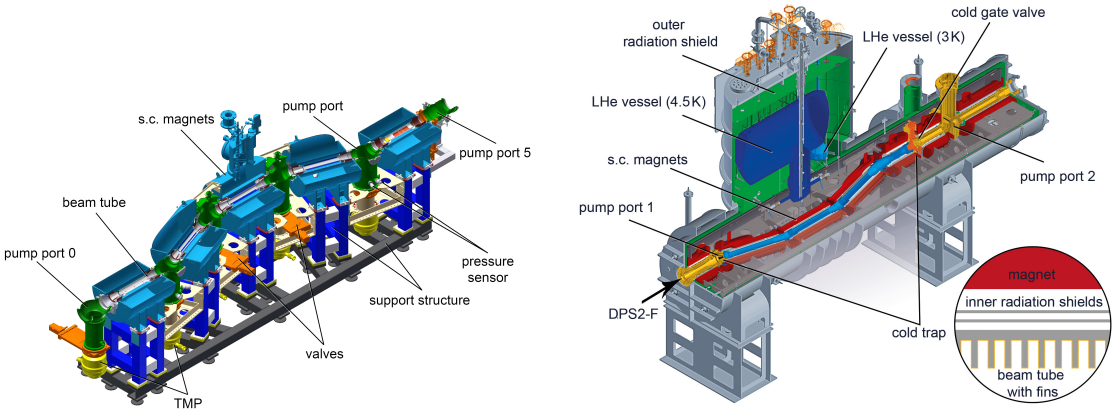

(a) DPS2-F. **(b)** CPS.

Figure 3.4: (a) CAD model of the differential pumping section DPS2-F following the WGTS in downstream direction. **(b)** CAD model of the cryogenic pumping section CPS. Combining both systems, it is possible to reduce the pressure by a factor of (figures adapted from 10^{14}. The main components will be described in the text [45]).

the electric potential of the tritium plasma inside the WGTS [13, 14]. Another important component of the rear section is an angular-selective photoelectric calibration source [112]. As electrons interact via inelastic scattering, while passing through the source, an e-gun can be utilised to measure the column density and determine the transmission function [13].

Forward beam monitor (FBM)

The FBM is the only monitor system inside the beamtube of the CPS, capable of constantly determining and monitoring the β-electron flux with a 0.1 % level of precision. The monitor system consists of two PIN diodes, installed on a rotating detector board. The whole board can be inserted, as well as scanned through the cross section of the flux tube. Due to its movability, the FBM can measure the decay profile inside the flux tube as well as constantly monitor at the side of the flux tube. The energy spectrum can also be taken in a differential mode with an energy resolution of $E_{\mathrm{FWHM}} = 2.0\,\mathrm{keV}$ [40].

Transport section

The transport section can be divided into two sections. The WGTS is followed by a differential pumping section (DPS2-F) which leads to the cryogenic pumping section (CPS). A main requirement to the transport section is that an ultra high vacuum can be achieved at the end, with a pressure lower than 10^{-11} mbar and a maximum partial tritium pressure of 10^{-20} mbar. Reducing the pressure by a factor of 10^{14} in comparison to the WGTS [82]. A graphical representation of both the DPS2-F and the CPS are shown in figure 3.4.

The beam tube inside the DPS2-F is split into five sections, where the central three sections are each tilted by 20° to each other, in a chicanery manner. Each segment is located inside a superconducting solenoid.To accomplish adiabatic guidance of the electrons, the magnets are operated at 5.6 T [58]. The 7 m long DPS2-F is equipped with five turbomolecular pumps, reducing the tritium flow by the order of $\sim 10^4 - 10^5$ [66]. Each turbomolecular pump is connected via pump ports between the beam tube sections, as well as one before and one after the DPS2-F (pump ports 0 and 5). As each of the central three DPS segments is equipped with a dipole electrode. Inside the electric field charged particles are forced onto curved tracks via the Lorentz force. Positive ions are deflected in the opposite direction

to electrons, thus positive ions deflected onto the walls [56]. To prevent residual positive ions from entering the spectrometer, a ring electrode is installed at the downstream end of DPS2-F. By biasing the WGTS and the DPS-ring-electrodes with a positive potential, positive ions can be deflected, preventing them from reaching the spectrometers. To identify the ion type, an FT-ICR (Fourier Transformation-Ion Cyclotron Resonator) is installed at the end of DPS2-F inside beam tube 5 [110].

Connected to the DPS-F is the CPS, with the purpose to reduce the pressure by another seven orders of magnitude via cryogenic absorption of tritium molecules. Figure 3.4b gives an overview of the CPS structure. The 6.5 m long section, can be subdivided into seven beam tube segments, each surrounded by a superconducting magnet, guiding the electrons adiabatically, with a magnetic field of 5.6 T. The second to fifth segment are prepared with an argon frost layer on the inside. To maximise the surface area of the argon frost layer, the inner tube surface is equipped with 90 gold plated fin structures, giving a total surface of 2 m^2. To sustain the argon frost layer, the tubes are cooled by liquid helium to 3 K. It is possible to absorb tritium molecules within the frost layer. To make the tritium trapping more efficient and to avoid a continuous tritium beam in the centre, the second and forth tube section are each tilted by 15°. The CPS is also connected to turbomolecular pups over pump ports 1 and 2, to evacuate the beam tube in the case of removal of the argon layer during the maintenance phases, as well as evacuation during bake-out [45, 48].

3.2.2 Spectrometer and detector section (SDS)

The SDS is composed of two spectrometer vessels and a detector system at the downstream end of the experimental setup, with the purpose to regulate the transmission of electrons from the source, depending on their kinetic energy and to detect these electrons. Both spectrometer vessels function as MAC-E filters. The functional principle of MAC-E filters is depicted in section 3.1. To minimise energy loss due to scattering with gas molecules inside the spectrometer and to reduce background induced by decay of residual gas, the spectrometer detector section is operated at an ultra high vacuum of $\sim 10^{-11}$ mbar. Part of the SDS is also the monitor spectrometer, located in a building next to the beamline, monitoring the high voltage stability continuously. In the subsequent sections the four major components will be explained in detail.

Pre-spectrometer (PS)

Connecting to the CPS, the pre-spectrometer is the first component in the spectrometer and detector section. With a length of 3.4 m and a diameter of 1.7 m it functions as a MAC-E filter system to pre-filter low energy electrons consequently reducing the electron flux into the main spectrometer. By setting the vessel to a potential close to the region of interest, the electron flux can be reduced by 10^7 before the main spectrometer. At the inlet and outlet of the pre-spectrometer vessel superconducting solenoids are installed (PS1-magnet and PS2-magnet). By setting both magnets to 4.5 T the pre-spectrometer can reach an energy resolution around 70 eV for electrons with an energy close to the endpoint [58]. To investigate and characterise background effects and magnet guidance in electric fields, the pre-spectrometer was used as a test setup for the main spectrometer vessel beforehand [52, 82, 113].

However, if both, the pre-spectrometer and the main spectrometer, are set on high voltage, in combination with the presence of magnetic guidance, the fields can lead to the creation of a Penning trap. In this case charged particles can be axially confined on cyclotron trajectories and thus trapped between the pre- and the main spectrometers [95]. The

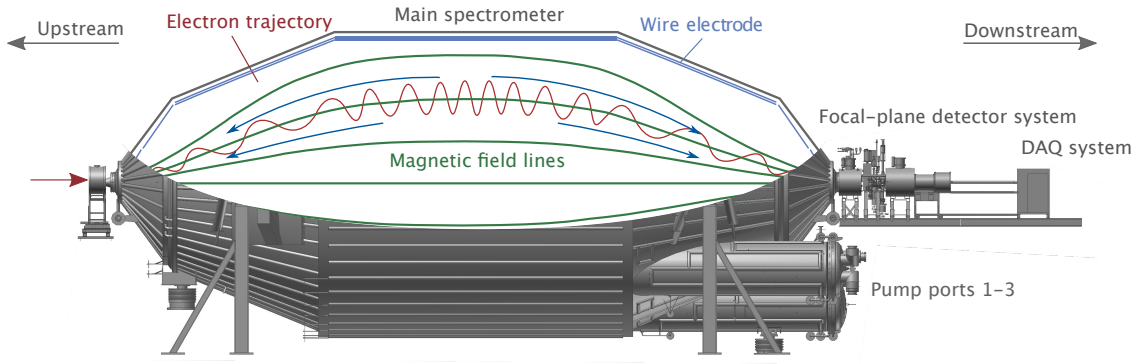

Figure 3.5: Schematic illustration of the main spectrometer vessel. Electrons entering the vessel are guided on helical tracks along the magnetic field lines. If the kinetic energy is higher than qU_{ret}, electrons can overcome the electric potential and reach the focal-plane detector (figure adapted from [58]).

trapped particles contribute to the background and the effect can lead to a spontaneous Penning discharge. The effect was investigated, showing that both spectrometers can be used in combination for low retarding energies [95].

Main spectrometer (MS)

To obtain a high energy resolution the KATRIN collaboration designed and constructed a large MAC-E filter system. With a length of 23.3 m, a diameter of 10 m, and a volume of 1240 m^3 the main spectrometer is the largest spectrometer vessel ever built [58]. A schematic illustration of the main spectrometer vessel is given in figure 3.5. Maintaining an ultra high vacuum inside the main spectrometer is realised by the utilisation of large turbomolecular pumps and non-evaporating getter pumps, located at the downstream end of the vessel (pump ports 1 – 3).

A superconducting magnet is located between the pre- and the main spectrometer (PS2), operated at 4.5 T. Furthermore a superconducting solenoid is installed between the main spectrometer vessel and the detector. This pinch magnet is operated at $B_{\mathrm{pinch}} = 6\,\mathrm{T}$. Due to conservation of magnetic flux both magnets generate a large flux tube in the centre of the spectrometer, with a magnetic field around $B_{\mathrm{ana}} = 1.79 \times 10^{-4}\,\mathrm{T}$ in the analysing plane. Because of the large size, and the low gradient magnetic field, it is possible to guide electrons adiabatically for small surplus energies. The maximum magnetic field strength is located inside the pinch magnet, whereby $B_{\mathrm{max}} = B_{\mathrm{pinch}}$.

The main background sources can be traced back to electron emission of the wall, induced by the cosmic muon flux interacting inside the vessel walls, and the decay of radioactive isotopes present inside the stainless steel walls. Inside the steel vessel a system of wire electrodes are installed in parallel to the walls. By setting the electrodes on negative potential, it is possible to prevent electrons, emitted by the steel walls, to enter the sensitive volume thus reducing the background coming from the walls [111].

Additionally, the main spectrometer is surrounded by an air-coil system consisting of 15 air coils providing the low field correction system (LFCS). By adjusting the current running through each coil, the flux tube can be shaped more precisely. It is also necessary to increase the magnetic field in the analysing plane by setting the LFCS currents accordingly, so the flux tube does not collide with the spectrometer walls. In this way it is possible to reach a magnetic field of $B_{\mathrm{ana}} = 3 \times 10^{-4}\,\mathrm{T}$ in the analysing plane [64].

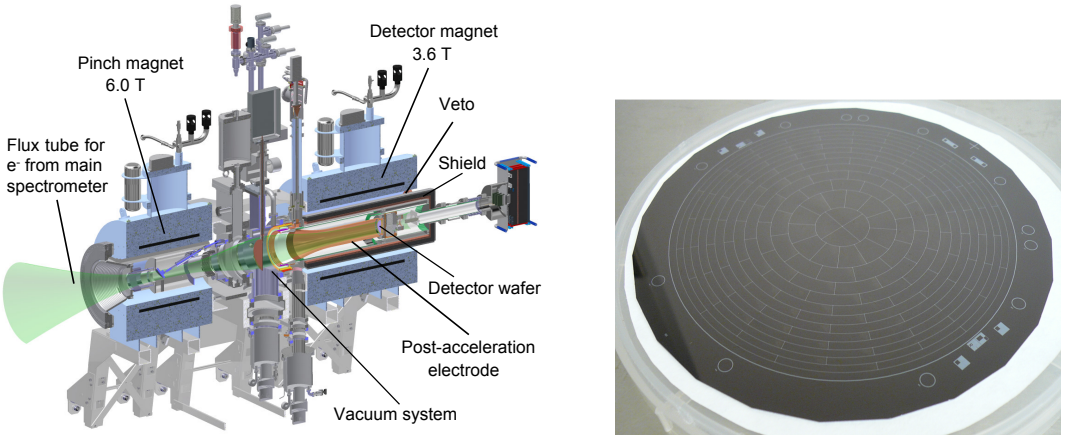

(a) The KATRIN focal-plane detector system [10].

(b) The detector wafer [32].

Figure 3.6: (a) CAD of the focal plane detector system (adapted from [10]). The electron flux tube is narrowed by the pinch magnet, guiding electrons from the main spectrometer to the focal-plane detector, in the centre of the detector magnet. **(b)** Top view of the silicon FPD-wafer installed inside the detector magnet (picture taken from [32]).

The relative energy resolution of the spectrometer at the endpoint is given by [71]

$$\frac{\Delta E}{E_0} = \frac{B_{\text{ana}}}{B_{\text{max}}} \quad \Rightarrow \quad \Delta E = \frac{3 \times 10^{-4}\,\text{T}}{6\,\text{T}} \cdot 18\,575\,\text{eV} = 0.928\,\text{meV} \tag{3.7}$$

Another 16 air coils are installed vertically and 10 air coils horizontally Earth magnetic field compensation system (EMCS) to the main spectrometer. The purpose of these additional coils is to counteract and compensate the terrestrial magnetic field [50].

Detector system

To measure the integral tritium spectrum, a detector system is located at the downstream end of the setup. The magnetic flux tube is narrowed by the pinch magnet set to $B_{\text{pinch}} = 6\,\text{T}$, followed by a second superconducting solenoid, the detector magnet. An overview of the detector system can be seen in figure 3.6a. The second magnet is operated at $B_{\text{det}} = 3.6\,\text{T}$. To evacuate the detector system, a pump port connected to the vacuum system, is located between both magnets.

The centrepiece of the detector system is the focal-plane detector (FPD), located inside the detector magnet. A picture of the detector wafer is shown in figure 3.6b. β-electrons are detected with a monolithic silicon wafer with a diameter of 90 mm and a thickness of 500 µm. Functioning as a PIN diode, the detector is divided into 148 pixels, each with an equal surface area of $43\,\text{mm}^2$. The FPD has an energy resolution of $(1.637 \pm 0.004)\,\text{keV}$ [58].

For cosmic ray background reduction, the detector is surrounded by an active and a passive background reduction system. Active background attenuation can be achieved via a veto system, triggered by the signal of plastic scintillators. Passive background suppression is realised by a layer of copper and lead shielding [57]. Additionally electrons are boosted, by applying a potential at the post acceleration electrode (PAE), into an energy region with low intrinsic detector background. The post acceleration is usually set to $U_{\text{PAE}} = 10\,\text{kV}$.

Monitor spectrometer

In parallel to the KATRIN spectrometer, a second spectrometer located in a building next to the main hall, is monitoring the stability of the retarding potential. With a length of 4 m

and a diameter of 1 m, the construction comprises of two 6 T superconducting solenoids, achieving the same energy resolution as the main KATRIN setup.

The main spectrometer and the monitor spectrometer are connected via a voltage divider and kept at the same potential. By observing the mono energetic K32 calibration line, the source can be used to monitor the stability of the width and the position of the krypton line. Thereby allowing drifts to be detected instantly. The K32 line is produced by a ^{83m}Kr source, installed inside the monitor spectrometer. The monitor spectrometer was the main MAC-E filter spectrometer from the former Mainz experiment [76], which took data from 1997 – 2001.

3.3 The TRISTAN project

The KATRIN experiment is designed to measure the effective neutrino mass. By adapting the setup, it is possible to use the KATRIN experiment, in order to search for sterile neutrinos. Following the current neutrino mass measurements, the KATRIN collaboration is preparing for improved sensitivity sterile neutrino measurements, prospectively in 2025. To search for keV-sterile neutrinos it is necessary to look deeper into the tritium spectrum. By measuring in a lower energy range, a much higher count rate compared to standard neutrino mass measurements close to the endpoint have to be expected. High electron rates and higher surplus energies come with severe challenges, such as higher pile-up, higher backscattering rates, non-adiabatic behaviour, more scattering in the source, and non linearities of the detector, all of which lead to distortions of the measured spectrum. As the current detector system with a 148-pixel FPD is only capable of handling a maximum count rate of up to 10^5 cps over the whole detector, lower retarding potentials are a challenge for the detector and read-out system. It is only possible to look deeper into the spectrum with the current setup by reducing the column density of the WGTS. To use the full unprecedented source strength and its luminosity (10^{11} decays per second), a new detector system is required. In order to be sensitive to small mixing amplitudes of a keV-scale sterile neutrino, the system has to be capable of handling high count rates while maintaining a high energy resolution.

The goal of the TRISTAN sub-project is to develop a new detector and read-out system, designed to be able to handle high count rates, up to 10^8 cps, with an extraordinary high energy resolution close to the Fano-limit[1]. To have a reasonably low number of pile-up events, a maximum of 100 kcps for each detector pixel is foreseen [84]. Optimising the design of the silicon drift detector (SDD) and detector layout in respect to charge sharing and energy resolution, as well as an optimal surface coverage, led to a hexagonal pixel shape. The SDD consists of an n-doped bulk material, a (p^+)-doped backplane, as well as an (n^+)-doped central contact point for each pixel. The centre contact point is circularly surrounded by (p^+)-doped steering electrodes, guiding generated electrons along field lines to the centre point [34]. In the final detector layout, each of the pixels will have a diameter of about 3 mm. Figure 3.7b shows a sketch of the final detector layout. In the final layout, the detector is divided into modules, in a diameter of approximately 20 cm. Each module is containing 166 pixels, giving a total number of almost 3500 pixels. This layout is arranged in a way to give maximum coverage of the flux tube diameter while guaranteeing a minimum dead area inside the array.

First TRISTAN detector prototypes have been fabricated in the semiconductor lab of the Max Planck Society (HLL) and are currently being characterised. The prototypes

[1] The Fano limit describes the theoretical minimum for the relative dispersion of a in comparison to the measured energy.

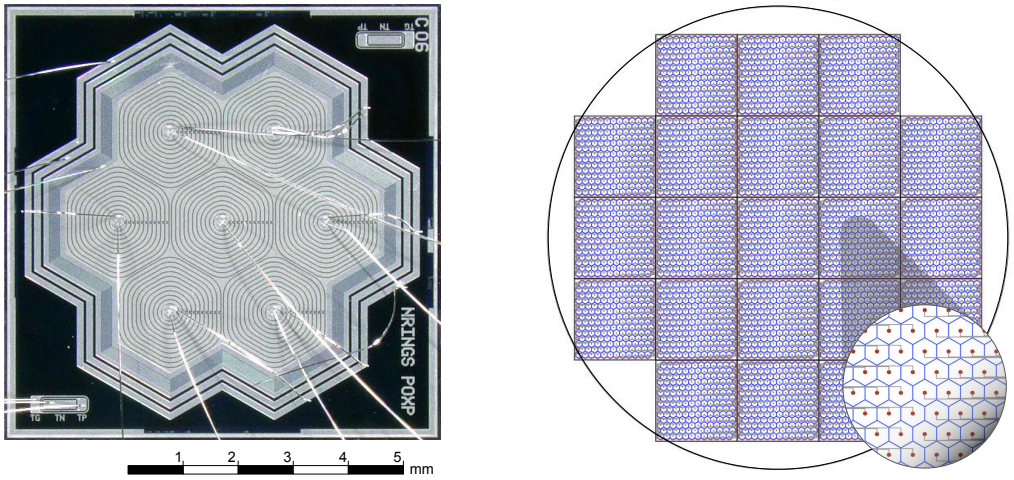

(a) 7-pixel TRISTAN prototype. **(b)** Final TRISTAN detector layout.

Figure 3.7: (a) Read-out side of the 7-pixel TRISTAN detector prototype. The SDD was produced by the HLL of the Max-Planck-society. Each hexagonal pixel has a diameter of 2 mm and is bonded in the centre [63]. **(b)** Detector layout of the final TRISTAN detector. The detector, with a diameter of about 20 cm, is divided into 21 detector modules, each equipped with 166 pixels, giving a total of almost 3500 hexagonal shaped pixels. Each of the pixels on the final detector are foreseen to have a diameter of 3 mm. The final TRISTAN detector system is expected be able to handle a maximum count rate of up to 10^8 cps, which is an increase by 10^3 cps in comparison to the current FPD (figure adapted from [97]).

consist of 7 pixels, each with a diameter of 2 mm. Figure 3.7a shows the read-out side of the current TRISTAN prototype, where one can see the layout of the steering rings, surrounding the central contact point of each pixel. For the current prototypes a special read-out system by XG-Lab is used, amplifying the detector signal in two stages before the data-acquisition (DAQ). First characterisations give and energy resolution of 139 eV at 5.9 keV, measured with the X-ray lines of a ^{55}Fe source. Furthermore the detector shows excellent linearity, as well as a negligible level of leakage current at $-30\,^{\circ}$C [84]. First TRISTAN detector prototypes have also been used in measurements at the Troitsk neutrino-mass experiment [9].

4. Search for keV-scale sterile neutrino in "first tritium" at KATRIN

With its highly active and stable tritium source, the KATRIN experiment is designed to give high energy resolution in a region close to the endpoint. With the TRISTAN project, the KATRIN collaboration is currently preparing for sterile neutrino measurements in the future as the current detector system has readout limitations with a maximum read-out speed of 100 kcps for the whole detector. By adapting the experimental conditions, it is still possible to use the KATRIN setup with the current detector system to get a first insight deeper into the tritium spectrum.

This chapter discusses the challenges when looking deeper into the spectrum. Furthermore the objective of the "first tritium" campaign will be outlined, as well as dedicated sterile neutrino measurements performed during the measurement campaign. The physics model and the analytical methods will be described, which are subsequently used to fit the data, including systematic uncertainties. Furthermore, the statistical sensitivity will be compared to the exclusion limit calculated from the measured data. Finally, the influence of systematic uncertainties will be discussed.

4.1 Challenges finding keV-scale sterile neutrinos

The search for sterile neutrinos in the keV mass range, with KATRIN, comes with several challenges. KATRIN is designed to deliver a high count rate for the neutrino search in the endpoint region, with a decay rate of $\sim 10^{11}\,\mathrm{s}^{-1}$ in the source. Measuring deeper in the spectrum, a higher count rate is expected. High count rates per pixel have significant drawbacks, as they result in distortions of the spectrum due to pile-up effects and therefore are a severe problem. The effect of pile-up will be discussed in section 4.3.3. The DAQ also has limited read-out speed for the FPD and thus a maximum event rate of 100 kcps for the whole detector [10]. In order to keep pile-up effects in an acceptable range, a maximum count rate of 3 kcps per pixel should not be exceeded. This gives limitations to the lowest possible retarding potential that can be set.

Furthermore, electrons with a high surplus energy above the retarding potential are more likely to show non adiabatic behaviour if the magnetic gradient is not reduced. Having non adiabatic electrons changes the transmission probability, and should be avoided. The adiabatic transport can be improved with a reduced B-field inside the source, because the acceptance angle for electrons becomes smaller, or by adapting the LFCS field. Another effect with a more significant role deeper in the spectrum is scattering in the WGTS. Scattered electrons are still able to reach the detector due to their high energy and thus change the spectral shape.

4.2 “First tritium” campaign

The “first tritium” (FT) campaign at KATRIN took place in June 2018. The objective of the campaign was to operate the complete experimental KATRIN setup with a constant tritium injection into the WGTS. For the first time tritium was successfully circulated in the LOOPS system and continuously injected into the source via the buffer vessel. Additional goals included testing the ion retention and ion blocking systems, taking tritium scans with the FBM, validating the stability requirements of the system, and taking scans of the tritium spectrum with the FPD [72]. Dedicated keV-scale sterile neutrino scans were performed, measuring the tritium spectrum down to 2.6 keV and 4.0 keV below the endpoint.

During the FT campaign, the WGTS was operated with a column density of $4.47 \times 10^{21}\,\mathrm{m}^{-2}$, corresponding to a gas throughput of 1.86 mbar l/s and a DT-concentration of 1 %. In the standard FT-mode, scans were performed down to 1.60 keV below the endpoint. In addition, looking deeper into the spectrum, while obtaining a high count rate comes with many disadvantages. In order to keep the pile-up rate as small as possible while keeping a stable source strength, the measurements were performed with a column density of 50 % and 25 %. Scattering inside the source with reduced column densities is less likely. An overview of runs with reduced column density is shown in appendix A. Furthermore, a summary of the parameter settings during the sterile neutrino measurements with reduced column density of 25 % is shown in table 4.1. The measurements with a 25 % column density ($1.1 \times 10^{21}\,\mathrm{m}^{-2}$) are analysed in detail in this work. To restrict the maximum electron count rate, the sterile neutrino scans were performed down to 4 keV, leading to a maximum count rate of $\sim$ 2.59 kcps/pixel. This was combined with a setting of the magnetic fields in the analysing plane to $B_{\mathrm{ana}} = 14.5\,\mathrm{G}$. The electron transport is fully adiabatic, when using this setting [65].

Table 4.1: Settings for the sterile neutrino measurements during “first tritium” with reduced column density to 25 %.

Parameter	Set value
B_{ana}	14.5 G
B_{max}	4.2 T
B_{source}	2.52 T
ρd	$1.1 \times 10^{21}\,\mathrm{m}^{-2}$
DT-fraction	1.0 %
HT-fraction	0.0 %
T_2-fraction	0.0 %

The deep scans had a maximum count rate of $\sim$ 2.59 kcps/pixel at a retarding potential of 4.0 kV. Scaling up to the whole detector, this would result in a total count rate of $\sim$ 384 Mcps, which exceeds the maximum read-out speed of 100 kcps. To be able to read out and process the data efficiently with the current DAQ, and to minimise losses within the read-out process, only the detector bulls eye and the inner two rings were read out, equivalent to the pixel numbers 0 to 27. This gives a maximum total count rate of 72.59 kcps, read out by the DAQ, which is in the limit given by the design specifications.

A measurement time distribution (MTD) with equidistant retarding potential increments was chosen, with two additional measuring points, close to the endpoint and in the background region. Due to lower count rates and therefore smaller statistics, rates are measured for a longer time in the endpoint region. The corresponding MTD is illustrated

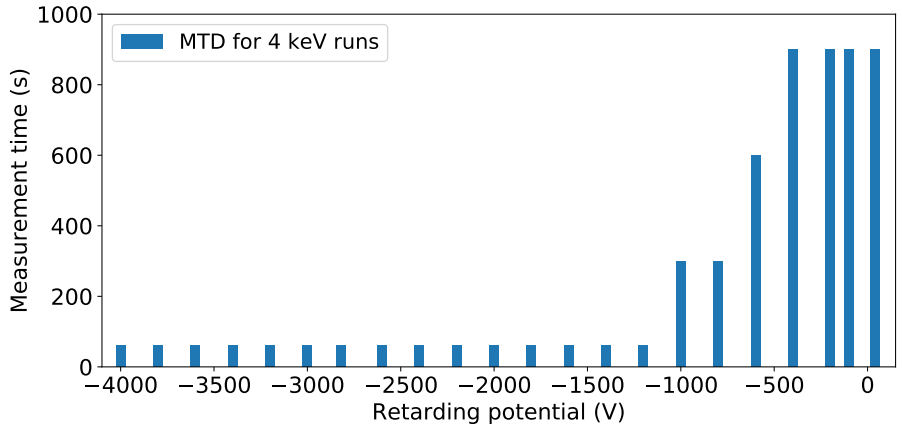

Figure 4.1: MTD during the sterile neutrino runs during the FT campaign. The MTD consists of 21 measurement points, equally distributed, with two additional measuring points close to the endpoint and in the background region. As rates closer to the endpoint are smaller, the measuring time is longer in these regions, whereas the measuring time deeper in the spectrum is reduced, due to high count rates.

in figure 4.1. More detailed values can be seen in appendix B. The total measurement time for one 4 keV-run is 5700 s.

4.3 Physics model

It is important to know the underlying model of the KATRIN experiment, and how the components change the spectral shape in its final form, such as the response of the source and spectrometer, or the response of the detector. The following sections will describe the tritium decay model, with regard to sterile neutrinos, as well as the influence of the experimental setup, and the detector response.

4.3.1 The β-decay model

The β-decay rate can be derived by using Fermi's golden rule. The rate $\Gamma_{i\to f}$ is given by the transition probability from the initial $\langle i|$ into the final eigenstates $|f\rangle$. In first order perturbation theory, this can be written as:

$$\Gamma_{i\to f} = 2\pi\rho(E_f)|\langle i|\, M\, |f\rangle|^2 = 2\pi\rho(E_f)|M_{if}|^2. \tag{4.1}$$

M_{if} corresponds to the transition matrix element between the initial and the final states. In the equation $\rho(E_f)$ is the density of final state. Calculating the final state distribution (FSD), as well as deriving the transition matrix elements over leptonic and nuclear transitions and rearranging equation 4.1 for E, leads to the following expression for the differential decay rate for tritium:

$$\begin{aligned}\frac{\mathrm{d}\Gamma}{\mathrm{d}E} = \frac{\mathrm{d}^2N}{\mathrm{d}E\mathrm{d}t} &= C\cdot F(E,Z=2)\cdot p\cdot(E+m_\mathrm{e})\cdot(E_0-E)\\ &\quad\cdot\sqrt{(E_0-E)^2-m^2_{\bar{\nu}_\mathrm{light}}}\cdot\Theta(E_0-E-m_{\bar{\nu}_\mathrm{light}}).\end{aligned} \tag{4.2}$$

In this equation, E_0 represents the endpoint of the tritium spectrum, m_e corresponds to the electron mass, and $m_{\bar{\nu}_\mathrm{light}}$ to the effective antineutrino mass. A more detailed derivation can be found in [39]. The Fermi function $F(E,Z)$ gives corrections of the spectrum due

to electromagnetic interactions of the electron with the daughter nucleus. In the case of tritium decay, the daughter nucleus is He^+, with the atomic number $Z = 2$. A Heaviside function Θ is added to ensure the conservation of energy, which confines the spectrum to a physical solution, where a neutrino can only be generated if the remaining energy is greater than the neutrino mass [58]. C is equivalent to a normalisation and can be written as

$$C = \frac{G_F^2}{2\pi^3} \cdot \cos^2(\theta_C) \cdot |M_{nuc}|^2. \tag{4.3}$$

Here G_F is the Fermi coupling constant, θ_C is the Cabibbo angle, and M_{nuc} denotes matrix element for nuclear transition. With the assumption of unitarity of the neutrino mass eigenstate $\sum_i \left|U_{ei}^2\right| = 1$, the flavour eigenstate $m_{\overline{\nu}_e}^2$ can be written as the superposition of the three mass eigenstates

$$m_{\nu_{light}}^2 = \sum_{i=1}^{3} \left|U_{ei}^2\right| m_{\nu_i}^2, \tag{4.4}$$

with the probability U_{ei} to have one of the eigenstates ν_i. As one can see in equation 4.2 the effective neutrino mass $m_{\nu_{light}}$ is an observable of the differential decay rate for the β-decay. Figure 2.8 illustrates the influence of the neutrino mass on the differential tritium spectrum. To include a heavy sterile neutrino in the β-decay model, unitarity of the mass eigenstates applies to all eigenstates, including heavy sterile neutrinos. The mixing amplitude is given by:

$$\text{light}: \quad \sum_{i,\,\text{light}} \left|U_{ei}^2\right| =: \cos^2(\theta), \tag{4.5}$$

$$\text{heavy}: \quad \sum_{i,\,\text{heavy}} \left|U_{ei}^2\right| = 1 - \sum_{i,\,\text{light}} \left|U_{ei}^2\right| = \sin^2(\theta). \tag{4.6}$$

Since the differential decay rate is proportional to the squared neutrino mass, a spectrum including a light and a heavy sterile part can be formed by multiplying the components with the according mixing amplitude. This leads to the following spectrum:

$$\frac{d\Gamma}{dE} = \cos^2(\theta) \cdot \frac{d\Gamma}{dE}(m_{light}) + \sin^2(\theta) \cdot \frac{d\Gamma}{dE}(m_{heavy}). \tag{4.7}$$

Figure 2.13 illustrates the imprint of a sterile neutrino on the β-decay spectrum of tritium.

4.3.2 Source and spectrometer response

In the KATRIN experiment the count rate of the integrated spectrum is measured. The Integrated count rate for a MAC-E-filter system is given by:

$$\frac{dN_s(qU)}{dt} \propto \int_{qU}^{E_0} \frac{dN}{dE\,dt} \cdot T(E, qU) \cdot dE. \tag{4.8}$$

This equation represents a folding of the differential decay rate of tritium, given by equation 4.2, and the Transmission probability $T(E, qU)$ of the spectrometer. The transmission function $T(E, qU)$ can be calculated from the magnetic field inside the source B_{source}, the magnetic field in analysing plane B_{ana}, which is located in the centre of the main spectrometer, as well as the maximum magnetic field B_{max}, given by the magnetic field

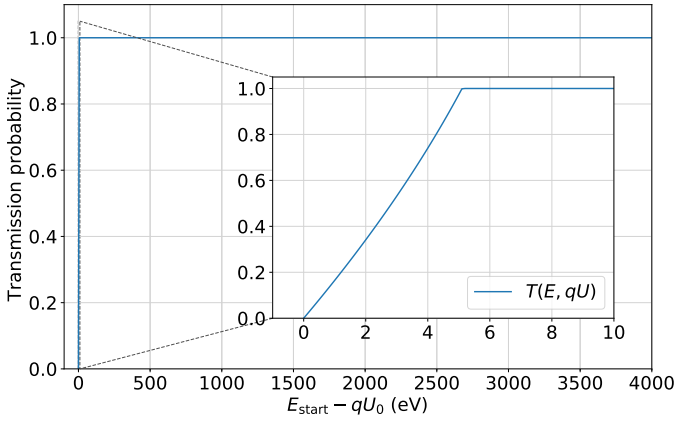

(a) Transmission function $T(E, qU)$.

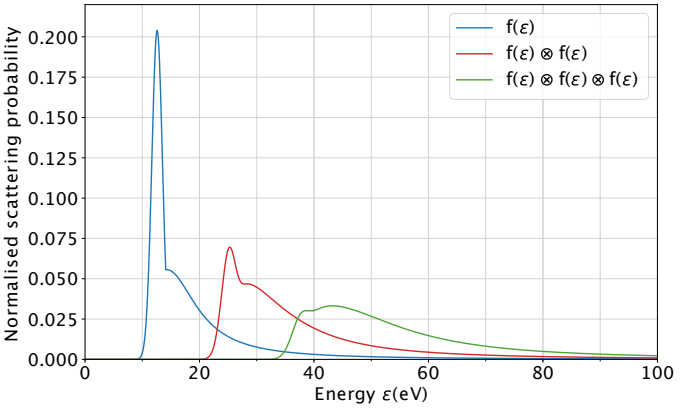

(b) Energy loss function $f(\varepsilon)$.

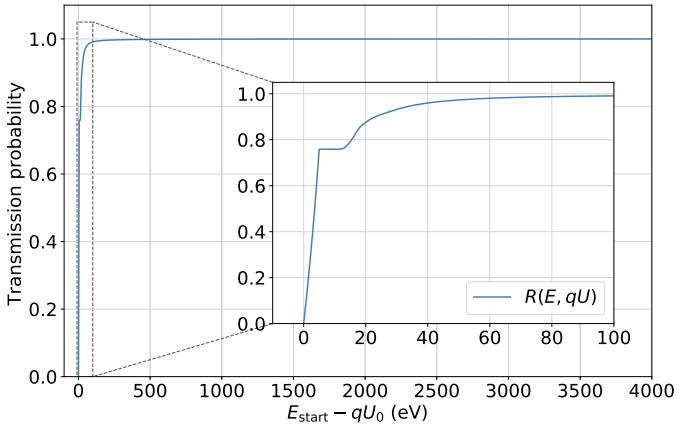

(c) Response function $R(E, qU)$.

Figure 4.2: (a) Plot of the transmission function for a given surplus energy ($E_{\text{start}} - qU$), described by equation 4.9, calculated for the 14.5 G setting with a retarding energy of 14.575 keV. **(b)** Illustration of the energy loss function $f_1 = f(\varepsilon)$ for one scattering (blue), two scatterings (red) and three scatterings (green), given by [11]. All probability distributions have been normalised $\int_0^\infty f(\varepsilon) \cdot \mathrm{d}\varepsilon = 1$. Higher orders are given by convoluting the energy loss function i-times. **(c)** Plot of the transmission probability given by the KATRIN response function with the 14.5 G setting and a retarding energy of 14.575 keV. The KATRIN response function can be calculated by folding the transmission function with the energy loss functions. The transmission probability was calculated for a retarding potential of 14 575 keV. The calculation assumes a maximum number of 10 scatterings inside the source.

inside the detector magnet.

$$T(E,qU) = \begin{cases} 0 & \text{for } E < qU \\ \dfrac{1-\sqrt{1-\frac{E-qU}{E}\cdot\frac{B_{\text{source}}}{B_{\text{ana}}}}}{1-\sqrt{1-\frac{B_{\text{source}}}{B_{\text{max}}}}} & \text{for } qU \leq E < qU\cdot\dfrac{f_{\text{rel}}\cdot B_{\text{max}}}{f_{\text{rel}}\cdot B_{\text{max}}-B_{\text{ana}}} \\ 1 & \text{for } E > qU\cdot\dfrac{f_{\text{rel}}\cdot B_{\text{max}}}{f_{\text{rel}}\cdot B_{\text{max}}-B_{\text{ana}}} \end{cases}, \tag{4.9}$$

whereas f_{rel} describes the relativistic correction factor [69]:

$$f_{\text{rel}} = \frac{\frac{E-qU}{m_{\text{e}}}+2}{\frac{E}{m_{\text{e}}}+2}. \tag{4.10}$$

In the special case of the KATRIN experiment, the transmission probability $T(E,qU)$ itself has to be folded with the energy loss function $f(\varepsilon)$. The energy loss function describes the electron energy loss ε due to inelastic scattering in the source. It can be parameterised by a composition of a low-energy Gaussian part, corresponding to excitation processes, and a high-energy Lorenzian part, referring to ionisation of tritium molecules [11, 74].

$$f(\epsilon) = \begin{cases} A_1\cdot\exp\left(-2\left(\dfrac{\varepsilon-\varepsilon_1}{\omega_1}\right)^2\right) & \varepsilon < \varepsilon_c \\ A_2\cdot\dfrac{\omega_2^2}{\omega_2^2+4(\varepsilon-\varepsilon_2)^2} & \varepsilon \geq \varepsilon_c \end{cases}. \tag{4.11}$$

Convolving both, the transmission function and the energy loss function leads to an expression for the KATRIN response function:

$$R(E,qU) = T(E,qU)\otimes(P_0 + P_1\cdot f(\varepsilon) + P_2\cdot f(\varepsilon)\otimes f(\varepsilon) + \dots). \tag{4.12}$$

For an electron passing through the source without scattering, the response is given by the transmission function multiplied with the probability of no scattering P_0. Whereas, for electrons scattering i-times, the transmission function is multiplied with the probability to scatter i-times (P_i) and folded with the energy loss function for each scattering [64].

Therefor the integrated spectrum for the KATRIN experiment is given by:

$$\frac{\mathrm{d}N_{\text{s}}(qU)}{\mathrm{d}t} \propto \int_{qU}^{E_0}\frac{\mathrm{d}N}{\mathrm{d}E\mathrm{d}t}\cdot R(E,qU)\cdot\mathrm{d}E, \tag{4.13}$$

folding of the differential decay rate of tritium, given by equation 4.2, and the response function $R(E,qU)$ of the experiment. As the rate is measured over a certain time t_{qU}, the rate has to be integrated over t, which leads to

$$N_{\text{s}}(qU) \propto t_{qU}\int_{0}^{E_0}\frac{\mathrm{d}N}{\mathrm{d}E}\cdot R(E,qU)\cdot\mathrm{d}E. \tag{4.14}$$

However the spectrum given by equation 4.14 does not take the background rate N_{b} into account. For the total number of counts, background counts have to be added to the counts emerging from the tritium decay,

$$N_{\mathrm{tot}}(qU) = N_{\mathrm{s}}(qU) + N_{\mathrm{b}}(qU). \tag{4.15}$$

As the KATRIN background is originating from Poissonian distributed processes, with a constant decay rate of Γ_{bkg}, the background rate is given by:

$$N_{\mathrm{b}} = t_{qU} \cdot \Gamma_{\mathrm{bkg}}. \tag{4.16}$$

4.3.3 Detector response

As well as the source and the spectrometer, the detector also has an effect on the measured energy spectrum, and distorts the spectrum in a particular way. Figure 4.3 shows the shape of the energy spectrum measured by the FPD and its distinct characteristics. To first order, the detector is approximated with an energy independent detection efficiency ($\varepsilon_{\mathrm{const}}$ = const.), usually around 0.90 – 0.95. Additionally, energy dependent and rate dependent corrections are accounted for in analyses.

The time resolution of the detector is given by the detector read-out electronics, and the shaping time. The current read-out system is operated with a shaping time of ($t_s = 1.6\,\mu\mathrm{s}$). Two impinging electrons within the shaping time can not be resolved separately, their energy is thus combined, and they are detected as a single electron with higher energy E:

$$E = E_1 + \xi \cdot E_2. \tag{4.17}$$

Depending on the arrival time of the electron, only a fraction ξ of the energy of the second electron is added to the first. In the measured energy spectrum this results in the overlay of a secondary energy spectrum, with double the peak energy. This efficiency is called pile-up. The pile-up structure can be seen in figure 4.3. A pile-up model can be approximated via an exponential probability density function, dependent on the rate R and the shaping time t_s [42, 75]:

$$\varepsilon_{\mathrm{pu}}(R) = \exp\left(-2R \cdot t_s\right). \tag{4.18}$$

In the following analysis, a rate dependent detection efficiency $\varepsilon_{\mathrm{pu}}(R)$, to correct for pile-up, as well as an energy dependent detection efficiency $\varepsilon_{\mathrm{ROI}}(qU)$, resulting from the region of interest cut is used. The energy dependent detection efficiency will be discussed more in detail in section 4.5.1. With the corrections, the detection efficiency is given by:

$$\varepsilon_{\mathrm{det}} = \varepsilon_{\mathrm{const}} \cdot \varepsilon_{\mathrm{pu}}(R) \cdot \varepsilon_{\mathrm{ROI}}(qU). \tag{4.19}$$

Combining all derivations from above, the integrated tritium spectrum is:

$$I(qU) = C \cdot \int_{qU}^{E_0} D(E) \cdot R(E, qU) \cdot \mathrm{d}E, \tag{4.20}$$

multiplied by a constant prefactor C, given by:

$$C = N_{\mathrm{eff}} \cdot \frac{1 - \cos\theta_{\mathrm{max}}}{2} \cdot \varepsilon_{\mathrm{det}} + \Gamma_{\mathrm{bkg}}. \tag{4.21}$$

The first part gives the effective number of tritium atoms in the source within the flux tube, where $N_{\mathrm{eff}} = 2 \cdot A_{\mathrm{eff}} \cdot \rho d$, with the column density ρd inside the source and the effective area of the flux tube inside the source A_{eff}. The second part corrects the spectrum to the decreased solid angle, given by the reduced maximum acceptance angle θ_{max} calculated using equation 3.5, and the third part corrects the spectrum by the detection efficiency.

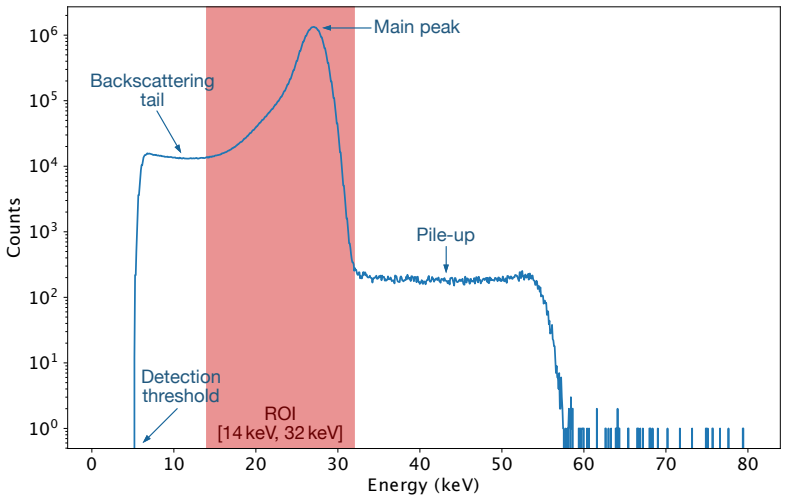

Figure 4.3: Characteristics of the energy spectrum measured by the FPD (measured at $U_{\mathrm{ret}} = 16.975\,\mathrm{keV}$). Electrons are only detected above the detection threshold. Backscattered electrons are depositing only a fraction of their energy, thus resulting in a low energy backscattering tail. The majority of electrons are able to deposit their complete energy, resulting in the main peak. Multiplicity events result in a pile-up structure. Here the pile-up structure of two electron events is clearly visible.

4.4 Analysis strategy

The analysis of the tritium β-decay spectrum in this work is predominantly based on Fitrium [69], a custom fitting tool developed by C. Karl and M. Slezák at the Max-Planck-Institute for Physics (MPP) in Munich, in order to deliver customised fitting of the integrated tritium spectrum as well as robust error propagation of systematic uncertainties. The following sections will explain the statistical methods used to fit the model to the measured data and the possible methods of handling systematic uncertainties.

4.4.1 Likelihood estimation and minimisation

To fit the theoretical model to the measured data with Fitrium, the negative log likelihood function for the model and data is estimated and minimised. The implementation of the likelihood estimation, and minimising algorithms are implemented in Fitter. The Fitter library includes a maximum likelihood estimator and provides likelihood estimation for Poisson and Gauss distributed data.

For independent measurements the likelihood $\mathcal{L}$ is given by the product of the probability density functions:

$$\mathcal{L}(d|\theta) = \prod_{I=1}^{n} P(d_i|\theta), \tag{4.22}$$

with a given probability density function $P(d|\theta)$ for measured data d_i and the dependency to the parameter θ. In order to find the optimal value for $\theta_{\mathrm{optimal}}$ the likelihood function has to be maximised. As it is technically better to manage monotonically increasing functions, it is more practical to use the logarithm of the likelihood function. Furthermore the problem can be inverted to a minimisation by taking the negative logarithm of the likelihood:

$$-\ln \mathcal{L}(d|\theta) = -\sum_{I=1}^{n} \ln P(d_i|\theta). \tag{4.23}$$

Therefore maximising the likelihood is equivalent to minimising the negative log likelihood. The minimum for θ is given by:

$$\frac{\mathrm{d}}{\mathrm{d}\theta}\left(-\ln \mathcal{L}(d|\theta)\right) = 0. \tag{4.24}$$

In the case of small statistics, the Poissonian approach is more accurate. The negative log likelihood for Poisson data d in respect to the fit parameters θ and the model $m(\theta)$ is defined as follows:

$$-\ln \mathcal{L}(d|\theta)_{\text{Poisson}} = -\sum_i \ln f(d_i|\theta) = \sum_i \left[m_i(\theta) - d_i + d_i \ln\left(\frac{d_i}{m_i(\theta)}\right)\right] = \frac{1}{2}\cdot D. \tag{4.25}$$

For Poisson distributed data, the negative log likelihood is proportional to the deviation D. In the limiting case of $d_i \to 0$ the negative log likelihood becomes:

$$-\ln \mathcal{L}(d|\theta)_{\text{Poisson}} = \sum_i m_i(\theta). \tag{4.26}$$

This is only defined for $m_i(\theta) \geq 0$. In the case of normal distributed data, the negative log likelihood is proportional to the χ^2.

$$-\ln \mathcal{L}(d|\theta)_{\text{normal}} = \frac{1}{2}\sum_i \left(\frac{m_i(\theta) - d_i}{\sigma_i}\right) = \frac{1}{2}\cdot \chi^2. \tag{4.27}$$

In the case of large statistics N, it can be assumed that the Poisson likelihood estimation approximates the likelihood for normal distributed data, with a statistical error of $\sigma = \sqrt{N}$.

$$-\ln \mathcal{L}(d|\theta)_{\text{normal}} \approx -\ln \mathcal{L}(d|\theta)_{\text{Poisson}}. \tag{4.28}$$

To find the optimal value for θ, the deviation D, in the case of Poisson distributed data, and χ^2, in the case of normal distributed data, have to be minimised. The minimisation is performed via a quasi-Newtonian method. A custom gradient based minimiser based on inexact line search and the Broyden-Fetcher-Goldfarb-Shanno algorithm (BFGS) determines the minimum of the likelihood function [23].

4.4.2 Fitrium software

Fitrium is a custom analysis tool developed at the Max-Planck-Institute for Physics (MPP) in Munich. Fitrium is based on the boost-library and uses the Fitter framework, a custom gradient-based minimiser. For efficient data processing and multithreading, Fitter and Fitrium are both written in C++. Fitrium is designed to be able to generate Monte Carlo datasets from the underlying physics model, as well as fitting the model to generated or measured data.

The physics model, outlined in section 4.3, is implemented alongside with various underlying components which can be selected to analyse data. It includes FSDs of various isotopologues, such as HT [103], DT [37], and T_2 [37, 103], to build the β-decay spectrum. Furthermore folding of the β-spectrum with the source and spectrometer response derived form the transmission function and the energy loss function are implemented, as described in section 4.3.2, as well as energy dependent scattering probabilities. The code also uses a pixel dependent detection efficiency, described in sections 4.3.3 and 4.5.1, and includes Doppler broadening.

As well as providing simulation of physics model, the Fitrium code gives different possibilities to fit and combine datasets. To fit the data, count rates measured by each pixel can be fit to the model for each individual pixel, or pixels can be combined to fit a uniform model to the detector. It is also possible to create a model for the whole detector, with an individual normalisation and background for each pixel, giving a total of 298 parameters to fit with a combined likelihood. When analysing multiple runs, each run can be fit individually, or runs can be combined. They are combined either via stacking, by adding up counts for the same retarding potentials, or combining via appending, by fitting the model to data points of multiple runs analogous to fitting a single run.

Fitrium includes options to take systematic uncertainties into account. Firstly, systematic uncertainties can be implemented via Monte Carlo propagation of errors. The second option is to include systematic uncertainties via the nuisance parameter method, by adding pull terms into the likelihood. The third method is to take systematics into account via a covariance matrix approach. A more detailed description of the Fitrium code, its structure, and the different approaches and underlying components can be found in [69].

4.4.3 Exclusion limit settings

To calculate an exclusion limit for a sterile neutrino, fits are preformed with fixed combinations of the sterile neutrino mass and mixing amplitude ($\sin^2\theta$, m_{heavy}), and free fit parameters for the background, the endpoint and the normalisation. For a 90 % CL with two degrees of freedom, the criteria for the exclusion limit is given by:

$$\Delta\chi^2 = \chi^2 - \chi^2_{\text{NH}} \leq 4.60. \tag{4.29}$$

Hereby the χ^2 for a combination of $\sin^2\theta$ and m_{heavy} is compared to the χ^2 for the null hypothesis χ^2_{NH} ($\sin^2\theta = 0$, $m_{\text{heavy}} = 0$). Translating this into the negative log likelihood, the following equation gives the condition for the 90 % CL exclusion limit on the sterile neutrino parameter space

$$\text{with } \left(-\ln\mathcal{L} = \frac{1}{2}\cdot\chi^2\right): \qquad \Delta\left(-\ln\mathcal{L}\right) = \left(-\ln\mathcal{L}\right) - \left(-\ln\mathcal{L}\right)_{\text{NH}} \leq 3.20. \tag{4.30}$$

For the scans, the neutrino mass is fixed to zero. Experimental parameters that go into the model are determined by slow control measurements. The influence of systematic uncertainties is handled via the covariance matrix method.

4.5 Systematic uncertainties

This section will discuss the selection of measured data, as well as the size of systematic uncertainties that have been taken into account in the analysis. For this thesis, systematic uncertainties have been implemented via the covariance matrix approach. The calculation method of covariance matrices is furthermore outlines. The resulting covariance matrices are subsequently shown for each systematic uncertainty.

4.5.1 Uncertainty of the pixel dependent detection efficiency

As shown in figure 4.3, the measured detector response contains distinct characteristics, like a main peak, a backscattering tail and a pile-up tail. The main peak position is given by the retarding potential plus the post acceleration. In first instance, the whole spectrum is recorded and stored. With a region of interest (ROI) cut various energy ranges can be excluded from the measured data and thus reduce the influence of certain systematic

effects. The upper limit of the ROI cuts off a significant number of multi electron events which cause a pileup structure in the measured energy spectrum. The lower ROI bound cuts off a part of the backscattering tail in the energy spectrum. Ideally the ROI is only in a small range close to the peak energy and thus the retarding energy, plus the additional energy added by post acceleration. This has the advantage that most of the backscattering events and pile-up events are cut away.

Every pixel of the FPD has an individual response and thus the peak position and the energy resolution can vary. Furthermore, as a continuous tritium spectrum is measured at the detector, the spectrum is a result of electrons with energies below the retarding energy, leading to a distorted spectral shape. Applying a ROI therefore results in different efficiencies, depending on the pixel, and the retarding potential. This efficiency can be described with:

$$\varepsilon_{\mathrm{ROI}}(qU) = \frac{N_{qU}[\mathrm{ROI}]}{N_{E_0}[\mathrm{ROI}]}, \tag{4.31}$$

whereas $N_{qU}[\mathrm{ROI}]$ is the number of counts inside the ROI for a retarding potential qU and $N_{E_0}[\mathrm{ROI}]$ the number of counts in the ROI at the endpoint.

To measure the magnitude of detection inefficiency caused by a ROI cut, a high statistics stability run (run 40970) was used. The stability run was performed at a retarding potential of $-16\,975\,\mathrm{V}$, with a post acceleration electrode (PAE) potential of $10.0\,\mathrm{kV}$.

Pixel dependence

Figure 4.4 compares the relative efficiency for each pixel with two different ROI cuts. The relative efficiency is calculated by scaling the count number to the pixel with the highest count number. Subfigure 4.4a shows the relative efficiency of each pixel for a narrow region [23.975 keV, 29.975 keV]. In direct comparison subfigure 4.4b gives the relative efficiency with a ROI fixed to [14.000 keV, 32.000 keV]. An illustration of the FPD coloured according to the relative efficiency, indicates pixel dependent differences of the efficiency. The outer two rings, as well as the pixels 100, 112, and 123, show an efficiency significantly lower than the rest of the FPD. The low efficiency on the outer two rings is the result of misalignment and dimensions of the magnetic flux tube being smaller that the surface coverage of the FPD. Therefore less β-electrons reach the detector in these areas. The inefficiency on the right detector side (pixels 100, 112, and 123) are due to the "shadow" casted by the FBM positioned inside the beam tube, resulting in lower statistics for these pixels. For all FT runs these pixels are removed from the analysis. Both of the lower plots in figure 4.4 give the values for the relative efficiency and show that several of the pixels in the outer detector region have an efficiency below 0.9.

Selecting a narrower ROI also results in larger deviations of the efficiencies, causing in a ring-like structure. This can be traced back to a deviation of the peak positions of the pixel-wise energy spectra. Figure 4.5a shows the peak positions for each pixel. In the case of a narrow ROI, peak deviations have direct repercussions on the relative efficiency. The pixel dependent peak shifts occurred after Penning trap measurements, seemingly caused by a Penning trap discharge in 2017. This shift could be a result of damages to the wafer surface [73]. By accepting events inside a wider ROI, pixel-wise deviations become smaller since deviations of the peak position have a smaller influence. The relative efficiency is more homogeneous, and the ring structure disappears. Both of the lower plots in figure 4.4 illustrate the effect of a wider ROI resulting in a relative efficiency (~ 1) for most of the pixels. However this neglects the energy dependence of the detection efficiency.

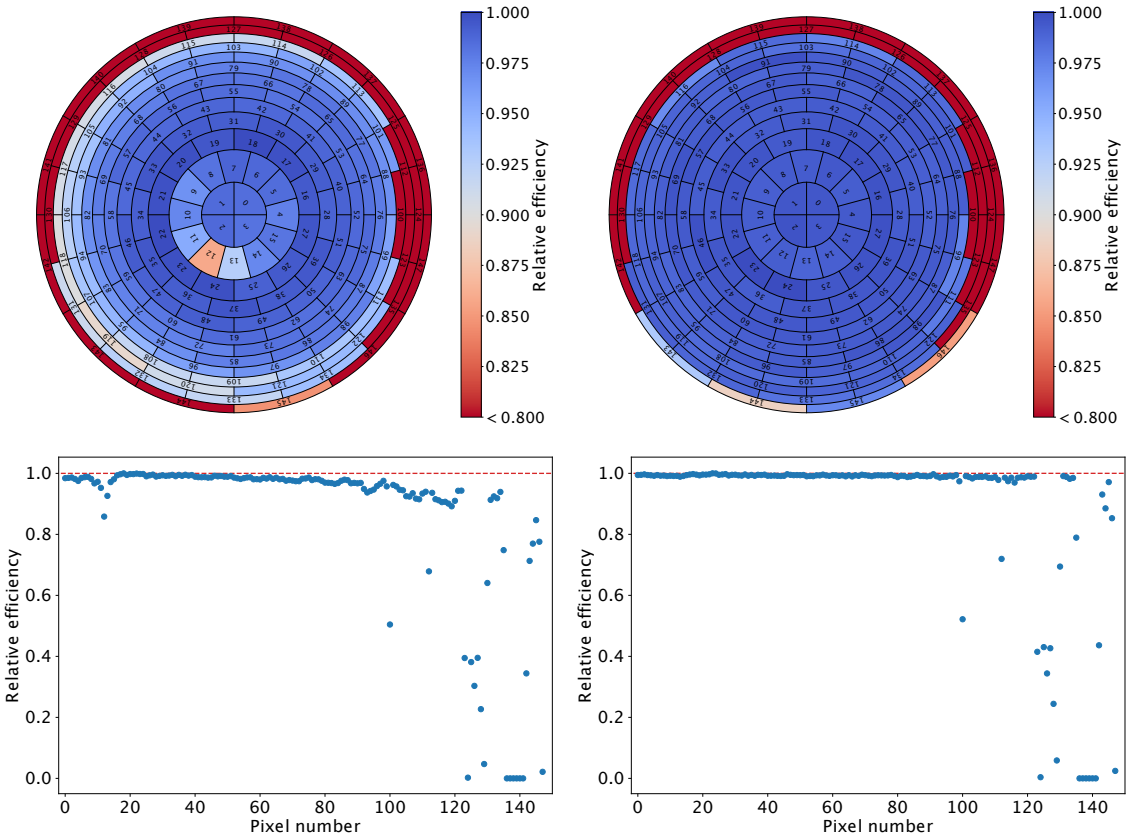

(a) ROI: [23.975 keV, 29.975 keV]. **(b)** ROI: [14.000 keV, 32.000 keV].

Figure 4.4: Relative pixel-wise efficiency calculated from a high statistics stability run (run 40970), scaled to the pixel with the highest count number. **(a)** Relative efficiency for a narrow ROI from −3.0 keV below the expected peak position, to +3.0 keV above the expected peak position. **(b)** Relative efficiency for a broader ROI fixed to 14.0 keV – 32.0 keV. The dashed red line reflects an efficiency of 100 %, corresponding to the pixel with the highest count number. By increasing the ROI width, the relative efficiency becomes more homogeneous throughout the detector (figures similar to [41]).

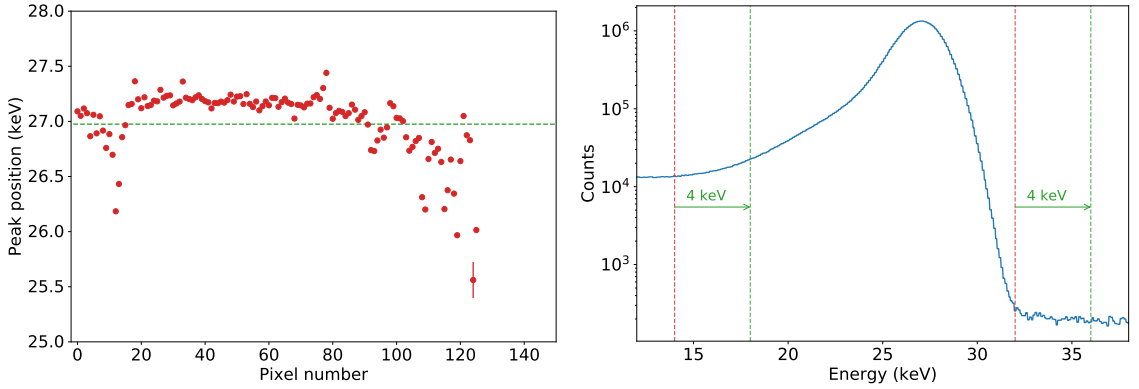

(a) Pixel-wise peak position of the spectra.

(b) Illustration of the sliding energy window method to estimate the energy dependent detection efficiency.

Figure 4.5: (a) Pixel-wise peak position in a high statistics stability run (run 40970), with a retarding potential of 16.975 kV and a PAE voltage of 10.0 kV. The dashed green line is the expected peak position at 26.975 keV, given by the retarding potential and the PAE voltage. The peak position is estimated by a Gaussian fit of the peak region in the energy spectrum. The peak position has not been calculated in the two outer rings, as statistics are too small in these regions. For pixel 9 to 14 a downwards trend of the peak position is observable, whereas pixels 16 to approximately 80 show similar peak positions and upward deviation. Pixels further outside also show a downwards trend. **(b)** Illustration of the sliding energy window method to estimate the energy dependent detection efficiency due to the ROI cut. The figure shows the energy-spectrum in a high statistic stability run (run 40970), summed over all pixels. By moving the ROI to higher energies, spectra at lower retarding potentials are emulated.

Energy dependence

Therefore an alternative method can be used to calculate an energy dependent detection efficiency. To estimate the detection efficiency from measurements, it would be possible to compare reference runs with equivalent statistics. For different retarding energies, the number of counts inside the region of interest for a qU is compared to the number of counts inside the region, with $qU = E_0$. The detection efficiency then would be given by:

$$\varepsilon_{\mathrm{ROI}}(qU) = \frac{N_{qU}[14\,\mathrm{keV},\ 32\,\mathrm{keV}]}{N_{E_0}[14\,\mathrm{keV},\ 32\,\mathrm{keV}]} \tag{4.32}$$

Here N_{qU} describes the number of events at the retarding energy qU in the ROI and N_{E_0} the number of events at the endpoint in the ROI. This approach can only be realised in simulations, as statistics with energies close to the endpoint are too small. Therefore a reverse approach was used to estimate the detection efficiency from measurements. In this approach, a single high statistics run is used. Instead of the moving peak position to lower energies, the ROI is moved to higher energies. This method assumes an independence of the spectral shape from U to first approximation. Figure 4.5b illustrates the method. For this work the energy dependent detection efficiency has been calculated down to 4 keV below the endpoint. By moving the ROI, a greater portion of the backscattering tale is cut off, whereas more pile-up events enter the ROI. In this case, the energy dependent detection efficiency due to the ROI cut is calculated by dividing the counts N inside the shifted ROI by the initial ROI.

$$\varepsilon_{\mathrm{ROI}}(qU) = \frac{N\left[(14\,\mathrm{keV} + qU),\ (32\,\mathrm{keV} + qU)\right]}{N\left[14\,\mathrm{keV},\ 32\,\mathrm{keV}\right]} \tag{4.33}$$

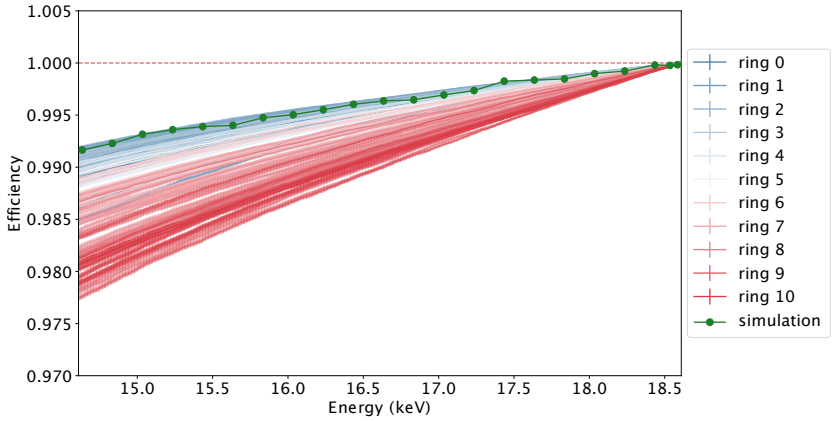

Figure 4.6: Calculated energy dependent detection efficiency for each pixel. The calculated points have been coloured according to the ring number. As statistics on the outer two rings are too low, these pixels were neglected. 4 keV below the endpoint, the detection efficiency varies between 99.2 % and 97.7 %. Comparison of determined detection efficiency form measurements with efficiency determinations from Monte Carlo simulations (green) show good agreement for pixels in the detector centre. For each retarding potential 10^6 electrons were simulated (simulation performed by M. Korzeczek).

This procedure can be executed for each pixel, leading to an energy dependent detection efficiency for each pixel. Figure 4.6 shows the pixel-wise detection efficiency, assuming a constant ROI form 14.0 keV to 32.0 keV. In the figure, each ring is represented by one colour. The detection efficiency varies between 99.2 % and 97.7 % at 4 keV below the endpoint. The plot also shows that pixels further outside have an inferior detection efficiency compared to pixels in the detector centre. For comparison, the detection efficiency from a simulated tritium spectrum is also plotted, using the approach described by equation 4.32. The efficiencies determined via a Monte Carlo simulation and from measured data are consistent and in good agreement for the inner rings, and thus validates the approach to determine the efficiency.

To correct the measured count rate with the detection efficiency due to the ROI cut, the detection efficiency can be included in the constant prefactor C used in equation 4.20.

$$\varepsilon_{\mathrm{det}} = \varepsilon_{\mathrm{const}} \cdot \varepsilon_{\mathrm{pu}}(R) \cdot \varepsilon_{\mathrm{ROI}}(qU) \tag{4.34}$$

A method to calculate the detection efficiency via a reference run independent method and thus independent from the retarding potential of the reference run, is outlined in appendix C.

Uncertainty on the detection efficiency

In the following analysis, the uncertainty on the detection efficiency is included, both, for pile-up and the detection efficiency due to a ROI cut

The uncertainty on the detection efficiency resulting from pile-up $\varepsilon_{\mathrm{pu}}(R)$, is calculated for each datapoint by Gaussian error propagation of equation 4.18:

$$\sigma(\varepsilon_{\mathrm{pu}}(R)) = 2t_s \cdot \varepsilon_{\mathrm{pu}}(R) \cdot \sigma_R. \tag{4.35}$$

Furthermore, the estimated uncertainty on the detection efficiency resulting from a region of interest cut $\varepsilon_{\mathrm{ROI}}(qU)$ is calculated by Gaussian error propagation of equation 4.33, which

Table 4.2: Scale of systematic uncertainties used in this FT analysis for sterile neutrinos.

Parameter	**Systematic uncertainty**
B_{ana}	2.00 %
B_{max}	2.00 %
B_{source}	2.00 %
DT-fluctuation	1.00 %
FSD (onset)	3.00 %
FSD (ground state width)	1.00 %
FSD (excited states)	2.50 %
ε_{pu}	$\sim$ 1.0 ‰
ε_{ROI}	$\sim$ 0.03 %
$\rho d\sigma$	5.39 %

leads to:

$$\sigma(\varepsilon_{\text{ROI}}(qU)) = \varepsilon_{\text{ROI}}(qU) \cdot \sqrt{\frac{1}{N\left[(14+qU),\ (32+qU)\right]} + \frac{1}{N\left[14,\ 32\right]}}. \tag{4.36}$$

4.5.2 Scale of uncertainties

In this subsection, the scale of systematic uncertainties included in the analysis is described. As the uncertainty on the DT-concentration identifies as a major systematic, it is described separately.

Systematic uncertainty on the DT-concentration

Additionally source strength uncertainties were taken into account via DT-fluctuations. For the analysed data the DT-fluctuations were conservatively estimated from the LARA data, with an uncertainty of 1 % for a single run. Furthermore, the uncertainty on DT, is sub-run uncorrelated. Appendix D shows the LARA data of the DT-concentration, as well as the used DT-fractions and statistical uncertainty. To estimate the DT-fluctuation on stacked run, the DT-fluctuation is scaled by $\sqrt{N}$, where N is the number of runs [70].

Other systematic uncertainties

The scale of systematic uncertainties considered in this analysis are listed in table 4.2. All B-fields are considered to have an uncertainty of 2 %. The uncertainty on the B-fields result in an uncertainty of the transmission probability, and thus have a stronger effect on measuring points closer to the endpoint. The energy loss parametrisation and correlated uncertainties are taken from Aseev *et al.* and Abdurashitov *et al.* [2, 11]. The FSD onset is describing the ratio between rovibrational ground states and electronic excitation states. It is planned to be refined in the future, and thus conservatively estimated to be 3 % in this work [69]. The uncertainties on the the detection efficiency resulting from pile-up is in the order of $\sim$ 1.0 ‰, whereas the uncertainty on the detection efficiency resulting from a ROI cut is $\sim$ 0.03 %. The uncertainty on $\rho d\sigma$ is composed of an estimated uncertainty of 5 % on the column density ρd and 2 % on the inelastic cross section σ, leading to a total systematic uncertainty of $\sqrt{(5\,\%)^2 + (2\,\%)^2} = 5.39\,\%$.

4.5.3 Treatment of uncertainties

In the following analysis, systematic uncertainties are taken into consideration, using the covariance matrix approach. The covariance matrix approach assumes Gaussian distribution of the data and thus is only valid for high count rates. An advantage of this method is that the systematic effects can be applied separately and are easily combined. Furthermore, the matrices are calculated only once and can then be used for independent datasets, with the same preconditions. It is therefore a flexible and fast method. To calculate a covariance matrix, the respective variable is varied in the range of the uncertainties, generating ~ 1000 Monte Carlo spectra. A covariance matrix V can be calculated, using the following relation.

$$V_{i,j} = \mathrm{cov}(\vec{r}_i, \vec{r}_j) = \frac{1}{N_{\mathrm{spectra}}} \sum_{l=0}^{N_{\mathrm{spectra}}} \left(\vec{r}_{i,l} - \langle \vec{r}_i \rangle\right) \cdot \left(\vec{r}_{j,l} - \langle \vec{r}_j \rangle\right). \tag{4.37}$$

$V_{i,j}$ are the entries of the covariance matrix and the vectors $\vec{r}$ denote the generated Monte Carlo spectra. The covariance matrix is normalised to the total number of spectra N_{spectra}. Introducing covariance matrices adds systematic uncertainties to the spectrum, while keeping correlations between the data points intact. To implement multiple systematic uncertainties, covariance matrices can be calculated independently and be combined by summing over the according matrices V_k,

$$V_{\mathrm{syst}} = \sum_k V_k. \tag{4.38}$$

Bin-to-bin uncorrelated systematic uncertainties are represented by diagonal elements of the covariance matrix. The statistical error is represented by a diagonal matrix V_{stat} with the number of counts N_i on the diagonal entries. This is based on the assumption of a statistical uncertainty of $\sigma_{\mathrm{stat.},i} = \sqrt{N_i}$. Combining the statistical and systematic errors leads to the total covariance matrix V_{tot},

$$V_{\mathrm{tot}} = V_{\mathrm{stat}} + V_{\mathrm{syst}}. \tag{4.39}$$

The total covariance matrix is put into the χ^2-function, and the χ^2 is then minimised

$$\chi^2\left(\vec{m}(\theta), \vec{d}\right) = \left(\vec{m}(\theta) - \vec{d}\right)^{\mathrm{T}} V_{\mathrm{tot}} \left(\vec{m}(\theta) - \vec{d}\right). \tag{4.40}$$

Here $\vec{m}(\theta)$ represents the count rate predicted by the model with fit parameters θ, and $\vec{d}$ denotes the measured data [69].

All calculated covariance matrices are shown in figures 4.7 and 4.8. Combining all uncertainties, leads to the covariance matrix, shown in figure 4.9. Each bin of the covariance matrix is corresponding to a retarding potential set-point of the MTD. In all figures, bin 0 corresponds to the retarding potential 4.0 kV below the endpoint, and bin 21 to a retarding potential 40 eV above the endpoint.

The systematic uncertainties on the detection efficiency were calculated via Gaussian error propagation of equation 4.18 (figure 4.7a) and equation 4.33 (figure 4.7b). Both detector related uncertainties are mainly manifested in diagonal elements of the covariance matrix. As rates further away from the endpoint are higher, the uncertainty related to pile-up is increasing with the retarding energy. The systematic uncertainties on the magnetic fields (B_{ana}, B_{max} and B_{source}) are combined in one covariance matrix (figure 4.7c). Hereby, mainly bins in a 100 eV region below the endpoint are affected, as the influence on the transmission function and thus the KATRIN response function is larger in this region, in

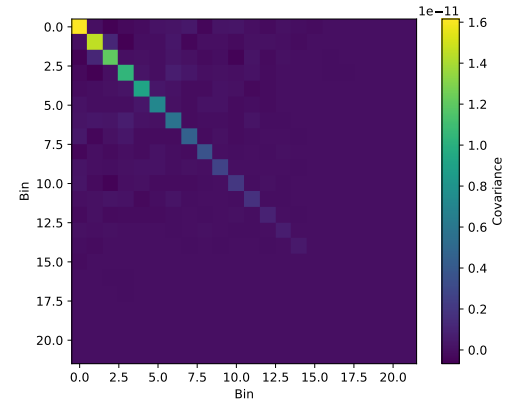

(a) Detection efficiency (pile-up).

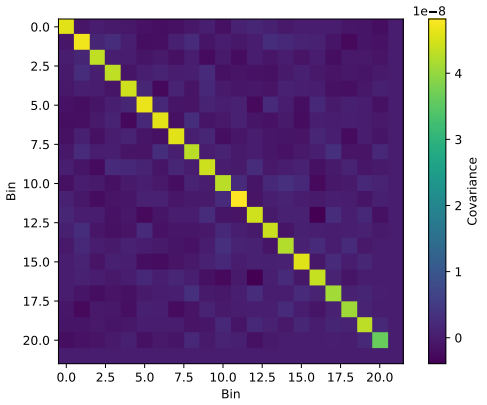

(b) Detection efficiency (ROI-cut).

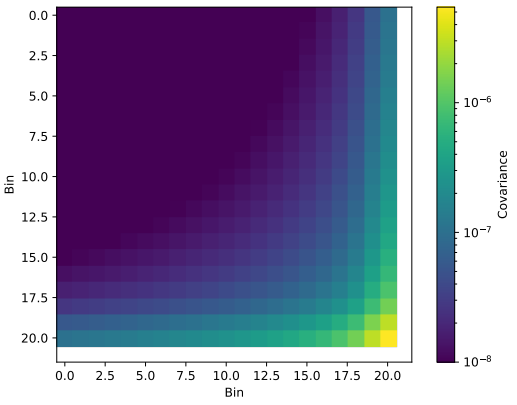

(c) B_{source}, B_{ana} and B_{max}

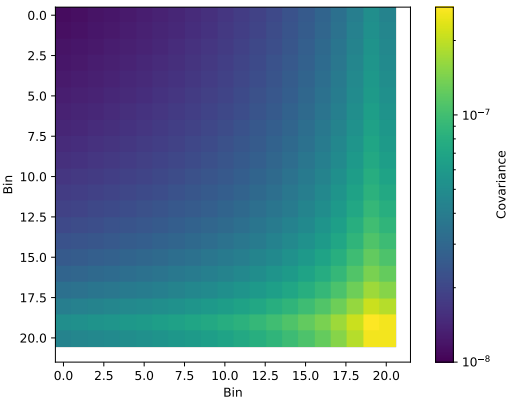

(d) Energy loss.

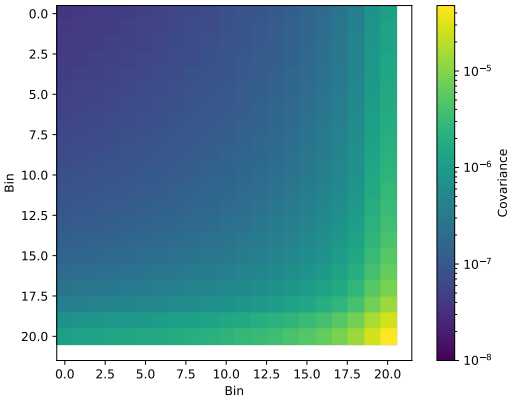

(e) FSD (bin-to-bin correlation).

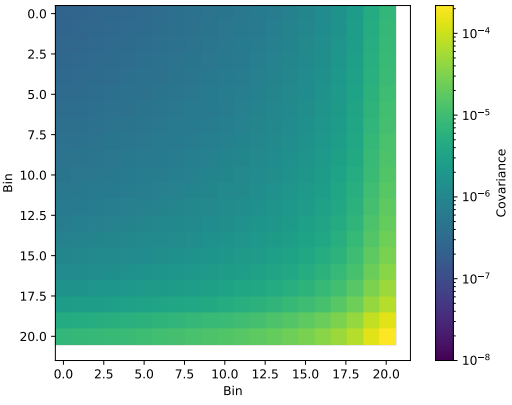

(f) FSD (onset).

Figure 4.7: Calculated covariance matrices used in this analysis. **(a)** Detection efficiency related uncertainty due to pileup. **(b)** Detection efficiency related uncertainty due to the chosen region of interest cut. **(c)** Systematic uncertainties on all magnetic fields combined in a single covariance matrix. **(d)** Systematic uncertainty on the energy loss function. **(e)** Uncertainties on the bin to bin correlation of the rovibrational ground states and the excited states. **(f)** Uncertainty considering an onset on the FSD.

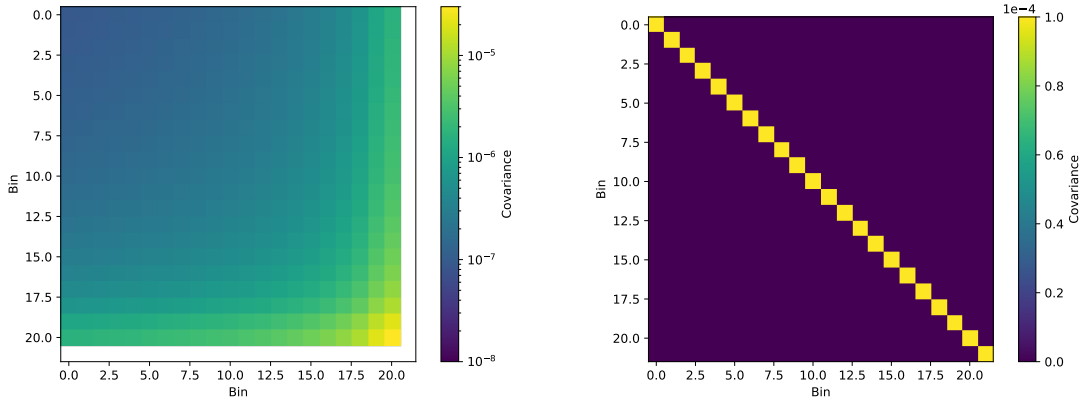

(a) $\rho \mathrm{d}\sigma$. **(b)** DT-fluctuation.

Figure 4.8: Calculated covariance matrices used in this analysis. **(a)** Systematic uncertainty on the column density and the elastic scattering cross section $\rho d\sigma$. **(b)** Example for a uniform systematic uncertainty on the DT stability with 1 %, as bins are uncorrelated, the matrix only contains diagonal elements.

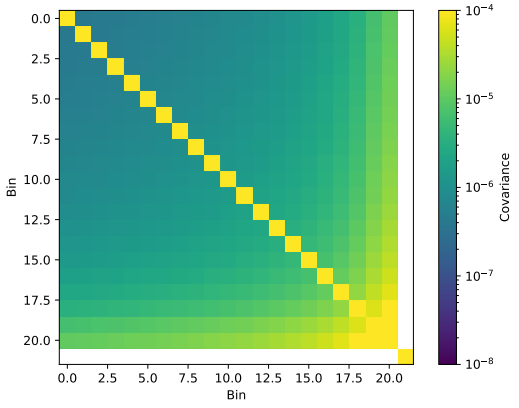

Figure 4.9: Covariance matrix of all systematics combined, including detection efficiency. To accentuate the structure, a logarithmic colour-scale has been used.

comparison to bins deeper in the spectrum. The 4 keV-MTD has only one measurement point in this range, therefore the uncertainty mainly applies to this bin. The energy loss uncertainty affects more bins, as the energy loss, considering 10 scatterings, is in a region around 300 eV below the endpoint (figure 4.7d). The FSD effects of an onset and the correlation between the bins of the FSD result in the covariance matrix, show in figures 4.7e and 4.7f. The uncertainty on the DT-fluctuation is uncorrelated, and thus only possesses diagonal entries (figure 4.8b).

4.6 Results

The model for the integral tritium spectrum $I(qU)$ is parametrised, as described in equation 4.20. In general the model includes seven free parameters, namely the endpoint E_0, the normalisation $Norm$, the background Γ_{Bkg}, the product of column density and cross section $\rho d\sigma$, the squared neutrino mass ν^2, as well as both sterile neutrino parameter, the sterile-active neutrino mass ν_{heavy} and the sterile mixing amplitude $\sin^2(\theta)$.

For the following analysis, only the endpoint, the normalisation, and the background are free fit parameters. Therefore the negative log likelihood for the data d is $(-\ln \mathcal{L}(d|E_0, \Gamma_{\mathrm{Bkg}}, \mathrm{Norm}))$. The squared neutrino mass, as well as both sterile neutrino parameter, the sterile neutrino mass and the mixing amplitude, are fixed to zero inside the model. Both sterile neutrino parameters are fixed to zero, as a proof of concept, and will later be varied to calculate exclusion limits. $\rho d\sigma$ is set to the value, calculated by the throughput in the LOOPs system. The model is initialised, considering a maximum number of 10 scattering inside the source and uses the Doss FSD model [36, 37], as well as an isotropic transmission function for the entire detector.

Figures 4.11 and 4.10 as well as appendix F the fit results of the two dedicated sterile neutrino runs (run 40773 and run 40806), 4 keV below the endpoint, is shown. In this particular case considering only statistical uncertainties. Influences of systematic uncertainties will be discussed in section 4.6.3. In this first analysis, Poissonian likelihood estimation is assumed. Figure 4.11 shows the fit result for a uniform detector, combining the data of all pixels. Each subfigure is divided into two subplots. The upper subplot shows the measured count rates, with a maximum count rate of 72.59 kcps for the bulls eye and the most inner two rings (pixel 0 to 27), as well as the fit of the integral tritium model in blue. The lower subplot gives the residuals normalised by the uncertainty for each data point in comparison to the model. Taking only statistical uncertainties into account. In run 40773 two data points are laying outside the 2σ error band, and in run 40806 three data points are outside the 2σ error band. The 1σ band in this case is given by the statistical uncertainty.

Furthermore, as a consistency check, pixel-wise fits are calculated to check if the fit parameters show any structure. Figure 4.10 the results for the endpoint, normalisation, and the background for a pixel-wise fit of run 40773 is shown, where the count rate of each pixel is fit separately, visualised as a coloured pixel map of the FPD. The pixel-wise fit results of run 40806 are shown in appendix F. The subfigures also give the average value for the fit parameters, averaged over all active pixels. The error reflects the variance of the pixel-wise fit results. The plots show no large observable difference or structure of the fit results. In direct comparison, the fit results are in good agreement, and the pixel-wise fits don’t show obvious features.

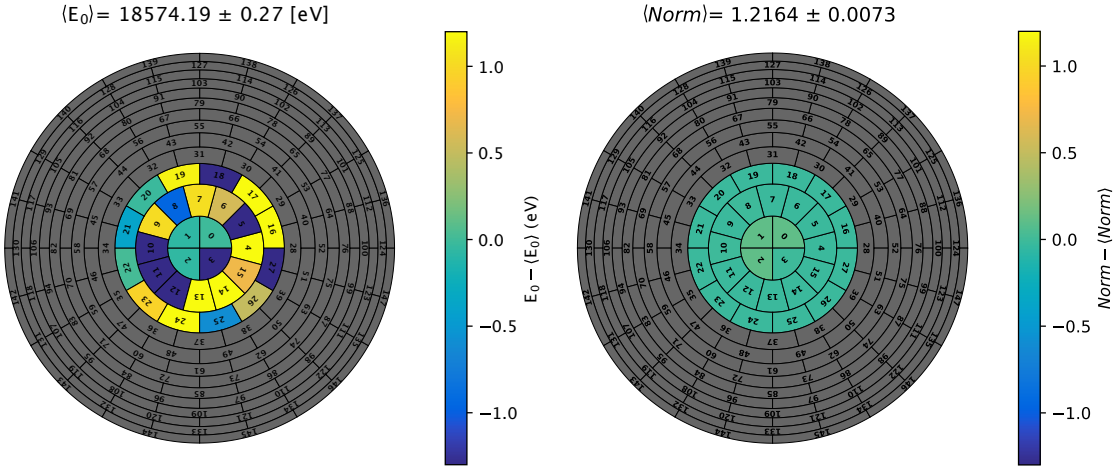

(a) Endpoint.

(b) Normalisation.

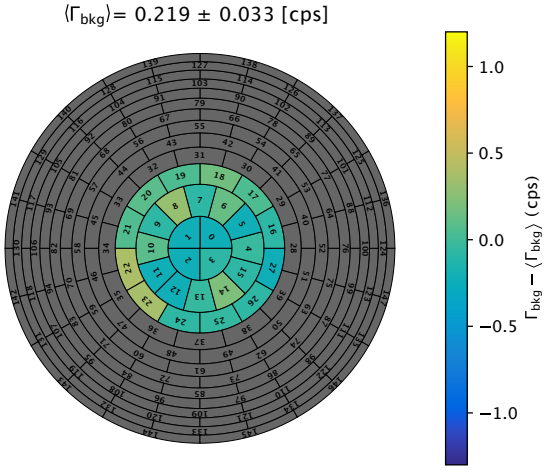

(c) Background.

Figure 4.10: Pixel-wise fit of a FT run (run 40773) with reduced column density, measuring 4.0 keV deep into the spectrum. Each subfigure shows the pixel-wise fit results for **(a)** the endpoint E_0, **(b)** the normalisation, and **(c)** the background Γ_{bkg}. Each figure also gives the mean result of the fitted parameter, as well as the variance of the fit results. Only the endpoint, normalisation and the background are fit. The neutrino mass squared is fixed to zero, as well as the sterile neutrino mass and the mixing amplitude. The pixel map shows no structures for the fit results of each parameter, as well as only small variations of the parameters. The pixel-wise fit for run 40806 can be found in appendix F.

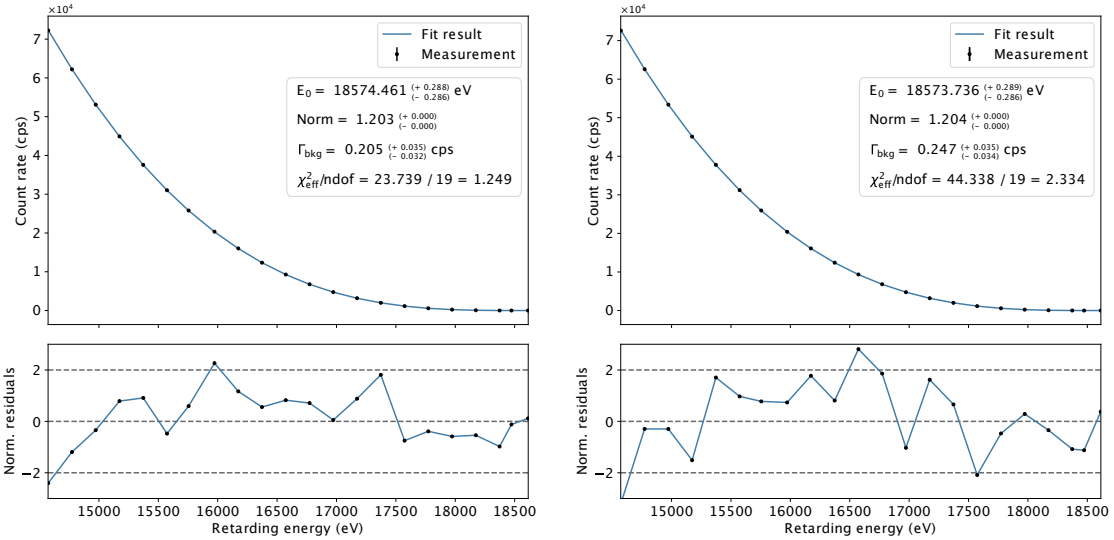

(a) Run 40773. **(b)** Run 40806.

Figure 4.11: Fit of the two 4 keV FT runs (run 40773 and run 40806) with reduced column density, measuring 4.0 keV into the spectrum. The endpoint, normalisation, and the background were fit to a uniform detector model. The neutrino mass squared was fixed to zero, as well as the sterile neutrino mass and the mixing amplitude. The upper subplots show the measured data as well as the fit results for the integrated tritium model. The lower subplots give the residuals, normalised to the statistical uncertainty. Apart from three data points, all normalised residuals are inside the 2σ error band.

4.6.1 Sensitivity of KATRIN based on Monte Carlo

The sensitivity study shown here is based on the settings used during the dedicated sterile neutrino runs during FT. Furthermore the same systematic uncertainties were included as in the final analysis, as well as conservatively estimated values for the DT-fluctuation which is in a comparable regime to the measured systematic uncertainties on the DT-fluctuation. In this case DT-fluctuations were conservatively estimated to be 1 % for a single run. The systematic uncertainties for the DT-fluctuation were scaled by square-root of the number of runs $\sqrt{N}$ [70], thus giving smaller systematic uncertainties for longer measurement times.

To calculate the statistical sensitivity for the datasets, a so called “Asimov” dataset[1] was produced, with no statistical fluctuations and only the expectation value for each variable. In this case, a Monte Carlo dataset with the MTD was used in the 4 keV measurements during FT and a total measurement time of 5700 s = 1 run was generated. Additionally a 11 400 s = 2 runs “Asimov” dataset was generated, for the case of two stacked runs. The parameter space $(\sin^2(\theta), m_{\text{heavy}})$ is scanned in a (20×21) grid pattern, fitting a spectrum for each combination. Subsequently the calculated negative log likelihoods $-\ln \mathcal{L}$, are linearly interpolated for all combinations in between this grid. The sensitivity to a sterile neutrino at a 90 % CL can be calculated as shown in section 4.4.3.

In figure 4.12, the results of the sensitivity study for different effective measurement times is shown. The general shape of all the sensitivity curves shows a minimum at $\nu_{\text{heavy}} \approx 1.2\,\text{keV}$, with decreasing sensitivity towards both sides of the data frame. Regions above the sensitivity curve can be excluded with a 90 % CL. For sterile neutrino masses at the lower end of the energy spectrum, less data points are below the sterile kink, making it less

[1] A Monte Carlo dataset, in which all quantities are set to their expectation value.

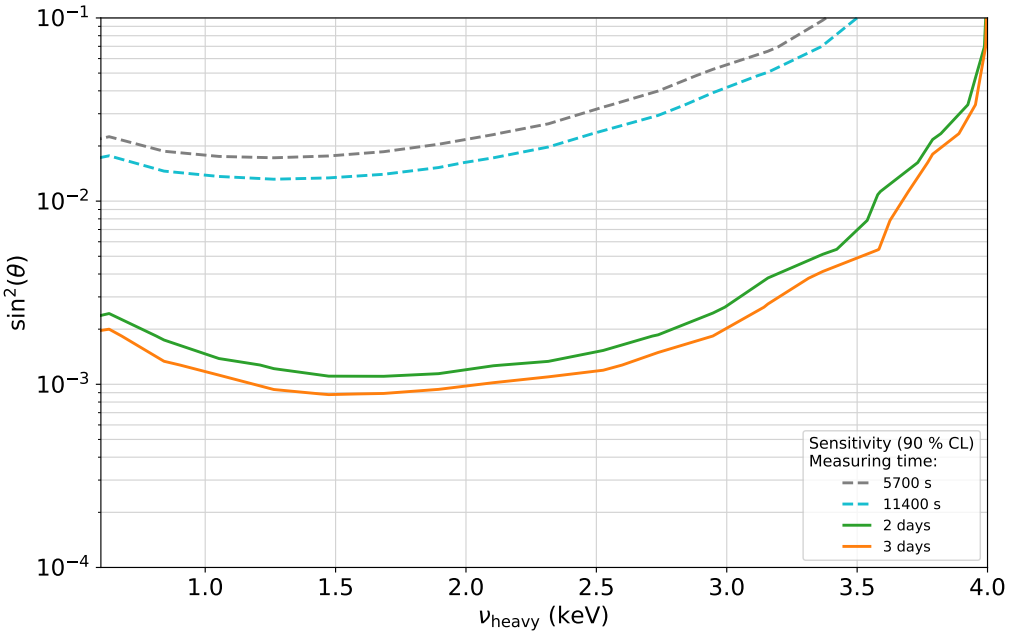

Figure 4.12: Calculated statistical sensitivity (90 % CL) for dataset of a single run, based on the MTD described in section 4.2 (grey), as well as the statistical sensitivity for two stacked runs, equivalent to a 11 400 s dataset (teal). Additionally the sensitivity for 2 days (green), and 3 days (orange) of measurement time are shown, using the same MTD. The sensitivity has been scanned over a (20×21) grid for $(\sin^2(\theta), m_{\text{heavy}})$.

distinguishable. The same reasoning applies for sterile neutrino masses towards the upper end of the data frame, as less data points are in above the sterile kink. The extreme cases are sterile neutrino masses higher than the last data point, as any combination of sterile neutrino mass and mixing angle can be fit to the data.

Furthermore the figure contains the sensitivity for different effective measurement times: 1 run (dashed grey), 2 runs (dashed teal), 2 days (solid green), and 3 days (solid orange). With longer effective measurement time, the sensitivity improves. This can be explained as the relative statistical uncertainty decreases with the effective measurement time, as the over all statistics are higher. Furthermore, as the dominant systematic uncertainty on the DT-fraction is scaled by the square root of the number of runs $\sqrt{N}$, the systematic uncertainty decreases with longer effective measurement times.

For a single 5700 s run the minimum mixing angle that can be distinguished from a spectrum without a sterile neutrino is $\sin^2(\theta)_{\text{min}}(1\,\text{run}) \approx 1.8 \times 10^{-2}$, corresponding to $\nu_{\text{heavy}} \approx 1.3\,\text{keV}$. By doubling the measurement time, the minimum mixing angle decreases to $\sin^2(\theta)_{\text{min}}(2\,\text{runs}) \approx 1.5 \times 10^{-2}$, corresponding to $\nu_{\text{heavy}} \approx 1.3\,\text{keV}$. Increasing the effective measurement time from hours to the order of days, the minimal value for the mixing amplitude that can be distinguished decreases further. In this case to $\sin^2(\theta)_{\text{min}}(2\,\text{d}) \approx 1.1 \times 10^{-3}$ for 2 days of effective measurement time, corresponding to $\nu_{\text{heavy}} \approx 1.7\,\text{keV}$. With 3 days of effective measurement time, the limit decreases further to $\sin^2(\theta)_{\text{min}}(3\,\text{d}) \approx 0.9 \times 10^{-3}$, corresponding to $\nu_{\text{heavy}} \approx 1.7\,\text{keV}$.

4.6.2 Exclusion based on data

The 90 % exclusion limit for measured data can be calculated analogously to the sensitivity. Hereby the parameter space $(\sin^2(\theta), m_{\text{heavy}})$ is scanned as before, in a (20×21) grid-wise

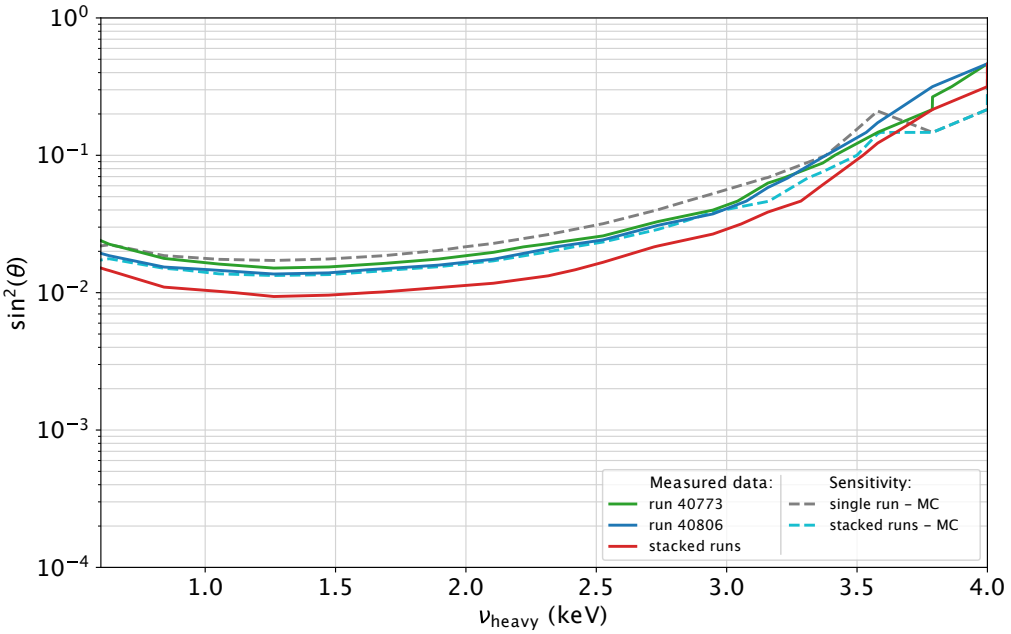

Figure 4.13: Calculated 90 % CL exclusion limit based on data. The exclusion has been scanned over a (20×21) grid for $(\sin^2(\theta), m_{\mathrm{heavy}})$. The plot shows the exclusion limit, based on data measured in run 40773 (solid green) and in run 40806 (solid blue), as well as the exclusion limit calculated when stacking both runs (solid red). In comparison the statistical sensitivity for a single run (dashed grey) and for stacked runs (dashed teal) is also shown, which were described in section 4.6.1.

pattern and later linearly interpolated for all combinations in between. Figure 4.13 shows the results for the 90 % CL exclusion limit, including all systematic uncertainties. The plot shows both 4 keV scans (solid green and solid blue), as well as the result when stacking both runs (solid red). In comparison the statistical sensitivity presented in section 4.6.1 for both single runs (dashed grey), as well as for the stacked runs (dashed teal) is plotted.

The contour of the exclusion lines follows the expected shape, with a minimum in the centre of the measurement window ($\nu_{\mathrm{heavy}} \approx 1.3\,\mathrm{keV}$), and declining sensitivity to both sides. The 90 % CL exclusion line for run 40773 has a minimum at $\sin^2(\theta) \approx 1.48 \times 10^{-2}$, and run 40806 at $\sin^2(\theta) \approx 1.34 \times 10^{-2}$. In comparison to the statistical sensitivity, the exclusion limits of runs 40773 and 40806 are lower than the sensitivity curve for a single run. This can be explained due to statistical fluctuations of the measured data, or as the DT-fluctuations were estimated too conservatively in the Monte Carlo study.

As a direct consequence of the statistical fluctuations of both single runs, stacking leads to an exclusion limit which is also lower than the statistical sensitivity. This leads to an exclusion limit with a minimum at $\sin^2(\theta) \approx 0.93 \times 10^{-3}$ for $\nu_{\mathrm{heavy}} \approx 1.3\,\mathrm{keV}$.

The sensitivity and the exclusion limit are in agreement. As only two measurements were taken to down 4 keV below the endpoint, as expected the exclusion limit is still relatively high. Thus these measurements give a first hint, on what can be expected from future measurements and which challenges are relevant in future analysis. Therefore in the next section, the effects of systematic uncertainties will be discussed in more detail.

4.6.3 Influence of systematics

The predominant systematic uncertainty is given by the DT-fluctuations for single runs, as they contribute mainly to the systematic uncertainty for all bins. The systematic

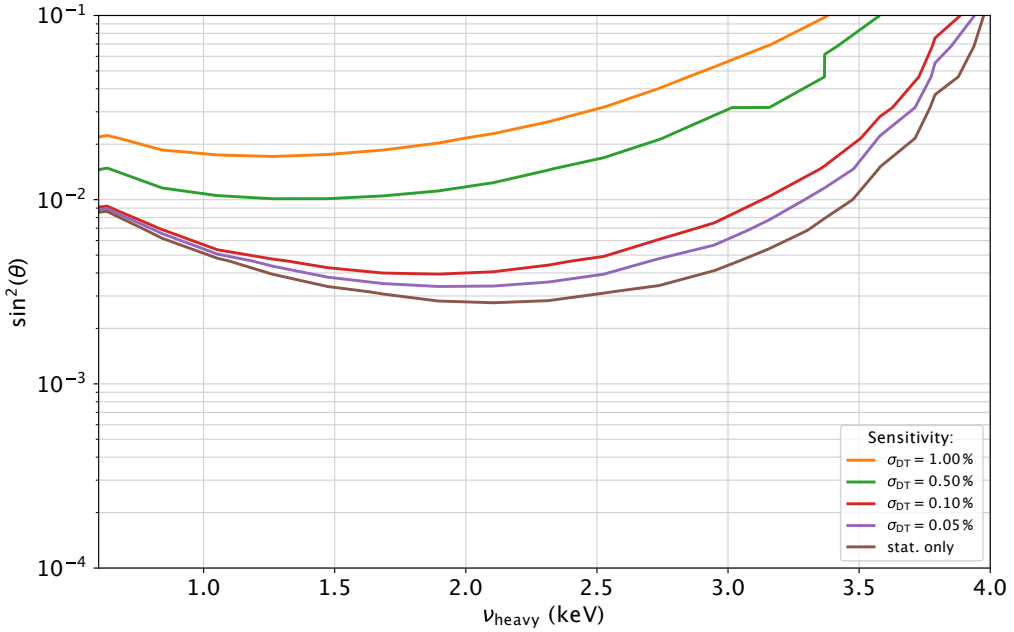

Figure 4.14: Influence of systematic uncertainties on the sensitivity. The sensitivity of a single run to the sterile neutrino parameters is shown, assuming four different systematic uncertainties on the DT-concentration. The uncertainties are: 0.05 % (purple), 0.1 % (red), 0.5 % (green), and 1.0 % (orange). For comparison the sensitivity, assuming only statistical uncertainties is shown (brown).

uncertainty on the DT-concentration for a single run is estimated to be 1 %. By stacking more runs, the systematic uncertainty on DT can be reduced, as the uncertainty is scaled by the square root of the number of runs $\sqrt{N}$.

In figure 4.14 a Monte Carlo study is shown, assuming four different systematic uncertainties on the DT-fraction. The study is based on the Monte Carlo dataset for a single run, which was also used in the previous sections. The uncertainties on the DT-concentration are: 0.05 % , 0.10 %, 0.50 %, and 1.00 % . Furthermore the plot includes the sensitivity curve assuming only statistical uncertainties. It is demonstrated that the uncertainty on the DT-concentration has a dominant impact on the sensitivity to the sterile neutrino parameters. By decreasing the systematic uncertainty from 1.0 % (orange) to 0.1 % (red), the sensitivity can be improved in the minimum by a factor of up to approximately five.

Furthermore the sensitivity study shows that the minimum of the sensitivity curves are shifted to lower sterile neutrino masses with increasing systematic uncertainties. Assuming an uncertainty of 1.0 % results in a minimum at $\nu_{\text{heavy}} \approx 1.3\,\text{keV}$. In comparison, a smaller systematic uncertainty on the DT-concentration of 0.05 % gives a minimum of the sensitivity curve at $\nu_{\text{heavy}} \approx 1.9\,\text{keV}$.

The 1.0 % uncertainty on the DT-concentration that is used in this analysis is a rather conservative estimation. A decrease of the systematic uncertainties to ~ 0.1 % would be desirable as the sensitivity would reach a regime which is comparable to the statistical sensitivity.

4.7 Outlook

These first measurements give an insight deeper into the tritium spectrum. The analysis has shown, that with dedicated sterile neutrino runs in the order of keV, a first exclusion

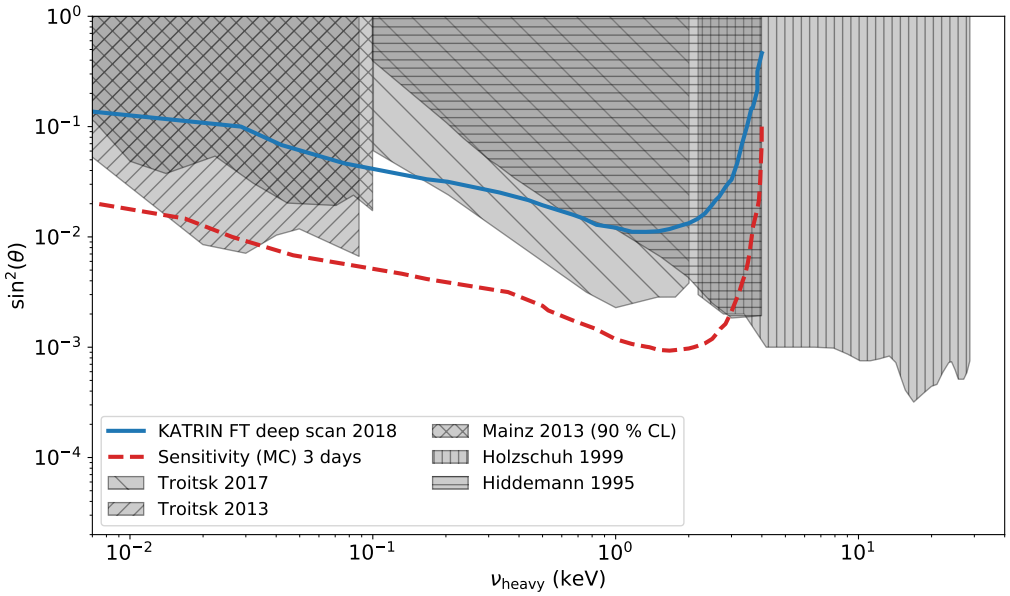

Figure 4.15: Comparison of the calculated 95 % CL exclusion limit calculated from the measured data (solid blue) to the results of other experiments. The plot contains the 95 % CL exclusion limits on the sterile neutrino parameters, given by Troitsk 2017 [3] and Troitsk 2013 [49]. Furthermore the 90 % CL given by the Mainz experiment [77], as well as the 95 % CL given by Holzschuhe *et al.* [62], based on β-spectrum measurements of Ni-63, and Hiddemann *et al.* [60], based on β-spectrum measurements of tritium, are shown. Additionally the sensitivity for 3 days of effective measurement time, based on a sensitivity study is shown (dashed red).

limit can be given (solid blue) comparable to other dedicated experiments. In figure 4.15 the 95 % CL calculated exclusion limit is shown in comparison to the exclusion limit given by other studies and experiments. The plot includes results by the Troitsk neutrino mass experiment [3, 49], and the Mainz experiment [77]. Furthermore results by Holzschuhe *et al.* [62] from β-spectrum measurements of Ni-63, and Hiddemann *et al.* [60] from β-spectrum measurements of tritium are shown. Additionally the sensitivity for 3 days of effective measurement time, based on a sensitivity study is shown in the plot (dashed red). With the measured data the limit is already comparable to other experiments, which reflects the high potential of dedicated sterile neutrino measurements with the current setup. With further dedicated sterile neutrino measurements using the present setup, it would already be possible to improve the exclusion limit further by an order of magnitude.

The treatment of systematic uncertainties especially the DT-fluctuations is a key factor in future analysis. An improvement of the uncertainties would be beneficial, subsequently improving the sensitivity. The rate stability measured by the FBM could, for example, be used as an indicator for DT-fluctuations and could reduce the systematic uncertainty. Characterisation measurements also continue to improve the model used in KATRIN, giving a better representation of the measured data, leading to an improved sensitivity.

This chapter also highlights the importance and potential of the TRISTAN project. With the new TRISTAN detector system it is possible to use the full source strength and thus obtain high statistics. Furthermore it will be possible to measure even deeper into the tritium spectrum.

5. Convolutional model for KATRIN - SSC-sterile

The search for keV-scale sterile neutrinos in β-decay spectra requires a highly precise underlying model for a wide energy range. In future measurements with the TRISTAN detector, the energy spectrum will be measured further into the tritium spectrum compared to the standard KATRIN neutrino measurements. A new model is currently being developed, which includes systematics that take effect not only in the endpoint region, but in lower energy ranges of the spectrum. The C++ code to generate this customised sterile neutrino model is mainly developed by A. Lokhov (INRM) and M. Slezák. (MPP) SSC-sterile is based on a convolutional approach. Effects directly influencing the spectrum are separately simulated or calculated, and can then be subsequently folded into the spectrum. The advantage of the SSC-model is, that every effect going into the model can be studied and treated separately. The following sections will explain the convolutional approach and will go into further detail on the detector response used within the model.

5.1 SSC-sterile model

The initial simulated spectrum is given by the theoretical tritium spectrum, with an isotropic angular distribution of the electron momenta. Inside the model, electrons are binned over their energies E_m and their pitch angle $\cos(\theta_n)$. Electrons in the same angular bins, can be combined to a vector S^T, containing the spectral entries $(S_1, S_2, \ldots, S_N)$ of all energy bins. The spectral distribution is given by the theoretical β-decay spectrum. By convoluting the initial electron spectrum with the combined response matrix R_{tot}, the final distribution M^T of the measured differential spectrum can be calculated. The response matrix represents the energy and angular redistribution of the electrons, given by the experiment. The approach can be written as:

$$M^T = S^T \times R_{\text{tot}} = S^T \times R_1 \times R_2 \times \ldots . \tag{5.1}$$

The complete response can be calculated by convolving response matrices R_i for various effects. Thus these matrices can be calculated individually. Each matrix is redistributing electrons from a single angular and energy bin onto a new set of angular and energy bins. Redistribution of each bin is realised by convolution with a two dimensional matrix. As there are n angular bins and m energy bins, there is a total number of $(n \cdot m)$ two dimensional matrices. Internally, the matrices are handled as four dimensional matrices, that can be applied to four dimensional vectors. An illustration of the four dimensional matrix can be seen in figure 5.1.

Matrices are scaled to the initial number of electrons. Furthermore, matrices are not necessarily unitary, reflecting the complex effects of electron losses. As the detector is only capable of measuring the energy of electrons, the final vector of measured electrons contains

$$
\begin{array}{c|cccc}
 & E_1 & E_2 & \dots & E_m \\
\cos(\theta_1) & \begin{pmatrix} R_{1111} & R_{1112} & \dots & R_{111j} \\ R_{1121} & R_{1122} & \dots & R_{112j} \\ \vdots & \vdots & \ddots & \vdots \\ R_{11i1} & R_{11i2} & \dots & R_{11ij} \end{pmatrix} & \begin{pmatrix} R_{1211} & R_{1212} & \dots & R_{121j} \\ R_{1221} & R_{1222} & \dots & R_{122j} \\ \vdots & \vdots & \ddots & \vdots \\ R_{12i1} & R_{12i2} & \dots & R_{12ij} \end{pmatrix} & \dots & \begin{pmatrix} R_{1m11} & R_{1m12} & \dots & R_{1m1j} \\ R_{1m21} & R_{1m22} & \dots & R_{1m2j} \\ \vdots & \vdots & \ddots & \vdots \\ R_{1mi1} & R_{1mi2} & \dots & R_{1mij} \end{pmatrix} \\
\cos(\theta_2) & \begin{pmatrix} R_{2111} & R_{2112} & \dots & R_{211j} \\ R_{2121} & R_{2122} & \dots & R_{212j} \\ \vdots & \vdots & \ddots & \vdots \\ R_{21i1} & R_{21i2} & \dots & R_{21ij} \end{pmatrix} & \begin{pmatrix} R_{2211} & R_{2212} & \dots & R_{221j} \\ R_{2221} & R_{2222} & \dots & R_{222j} \\ \vdots & \vdots & \ddots & \vdots \\ R_{22i1} & R_{22i2} & \dots & R_{22ij} \end{pmatrix} & \dots & \begin{pmatrix} R_{2m11} & R_{2m12} & \dots & R_{2m1j} \\ R_{2m21} & R_{2m22} & \dots & R_{2m2j} \\ \vdots & \vdots & \ddots & \vdots \\ R_{2mi1} & R_{2mi2} & \dots & R_{2mij} \end{pmatrix} \\
\vdots & \vdots & \vdots & \ddots & \vdots \\
\cos(\theta_n) & \begin{pmatrix} R_{n111} & R_{n112} & \dots & R_{n11j} \\ R_{n121} & R_{n122} & \dots & R_{n12j} \\ \vdots & \vdots & \ddots & \vdots \\ R_{n1i1} & R_{n1i2} & \dots & R_{n1ij} \end{pmatrix} & \begin{pmatrix} R_{n211} & R_{n212} & \dots & R_{n21j} \\ R_{n221} & R_{n222} & \dots & R_{n22j} \\ \vdots & \vdots & \ddots & \vdots \\ R_{n2i1} & R_{n2i2} & \dots & R_{n2ij} \end{pmatrix} & \dots & \begin{pmatrix} R_{nm11} & R_{nm12} & \dots & R_{nm1j} \\ R_{nm21} & R_{nm22} & \dots & R_{nm2j} \\ \vdots & \vdots & \ddots & \vdots \\ R_{nmi1} & R_{nmi2} & \dots & R_{nmij} \end{pmatrix}
\end{array}
$$

Figure 5.1: Illustration of the four dimensional $(n \times m \times i \times j)$ response matrix, applied to the initial spectrum. Rows of the matrix are related to the angular bins $(\cos(\theta_1), \cos(\theta_2), \dots, \cos(\theta_m))$, columns represent the according energy bin $(E_1, E_2, \dots, E_m)$ of the initial spectrum. The $(i \times j)$ sub-matrices correspond to the i^{th} final angular bins and the j^{th} final energy bins. The indices of all entries are in the order of: initial angular bin, initial energy bin, final angular bin, final energy bin.

the measured energy spectrum with no information about the pitch angle. Currently the model consists of five major components: The theoretical tritium decay model, scattering at the rear wall, scattering inside the source, the spectrometer response, and the response given by the silicon detector.

The source end of the KATRIN experiment contains a gold coated rear wall. For electrons with high surplus energies, it is possible that electrons hitting the rear wall are scattered back into the source, and still have enough energy to overcome the retarding potential. Measuring these electrons causes distortions in the final energy spectrum. During first tritium the rear wall was not yet present, thus electrons were hitting a steel valve instead. The according responses for electrons being backscattered from the gold rear wall or the steel valve are based on GEANT4 simulations [47]. In the simulations electrons were generated above a gold or steel surface. The response matrices were then generated by binning the backscattered electrons over the energy and pitch angle.

An effect that becomes more prominent when looking deeper into the spectrum is also scattering inside the source. Usually, for the neutrino mass measurements up to 10 scatterings are taken into consideration. For electrons with high energies, more scatterings have to be accounted for. The response of the WGTS is calculated with a convolutional code by M. Slezák. The approach uses an energy dependent cross section and takes many scatterings into account. In the source, electrons are isotropically generated. The code subdivides the WGTS into slices, propagating the energy and angular distribution into neighbouring slices. The final result gives information about the energy and angular distribution, representing the WGTS response.

As the spectrometer is following the MAC-E filter principles, the spectrometer response is given by the condition that electrons with low energies are back reflected by the retarding potential, and electrons with high pitch angles are back reflected by the pinch magnet.

The fifth component is the detector response. The response for electrons reaching the detector was simulated with KESS (KATRIN electron scattering in silicon) [99], a customised tool, to simulate interactions of low energy electrons within silicon. The following sections will describe the conditions used in the Monte Carlo simulation, and the construction of the detector response from this simulated data in detail. Currently a model for the KATRIN detector and the TRISTAN detector prototype are included in SSC-sterile. The KATRIN detector response was calculated for electrons with an initial energy from 16.575 keV to 18.575 keV. The TRISTAN detector response is included for electrons from 13.500 keV to 18.575 keV. The here shown simulation setups are based on the example of the KATRIN detector.

5.2 Detector response

The KESS framework combines various physical models, recreating the impingement of charged particles onto a silicon body. The framework includes scattering of electrons inside the silicon via elastic and inelastic scattering. Furthermore secondary electron production is implemented. Secondary electrons can originate from ionisation such as knock-on electrons[1], and from emission of Auger electrons from atoms. Transition and reflection probabilities when hitting the surface, and surface escape processes from electrons inside the silicon body are also implemented. A more detailed description of the KESS framework, as well as all implemented effects can be found in [99].

Figure 5.2 shows an example for the spectral shape for mono-energetic ($E_{\text{simulated}} = 26\,\text{keV}$) and mono-angular ($\theta = 0°$) electrons, simulated with KESS. The energy is simulated with 10 keV higher than expected from a tritium decay, as a post acceleration of $V_{\text{PAE}} = 10\,\text{kV}$ is assumed. The contribution of different effects to the over all spectral shape, such as the low energetic backscattering tail, energy losses inside the dead layer, and the contribution of electrons that are not backscattered, are illustrated.

To generate the response matrices, a total number of 10^6 electrons were simulated. Again, a post acceleration voltage of $V_{\text{PAE}} = 10\,\text{kV}$ was assumed, thus electrons are initialised uniformly distributed over $E_{\text{simulated}} = [26.575\,\text{keV}, 28.575\,\text{keV}]$. This corresponds to the initial range of the tritium spectrum: $E_{\text{initial}} = [16.575\,\text{keV}, 18.575\,\text{keV}]$. Furthermore the directions of all electron momenta are uniformly distributed over $\cos(\theta) = [0, 1]$. Binning the initial electron distribution into a $(E_{\text{initial}} \times \cos(\theta)) = (10 \times 10)$ bins, results in 10^4 electrons per energy and angular bin. Electrons were initialised in front of the silicon body. The simulated silicon body has a total thickness of 5 mm and a dead layer thickness of 100 nm. In its final form, SSC-sterile contains matrices for a (10×20) binning with $\cos(\theta) = [-1, 1]$. As electrons with $\cos(\theta) = [-1, 0]$ are reflected away from the detector, it is not necessary to simulate these electrons, thus the response matrices for these electrons can be filled with values of zero. After simulating each bin, the histogram is folded with a Gaussian, emulating smearing effects given by the energy resolution of the detector. For the Gaussian smearing, a FWHM of 3 keV is used. Additionally a detection threshold is applied to the energy spectrum, with a value of 5 keV. The detector response is finally binned into 100 energy bins for $E_{\text{final}} = [0.0\,\text{keV}, 32.5\,\text{keV}]$ for each initial energy and angular bin.

Figure 5.3 shows an illustration of the response matrix for the same angular bin ($\cos(\theta) = [0.9, 1.0]$). the left subplot gives the initial electron spectrum, whereas in the right subplot the detector response is given. The final detector response is scaled by the initial number of electrons per initial energy and angular bin. The figure shows the expected behaviour, where the peak position is increasing with the initial energy.

[1] Secondary electrons produced in an inner atom shells, causing further ionisation.

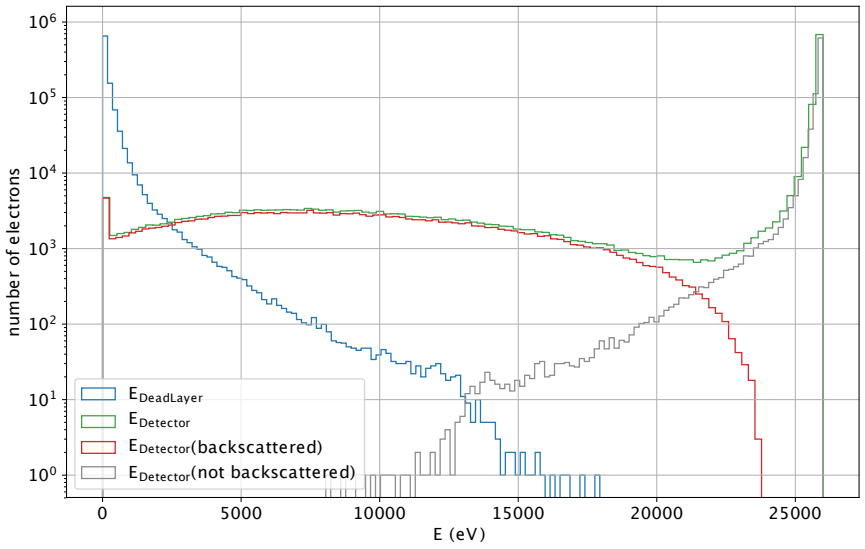

Figure 5.2: Example spectrum for 10^6 mono-energetic ($E_{\text{initial}} = 26\,\text{keV}$) and mono-angular ($\theta = 0°$) electrons simulated with KESS. The example assumes a post acceleration voltage of 10 kV. The plot contains five histogram of different components: The energy histogram of electrons depositing their energy inside the dead layer is shown in blue (here a 100 nm dead layer was assumed). The energy histogram of electrons depositing their energy inside the fiducial material is coloured in green. This is equivalent to a detector with no dead layer. Electrons which are the backscattered, result in the characteristic backscattering tail, which is represented by the red histogram. As well as the energy histogram of electrons that are not backscattered, marked in grey. This resulting in higher energy deposition inside the detector.

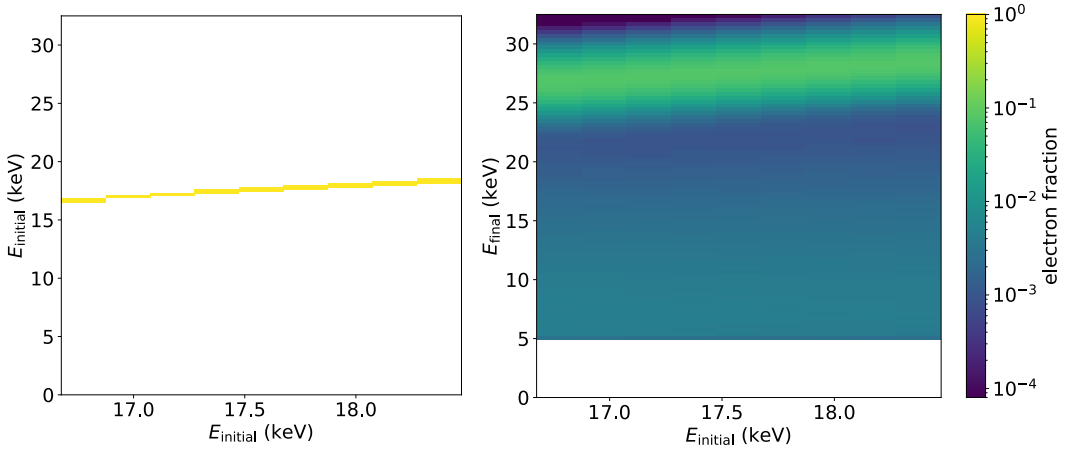

(a) Initial energy distribution. **(b)** Final energy distribution.

Figure 5.3: Illustration of the detector response for all energy bins with $\cos(\theta) = [0.9, 1.0]$. **(a)** Initial energy distribution of electrons, before post regulation. **(b)** Final energy distribution of electrons. Each column of the plot is equivalent to the response matrix for a single energy and angular bin. The lower limit is given by the detector threshold.

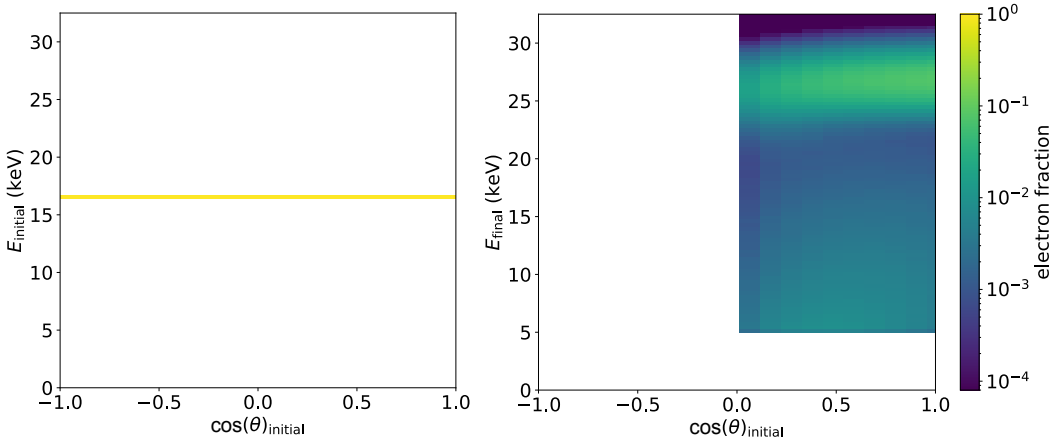

(a) Initial energy distribution. **(b)** Final energy distribution.

Figure 5.4: Illustration of a KATRIN detector response for angular bins within $E_{\text{initial}} = [16.575\,\text{keV}, 16.775\,\text{keV}]$. **(a)** Initial energy distribution of the electrons, before post regulation. **(b)** Final energy distribution of the measured electrons. As only electrons with $\cos(\theta) = [0, 1]$ are propagating in the direction of the detector, the left side ($\cos(\theta) = [-1, 0]$) contains values of zero. Due to 10 kV post acceleration, the final peak position 10 keV higher than the initial energy.

Figure 5.4 shows an example for the energy response dependent on the initial pitch angle. The angular dependent detector response shown in this figure is given for $E_{\text{initial}} = [18.375\,\text{keV}, 18.575\,\text{keV}]$. The plot also shows, that the peak height for electrons with $\cos(\theta) \sim 0$ is lower. This is due to the fact that electrons with a small impact angle are more likely to be back reflected, thus depositing less energy inside the fiducial volume.

5.3 Backscattering response

Electrons that are backscattered from the detector move along the magnetic field lines and are back reflected at the pinch magnet. These returning electrons can then again be detected by the detector, contributing to the measured energy spectrum. In combination with the back reflection response matrix for the pinch magnet, a backscattering response could be used iteratively to emulate electrons being backscattered and back reflected onto the detector. Following the same simulation principle, response matrices for backscattered electrons can also be calculated. In this case, only electrons leaving the silicon body are taken into consideration. The backscattering response for each energy and angular bin is described as a (100×100) matrix. The matrix entries have been normalised to the total number of electrons started in front of the detector. In this case 10^4 electrons per bin.

An example for the spectrum of backscattered electron is shown in figure 5.5. Here the response matrix for electrons within a single energy and angular bin is plotted ($E_{\text{initial}} = [26.797\,\text{keV}, 26.575\,\text{keV}]$, $\cos(\theta) = [0.0, -0.1]$). As backscattered electrons only possess momentum in opposite direction to the detector, the angular distribution is bound by $\cos(\theta) \leq 0.0$. The upper energy bound of backscattered electrons is given by the upper energy limit of the according bin. In this particular case this is at an energy of 26.575 keV.

5.4 Outlook

The SSC-sterile code provides flexibility and is easily expandable, thus represents a promising concept for simulation deep into the tritium spectrum. On the detector side further response

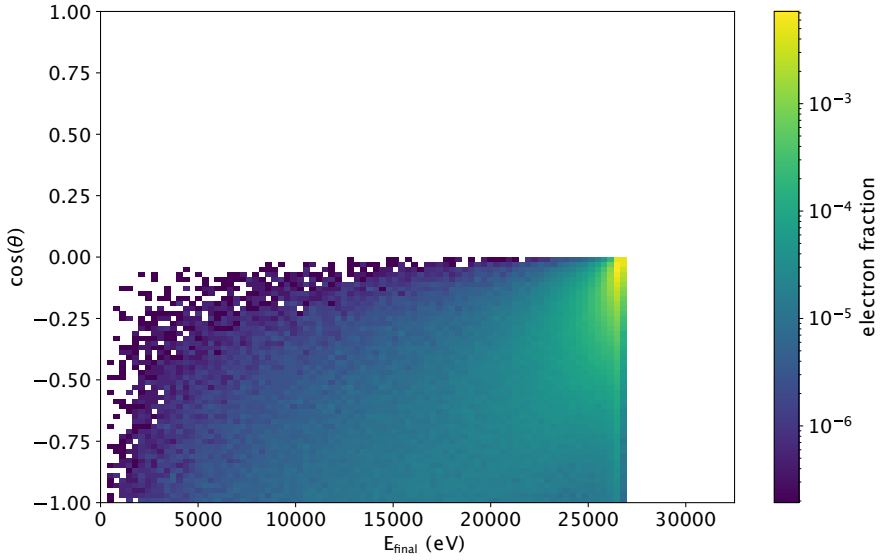

Figure 5.5: Example of a backscattering response for the KATRIN detector, included in SSC-sterile. The plot shows the energy and angular distribution of backscattered electrons. The (100×100) matrix has been normalised to the total number of electrons in the initial bin. In this particular case, the backscattering response for ($E_{\text{simulated}} = [26.797\,\text{keV}, 26.575\,\text{keV}]$, $\cos(\theta) = [0.0, -0.1]$) is shown.

matrices could be added in the future. These matrices could take additional effects into account such as pile-up or charge sharing between pixels.

The method to simulate and calculate a response matrix for all bins in series is still relatively time consuming and could be optimised by parallelising the simulation and calculation processes for each bin. Code to calculate the detector response on the fly could then be integrated, simulating and calculating the detector response matrix, depending on the required energy range and binning.

In combination with future TRISTAN measurements, SSC-sterile is highly promising, as the final energy spectrum can be fit to the actual spectrum measured by the detector. Scattering processes deeper in the spectrum are also considered for high surplus energies, making it possible to perform measurements with the full KATRIN source strength, enabling high statistics runs in future measurements. Various responses of the SSC-sterile model are already successfully used in analysis of keV-sterile measurements with the TRISTAN prototype at the Troitsk neutrino mass experiment [24].

6. Conclusion and outlook

The KATRIN experiment is designed to determine the effective neutrino mass with a sensitivity of 200 meV at a 90 % CL by kinematic measurements of the endpoint region of the tritium β-decay spectrum. With its highly active and stable source, with 10^{11} decays/s, it is possible to precisely measure the spectral shape, not only in the endpoint region, but also further into the spectrum. Therefore it is possible to extend the physics reach of the KATRIN experiment and search for keV-scale sterile neutrinos. When measuring deeper into the tritium spectrum, much higher count rates compared to standard neutrino mass measurements close to the endpoint are expected. To be able to cover the entire energy range, a new detector and readout system is needed. The KATRIN collaboration is currently developing and testing the new TRISTAN detector system, capable of measuring deeper into the tritium spectrum, while making use of the full source strength. To get a first insight deeper into the tritium spectrum, the KATRIN experiment can be used as designed for standard neutrino mass measurements with reduced source strength. This work mainly focuses on the search for keV-scale sterile neutrinos with the current configuration.

Sterile neutrinos in the keV-range are a well motivated extension of the standard model, and could be a viable candidate for dark matter. Extending the β-decay model, a sterile neutrino would be manifested as a kink signature in the spectrum at the location of the sterile neutrino mass.

Within the "first tritium" campaign in June 2018, the KATRIN experiment was successfully tested and operated with 1 % DT inside the system for the first time. During the campaign, first measurements of the tritium spectrum were taken. Furthermore dedicated sterile neutrino measurements down to 4 keV below the endpoint, with reduced column density, were performed. The limiting value of 4 keV is given by the readout capabilities of the DAQ system and the detector system.

The quality of the measured data and the data selection was discussed in this thesis. The importance of pixel dependent detection efficiencies in the final analysis was shown and subsequently implemented in the analysis. The analysis was performed with Fitrium, a custom analysis tool, developed to fit the tritium model to measured data. Furthermore sensitivity studies were presented, while considering systematic uncertainties.

Analysis of the data, including all relevant systematic uncertainties, leads to an exclusion limit on the sterile neutrino parameter space. Based on the data taken during the "first tritium" campaign, sterile neutrinos with mixing-angles down to $\sin^2(\theta) > 1.4 \times 10^{-2}$ (single runs) and $\sin^2(\theta) > 0.9 \times 10^{-2}$ (stacked runs) can be excluded with a 90 % CL. This work showed, that with only ~ 3 h of measurement time and without any hardware modifications the KATRIN experiment is able to achieve sensitivity on the sterile neutrino parameter space, that is comparable to other dedicated experiments. Furthermore it was shown that by increasing the measurement time to days, the sensitivity can be increased

by one order of magnitude, setting new exclusion limits on the sterile neutrino parameter space accessible by tritium β-decay experiments.

It was also shown that the sensitivity can be improved by a factor of approximately ten, when extending the effective measurement time to the order of days, because this results in lower relative statistic and systematic uncertainties. The main uncertainty identified is the uncertainty on the DT-concentration given by LARA. Additionally, this work showed that the magnitude of systematic uncertainties significantly changes the sensitivity. Therefore it is necessary to investigate the DT-fluctuation in further detail beyond this work. Including the stability of the FBM rate as an indicator for the DT-stability could lead to smaller systematic uncertainties for sub runs. Furthermore the uncertainties on the DT-fraction could be reduced by modifying the MTD.

The SSC-sterile model was developed to describe the tritium spectrum measured in the KATRIN experiment based on a convolutional approach. Components and effects can be calculated separately, and combined by folding the response matrices for each effect. In this work the corresponding response matrix for the detector were presented, as well as a response matrix for backscattered electrons.

Concluding, this work presented a first insight on keV-scale sterile neutrino measurements in the future of KATRIN. It was shown that the KATRIN experiment is able to take measurements over a larger energy range from the endpoint under stable conditions. It was demonstrated, that additional measurements with the current detector system would already improve the exclusion limit, and contribute to understanding the challenges for future measurements with the TRISTAN detector system. This sterile neutrino search is a model independent laboratory experiment, and a limit on the sterile neutrino parameters would have a significant impact in particle and astrophysics.

Appendix

A Overview of "first tritium" scans with reduced column density

Table A.1: Summary of the scans performed with reduced column density during "first tritium". The table contains information about the measurement type, the column density, the minimal retarding potential, and the total measurement time, as well as a link to the corresponding E-log entry. Runs with the description "m_ν scan", use the standard MTD used in the neutrino mass measurements. For measurements with the description "extended m_ν scan", the MTD was extended by 1 min sub-runs at 16.775, 16.575, 16.375, 16.175, and 15 975 kV. "Sterile scans" use the MTD, shown in figure 4.1. The runs analysed in this thesis are highlighted in grey.

Run	Measurement	Column density (%)	Column density (10^{21} m^{-2})	Minimum U_{ret} (kV)	Total duration (s)	E-log entry
40761	m_ν scan	50	2.14	1.60	3600	60
40762	m_ν scan	50	2.14	1.60	3600	60
40763	m_ν scan	50	2.14	1.60	3600	60
40764	m_ν scan	50	2.14	1.60	3600	60
40765	m_ν scan	50	2.14	1.60	3600	60
40766	m_ν scan	50	2.14	1.60	3600	60
40769	extended m_ν scan	25	1.09	2.60	3900	61
40770	extended m_ν scan	25	1.09	2.60	3900	61
40773	sterile scan	25	1.09	4.00	5700	62
40794	m_ν scan	25	1.09	1.60	3600	63
40795	m_ν scan	25	1.09	1.60	3600	63
40796	m_ν scan	25	1.09	1.60	3600	63
40797	m_ν scan	25	1.09	1.60	3600	63
40798	m_ν scan	25	1.09	1.60	3600	63
40799	m_ν scan	25	1.09	1.60	3600	63
40800	m_ν scan	25	1.09	1.60	3600	63
40801	m_ν scan	25	1.09	1.60	3600	63
40802	m_ν scan	25	1.09	1.60	3600	63
40803	m_ν scan	25	1.09	1.60	3600	63
40804	m_ν scan	25	1.09	1.60	3600	63
40806	sterile scan	25	1.09	4.00	5700	64

B MTD for sterile neutrino search in “first tritium”

The following table shows the MTD, used in the 4.0 keV deep scans during FT. Due to a lower count rate and thus smaller statistics, the measurement time in the endpoint region is longer.

Table B.2: MTD for the 4.0 keV sterile neutrino runs during FT.

Retarding potential (V)	**Measuring time fraction**	**Measuring time (s)**
40	0.157895	900
-100	0.157895	900
-200	0.157895	900
-400	0.157895	900
-600	0.105263	300
-800	0.052632	300
-1000	0.052632	300
-1200	0.010526	60
-1400	0.010526	60
-1600	0.010526	60
-1800	0.010526	60
-2000	0.010526	60
-2200	0.010526	60
-2400	0.010526	60
-2600	0.010526	60
-2800	0.010526	60
-3000	0.010526	60
-3200	0.010526	60
-3400	0.010526	60
-3600	0.010526	60
-3800	0.010526	60
-4000	0.010526	60

C Reference frame independence for the ROI dependent detection efficiency

The method to estimate the detection efficiency due to a ROI cut is based on the assumption of the independence of the spectral shape from the retarding potential. Both upper plots in figure C.1 show the comparison of the spectral shape measured by the FPD for different retarding potential. For comparison, each energy spectrum has been normalised to the maximum. By comparing the method for different reference frames with differing retarding potentials (illustrated in figure C.1a), using a fixed ROI for different frames of reference result in deviating detection efficiencies. The initial ROI bounds are illustrated by the dashed lines. By varying the lower limit of the ROI with the shift of the peak energy, deviations of the detection efficiency can be minimised to an acceptable level. Figure C.1b shows a reference frame independent method, with a variable lower ROI bound. In this particular case, the ROI has been set to an equivalent of [14.0 keV, 32.0 keV] for a 16 975 eV reference run, to be compliant with the detection efficiency used for the FT analysis. For different retarding potentials of the reference run, the lower bound has been adapted by the relative shift of the peak of the energy spectrum.

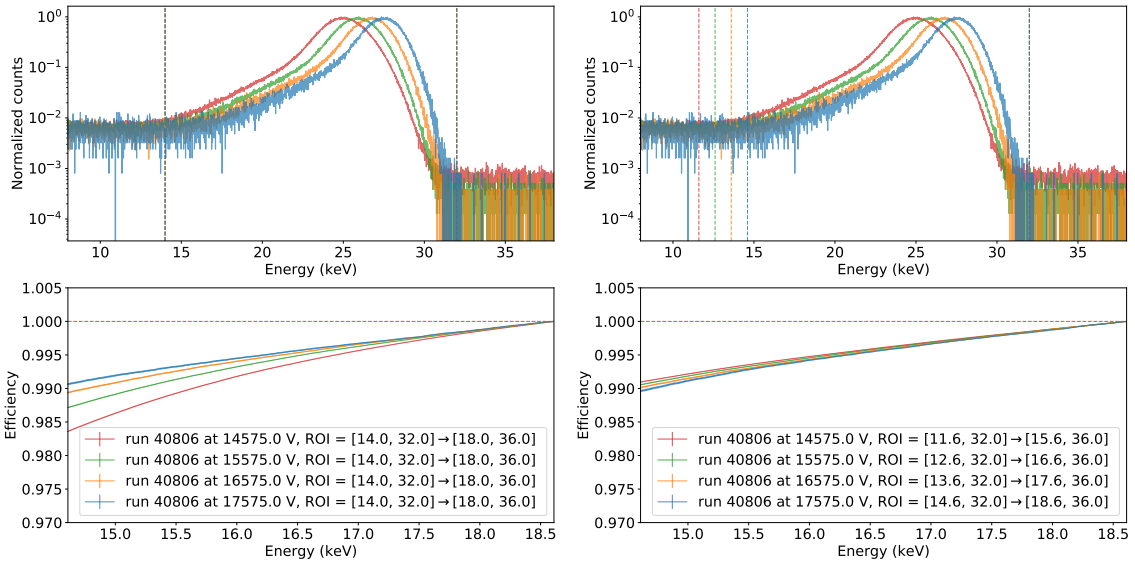

(a) Fixed bounds for ROI.

(b) Variable lower bound for ROI.

Figure C.1: (a) Calculated detection efficiency due to a ROI cut, using a fixed ROI. The plot legend each give information about the retarding potential, the initial ROI, as well as the shifted ROI, to calculate detection efficiency for the lowest energy (here 4 keV). Using a fixed ROI results in a reference frame dependent detection efficiency and gives a maxum differences $\sim 5\,\%$. **(b)** Calculated detection efficiency using a variable lower bound of the ROI. By variating the lower bound of the ROI, the influence of the reference frame is much smaller, and more in agreement.

D DT-fraction measured by LARA

Figure D.2 shows the LARA data given for both runs over time, as well as the DT-fraction for each sub-run. The Plot also shows the overall mean DT-concentration, as well as the standard deviation of the LARA data for each run.

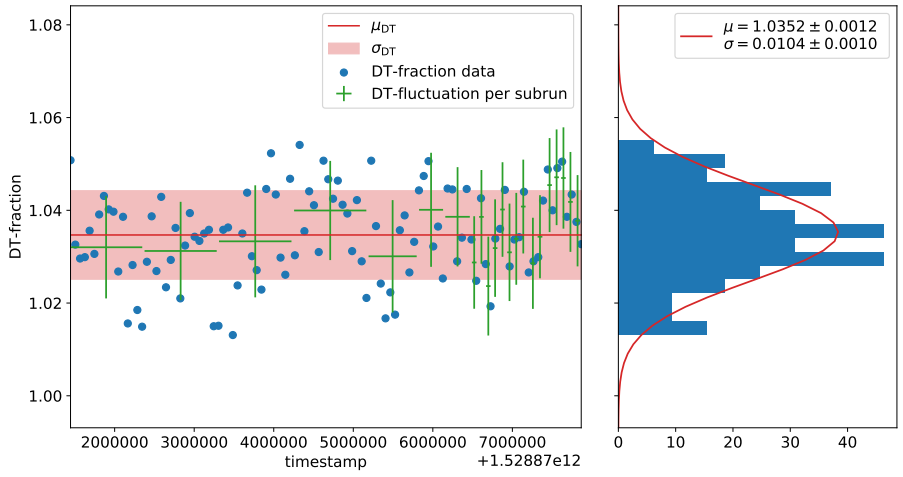

(a) Run 40773.

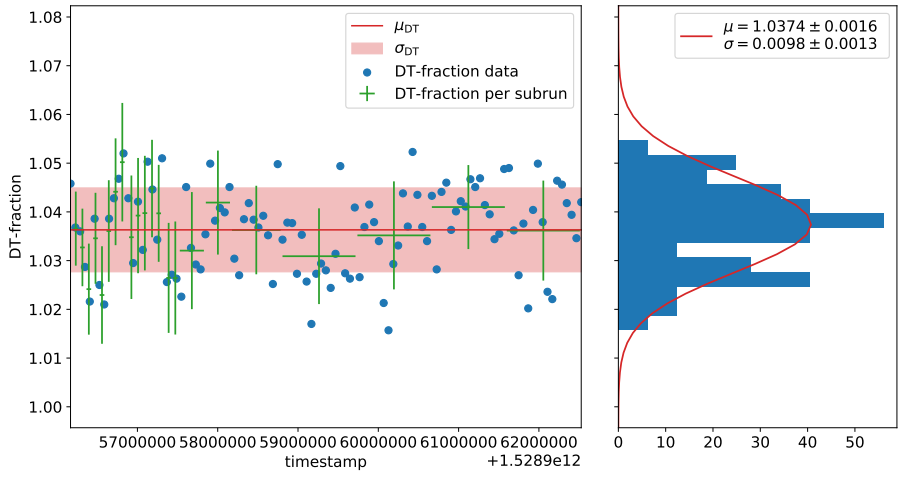

(b) Run 40806.

Figure D.2: DT-Fraction measured by LARA (blue) as well as the DT-Fraction of for each sub-run, and the statistical uncertainty on the DT-fraction used in the analysis (green). Histogram showing the DT-fluctuation within a single run ($\sim 1\,\%$).

E Correlation matrices for different systematic effects

Using the calculated covariance matrices V discussed in section 4.5.3 and shown in figure 4.7 and 4.8, the correlation matrices can be derived for each systematic effect. The correlation matrix ρ_{ij} entries are calculated as follows.

$$\rho_{ij} = \frac{V_{ij}}{\sqrt{V_{ii} \cdot V_{jj}}} \tag{E.1}$$

The following figures show the correlation matrices for all systematic effects, described in section 4.5.3. Furthermore, combining all systematic effects and calculating the correlation matrix leads to the correlation matrix, shown in figure E.5.

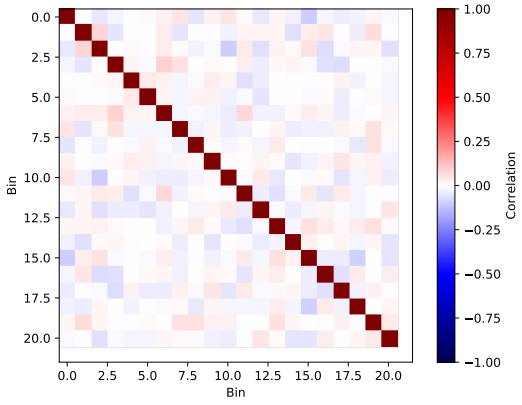

(a) Detection efficiency (pile-up).

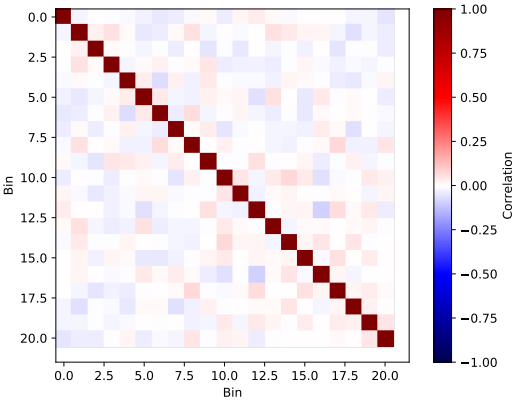

(b) Detection efficiency (ROI-cut).

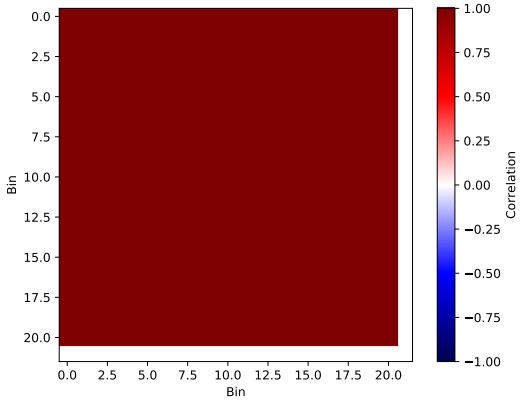

(c) B_{source}, B_{ana} and B_{max}.

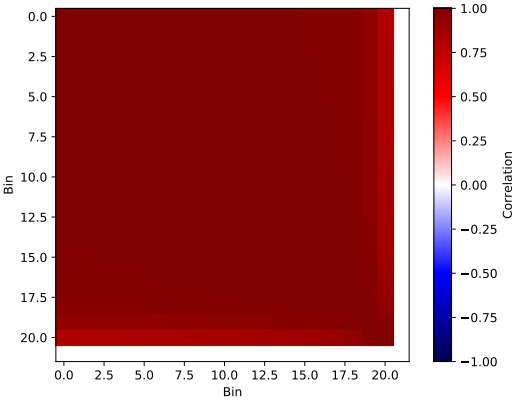

(d) Energy loss.

Figure E.3: Calculated correlation matrices for different systematic effects. **(a)** Correlation matrix assuming a systematic uncertainty on the detection efficiency including pile-up. **(b)** Correlation matrix assuming a systematic uncertainty on the detection efficiency due to a ROI-cut. **(c)** Correlation matrix assuming a 2.0 % uncertainty on the magnetic fields. **(d)** Correlation matrix assuming a systematic uncertainty on the energy loss function.

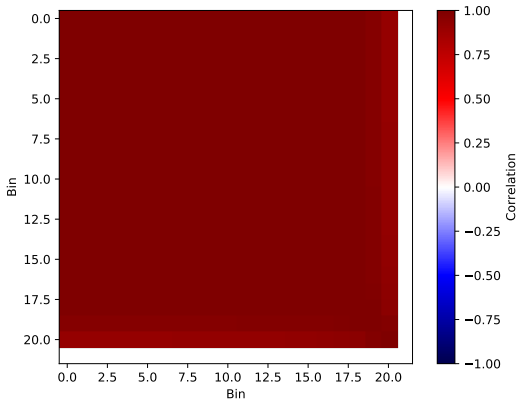

(a) FSD (bin-to-bin correlation).

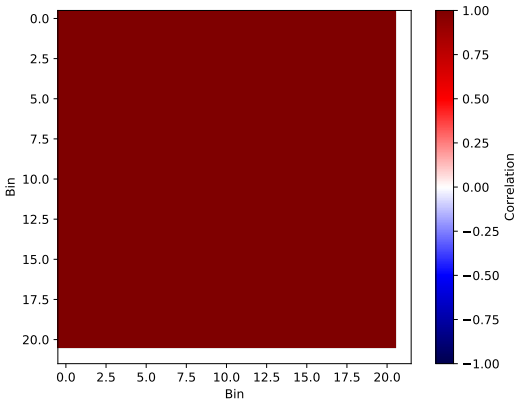

(b) FSD (onset).

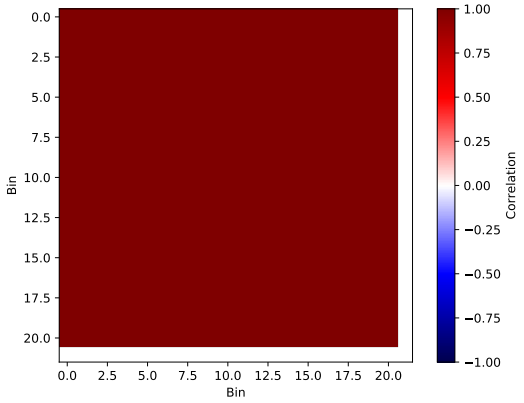

(c) $\rho \mathrm{d}\sigma$.

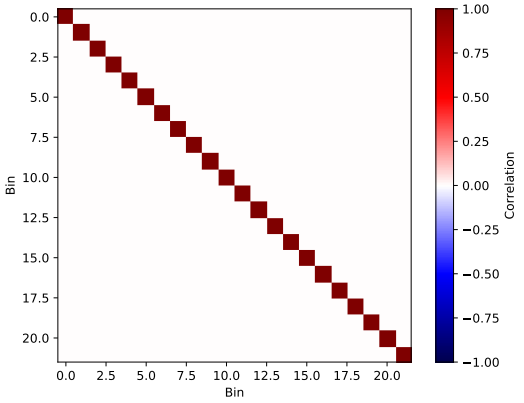

(d) DT-fluctuation.

Figure E.4: Calculated correlation matrices for different systematic effects. **(a)** Correlation matrix of the bin-to-bin correlation of the FSD. **(b)** Correlation matrix assuming an onset on the FSD. **(c)** Correlation for a systematic uncertainty of $\rho d = 5\,\%$ and $\sigma = 2\,\%$. **(d)** Correlation matrix for an bin-to-bin uncorrelated DT-fluctuation.

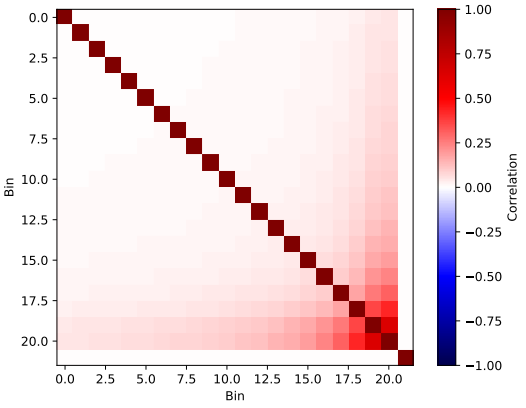

Figure E.5: Correlation matrix of all systematics combined, including detection efficiency

F Pixel-wise fit (run 40806)

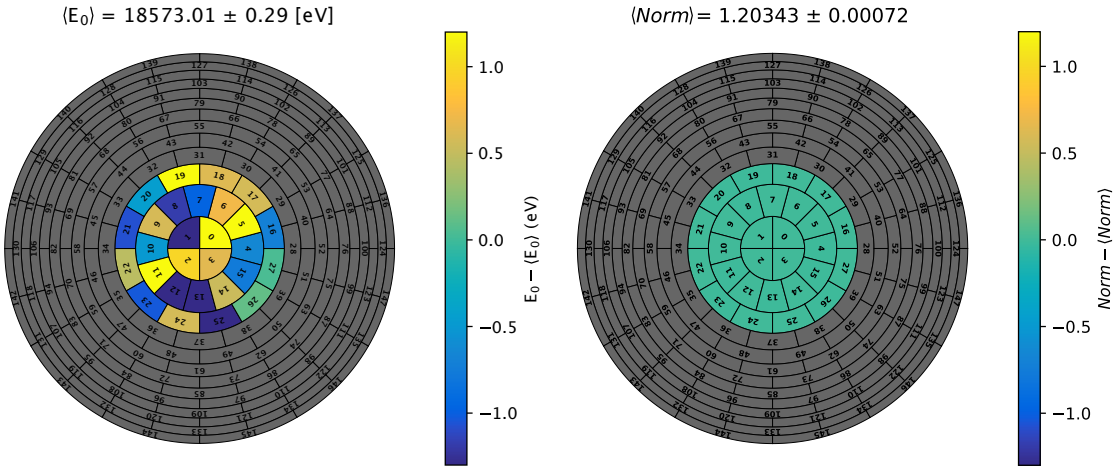

(a) Endpoint.

(b) Normalisation.

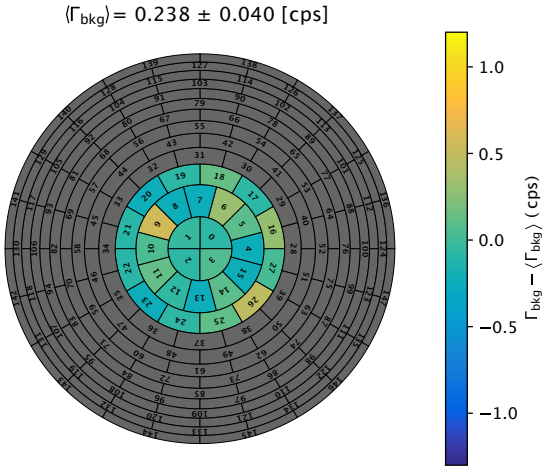

(c) Background.

Figure F.6: Pixel-wise fit of a FT run (run 40806) with reduced column density, measuring 4.0 keV deep into the spectrum. Each subfigure shows the pixel-wise fit results for **(a)** the endpoint E_0, **(b)** the normalisation, and **(c)** the background Γ_{bkg}. Each figure also gives the mean result of the fit parameter, as well as the variance of the fit results. Only the endpoint, normalisation and the background were fit. The neutrino mass squared was fixed to zero, as well as the sterile neutrino mass and the mixing amplitude. The pixel map shows no structures for the fit results of each parameter, and only small variations of the parameters.

List of acronyms

νMSM	**Neutrino** extended **m**inimal **s**tandard **m**odel
ASIC	**A**pplification-**s**pecific **i**ntegrated **c**ircuit
ATLAS	**A** **T**oroidal **L**HC **A**pparatu**s**
BFGS	**B**royden-**F**etcher-**G**oldfarb-**S**hanno
BIXS	**B**eta **i**nduced **X**-ray **s**pectrum
BooNE	**Boo**ster **N**eutrino **E**xperiment
CνB	**C**osmic **neutrino** **b**ackground
CAD	**C**omputer **a**ided **d**esign
CC	**C**harged **c**urrents
CDM	**C**old **d**ark **m**atter
CERN	**C**onseil **E**uropéen pour la **R**echerche **N**ucléaire
CL	**C**onfidence **l**evel
CMB	**C**osmic **m**icrowave **b**ackground
CMS	**C**ompact **M**uon **S**olenoid
CNGS	**C**ERN **n**eutrinos to **G**ran **S**asso
CNO	**C**arbon-**ni**trogen-**o**xigen
CP	**C**harge and **P**arity
CPS	**C**ryogenic **p**umping **s**ection
DAQ	**D**ata-**ac**q**u**isition
DONUT	**D**irect **o**bservation of the **nu** **t**au
DPS	**D**ifferential **p**umping **s**ection
EMCS	**E**arth **m**agnetic field **c**ompensation **s**ystem
ES	**E**lastic **s**cattering
FBM	**F**orward **b**eam **m**onitor
Fitrium	**Fi**t **trit**i**um**
FPD	**F**ocal **p**lane **d**etector
FSD	**F**inal **s**tate **d**istribution
FT	**F**irst **t**ritium
FT-ICR	**F**ourier **T**ransformation-**I**on **C**yclotron **R**esonator
FWHM	**F**ull **w**idth **h**alf **m**aximum
GERDA	**Ger**manium **D**etector **A**rray
GPU	**G**raphic **p**rocessing **u**nit

HDM	**H**ot **d**ark **m**atter
HLL	**H**albl**e**iter **L**abor
KamLAND	**Kam**ioka **L**iquid Scintillator **A**nti**n**eutrino **D**etector
KATRIN	**Ka**rlsruhe **Tri**tium **N**eutrino
KESS	**K**ATRIN **e**lectron **s**cattering in **s**ilicon
LARA	**La**ser **Ra**man
LFCS	**L**ow-**fi**eld **c**orrection **s**ystem
MAC-E	**M**agnetic-**a**diabatic **c**ollimation combined with an **e**lectrostatic
MINOS	**M**ain **I**njector **N**eutrino **O**scillation **S**earch
MPP	**M**ax-**P**lanck-Institut für **P**hysik
MS	**M**ain **s**pectrometer
MSSM	**M**inimal **s**upersymmetric **s**tandard **m**odel
MTD	**M**easurement **t**ime **d**istribution
NC	**N**eutral **c**urrents
OPERA	**O**scillation **P**roject with **E**mulsion **T**racking **A**pparatus
PAE	**P**ost **a**cceleration **e**lectrode
pdf	**P**robability **d**ensity **f**unction
PDG	**P**article **D**ata **G**roup
PIN	**P**ositive **i**ntrinsic **n**egative
PMNS	**P**ontecorvo-**M**aki-**N**akagawa-**S**akata
PS	**P**re-**s**pectrometer
RENO	**R**eactor **E**xperiment for **N**eutrino **O**scillation
ROI	**R**egion **o**f **i**nterest
RS	**R**ear **s**ection
SBL	**S**hort **B**ase **L**ine
SDD	**S**ilicon **d**rift **d**etector
SDS	**S**pectrometer and **d**etector **s**ection
SM	**S**tandard **m**odel
SNO	**S**udbury **N**eutrino **O**bservatory
STS	**S**ource and **t**ransport **s**ection
TRISTAN	**Tr**itium beta decay **i**nvestigation on **s**terile **t**o **a**ctive **n**eutrino mixing
WDM	**W**arm **d**ark **m**atter
WGTS	**W**indowless **g**aseous **t**ritium **s**ource
WIMP	**W**eakly **i**nteracting **m**assive **p**article
WMAP	**W**ilkinson **M**icrowave **A**nisotropy **P**robe

List of Figures

2.1 Feynman diagram of the inverse β-decay. 4
2.2 The standard model of elementary particle physics. 5
2.3 A depiction of the probability for neutrino oscillation. 7
2.4 Graphical representation of the neutrino mass hierarchy. 8
2.5 Results of solar neutrino flux measurements. 9
2.6 νMSM extension of the standard model. 12
2.7 Feynman diagram for the β^--decay. 13
2.8 Influence of the neutrino mass on the endpoint of the differential tritium spectrum. 14
2.9 Feynman diagram of a neutrinoless double β-decay 14
2.10 Simulated distribution of baryonic matter in regard to the neutrino mass. . 16
2.11 Halo simulations assuming the CDM as well as WDM. 17
2.12 Current constrains on a keV-scale sterile neutrino. 18
2.13 Imprint of a heavy sterile neutrino on the shape of the tritium decay spectrum. 19
2.14 Imprint of a heavy sterile neutrino on the ration of tritium decay spectra. . 19

3.1 Illustration of the working principle of a MAC-E filter. 22
3.2 Side view of the KATRIN experiment. 23
3.3 CAD model of the WGTS. 24
3.4 CAD model of the DPS2-F and the CPS. 25
3.5 Schematic illustration of the main spectrometer vessel. 27
3.6 The focal-plane detector system. 28
3.7 TRISTAN detector prototype and final TRISTAN detector layout. 30

4.1 MTD during the 4 keV sterile neutrino runs during the FT campaign. . . . 33
4.2 Plots of different components contributing the measured spectrum, such as the transmission function, the E-Loss model and the KATRIN response function. 35
4.3 Characteristics of the energy spectrum measured by the FPD. 38
4.4 Relative pixel-wise efficiency, scaled to the pixel with the highest count number. 42
4.5 Pixel-wise peak position in a high statistics stability run and Illustration of the method to estimate the energy dependent detection efficiency 43
4.6 Calculated energy dependent detection efficiency for each pixel. 44
4.7 Calculated covariance matrices used in this analysis 47
4.8 Calculated covariance matrices used in this analysis 48
4.9 Covariance matrix of all systematics combined 48
4.10 Pixel-wise fit of a FT run (run 40773) with reduced column density 50
4.11 Fit of the two 4 keV FT runs (run 40773 and run 40806) with reduced column density. 51
4.12 Calculated statistical sensitivity (90 % CL) for Monte Carlo datasets. 52
4.13 Calculated 90 % CL exclusion limit based on data. 53

4.14 Influence of systematics on the sensitivity. 54
4.15 Comparison of the exclusion limit with other experiments. 55

5.1 Illustration of the four dimensional ($n \times m \times i \times j$) response matrix. 58
5.2 Example spectrum for 10^6 mono-energetic ($E_{\text{initial}} = 26\,\text{keV}$) and mono angular ($\theta = 0°$) electrons. 60
5.3 Illustration of the detector response for all energy bins with the same $\cos(\theta)$-range. 60
5.4 Illustration of the detector response for angular bins within the same E_{initial}-range. 61
5.5 Example of a backscattering response, included in SSC-sterile. 62

C.1 Reference frame independence for the detection efficiency due to the ROI cut 67
D.2 DT-Fraction measured by LARA. 68
E.3 Calculated correlation matrices for different systematic effects. 69
E.4 Calculated correlation matrices for different systematic effects. 70
E.5 Correlation matrix of all systematics combined 70
F.6 Pixel-wise fit of a FT run (run 40806) with reduced column density 71

List of Tables

2.1 Summary of the results for the neutrino mixing parameters. 11
2.2 Summary of the results for the mass difference of the neutrino squared mass eigenstates 11

4.1 Settings for the sterile neutrino measurements. 32
4.2 Scale of systematic uncertainties used in this FT analysis for sterile neutrinos. 45

A.1 Overview of "first tritium" scans with reduced column density. 65
B.2 MTD for the 4.0 keV sterile neutrino runs during FT. 66

Bibliography

[1] Aalseth, C.E. *et al.*: *Search for neutrinoless double-β decay in ^{76}Ge with the majorana demonstrator*. Phys. Rev. Lett., 120:132502, Mar 2018. https://link.aps.org/doi/10.1103/PhysRevLett.120.132502.

[2] Abdurashitov, D. *et al.*: *Electron scattering on hydrogen and deuterium molecules at 14-25 keV by the "Troitsk nu-mass" experiment*. Mar. 2016. https://arxiv.org/pdf/1603.04243.

[3] Abdurashitov, J.N. *et al.*: *First measurements in search for keV sterile neutrino in tritium beta-decay in the Troitsk nu-mass experiment*. JETP Letters, 105(12):753–757, Jun 2017, ISSN 1090-6487. https://doi.org/10.1134/S0021364017120013.

[4] Abe, K. *et al.*: *Atmospheric neutrino oscillation analysis with external constraints in Super-Kamiokande I-IV*. Phys. Rev. D, 97:072001, Apr 2018. https://link.aps.org/doi/10.1103/PhysRevD.97.072001.

[5] Adhikari, R. et al.: *A White Paper on keV Sterile Neutrino Dark Matter*. 2016. http://arxiv.org/abs/1602.04816.

[6] Agarwal, S. and H.A. Feldman: *The effect of massive neutrinos on the matter power spectrum*. 2011MNRAS.410.1647A, June 2010. https://arxiv.org/pdf/1006.0689.

[7] Agostini, M. *et al.*: *Improved Limit on Neutrinoless Double-β Decay of ^{76}Ge from GERDA Phase II*. Phys. Rev. Lett., 120:132503, Mar 2018. https://link.aps.org/doi/10.1103/PhysRevLett.120.132503.

[8] Aguilar-Arevalo, A.A. *et al.*: *Search for Electron Neutrino Appearance at the $\Delta m^2 \sim 1$ eV^2 Scale*. Phys. Rev. Lett., 98:231801, Jun 2007. https://link.aps.org/doi/10.1103/PhysRevLett.98.231801.

[9] Altenmüller, K.: *Tristan measurements at troitsk with the cea system: final results*. 35th KATRIN Collaboration meeting, 2018.

[10] Amsbaugh, J. *et al.*: *Focal-plane detector system for the KATRIN experiment*. 2014. http://arxiv.org/abs/1404.2925.

[11] Aseev, V.N. *et al.*: *Energy loss of 18 keV electrons in gaseous T_2 and quench condensed D_2 films*. Eur. Phys. J. D, 10:39–52, 2000.

[12] ATLAS Collaboration: *Observation of a new particle in the search for the Standard Model Higgs boson with the ATLAS detector at the LHC*. Physics Letters B, 716(1):1 – 29, 2012, ISSN 0370-2693. http://www.sciencedirect.com/science/article/pii/S037026931200857X.

[13] Babutzka, M.: *Design and development for the Rearsection of the KATRIN experiment.* PhD thesis, Karlsruher Institut für Technologie (KIT), 2014. https://publikationen.bibliothek.kit.edu/1000045598.

[14] Babutzka, M. *et al.*: *Monitoring of the operating parameters of the KATRIN windowless gaseous tritium source.* New Journal of Physics, 14(10):103046, 2012.

[15] Bahcall, J.N., A.M. Serenelli, and S. Basu: *New Solar Opacities, Abundances, Helioseismology, and Neutrino Fluxes.* The Astrophysical Journal Letters, 621(1):L85, 2005. http://stacks.iop.org/1538-4357/621/i=1/a=L85.

[16] Bahcall, J.N. and R.K. Ulrich: *Solar models, neutrino experiments, and helioseismology.* Rev. Mod. Phys., 60:297–372, Apr 1988. https://link.aps.org/doi/10.1103/RevModPhys.60.297.

[17] Balázs, M.: *Neutrino Oscillation.* https://en.wikipedia.org/wiki/Neutrino_oscillation.

[18] Becquarel, H.: *The radio-activity of matter.* Nature, 63:396–398, 1901.

[19] Belesev, A. *et al.*: *Results of the troitsk experiment on the search for the electron antineutrino rest mass in tritium beta-decay.* Physics Letters B, 350(2):263 – 272, 1995, ISSN 0370-2693. http://www.sciencedirect.com/science/article/pii/037026939500335I.

[20] Bennett, C.L. *et al.*: *First Year Wilkinson Microwave Anisotropy Probe (WMAP) Observations: Preliminary Maps and Basic Results.* Astrophys.J.Suppl., 148:1, 2003. https://arxiv.org/pdf/astro-ph/0302207.

[21] Bennett, C.L. *et al.*: *Nine-year Wilkinson Microwave Anisotropy Probe (WMAP) observations: final maps and results.* The Astrophysical Journal Supplement Series, 208(2):20, 2013.

[22] Boyarsky, A. *et al.*: *Sterile neutrino dark matter.* July 2018. https://arxiv.org/pdf/1807.07938.

[23] BROYDEN, C.G.: *The Convergence of a Class of Double-rank Minimization Algorithms 1. General Considerations.* IMA Journal of Applied Mathematics, 6(1):76–90, Mar. 1970, ISSN 0272-4960. https://dx.doi.org/10.1093/imamat/6.1.76.

[24] Brunst, T.: *Tristan in troitsk: 3. update.* 2018.

[25] Chadwick, J.: *Intensitätsverteilung im magnetischen Spektrum von β-Strahlen von Radium B+C.* Verhandlungen der Deutschen Physikalischen Gesellschaft, 16:383–391, 1914.

[26] Chadwick, J.: *Possible existence of a neutron.* Nature, 129:313, 1932.

[27] Cleveland, B.T. *et al.*: *Measurement of the solar electron neutrino flux with the homestake chlorine detector.* The Astrophysical Journal, 496(1):505, 1998.

[28] CMS Collaboration: *Observation of a new particle in the search for the Standard Model Higgs boson with the ATLAS detector at the LHC.* Physics Letters B, 716(1):1 – 29, 2012.

[29] Danby, G. *et al.*: *Observation of high-energy neutrino reactions and the existence of two kinds of neutrinos.* Physical Review Letter, 9:36–44, Jul 1962. https://link.aps.org/doi/10.1103/PhysRevLett.9.36.

[30] Dawson, S.: *Introduction to electroweak symmetry breaking.* BNL-HET-99/1. https://arxiv.org/pdf/hep-ph/9901280.

[31] Dodelson, S. and L.M. Widrow: *Sterile Neutrinos as Dark Matter.* 1993.

[32] Doe, P.: *Status of the focal plane detector (FPD).* Presentation at the 15th KATRIN Collaboration Meeting, September 2008.

[33] Dolde, K. *et al.*: *Impact of adc non-linearities on the sensitivity to sterile kev neutrinos with a katrin-like experiment.* 2016.

[34] Dolde, K. *et al.*: *Impact of ADC non-linearities on the sensitivity to sterile keV neutrinos with a KATRIN-like experiment.* Nuclear Instruments and Methods in Physics Research Section A: Accelerators, Spectrometers, Detectors and Associated Equipment, 848(Supplement C):127 – 136, 2017, ISSN 0168-9002. http://www.sciencedirect.com/science/article/pii/S0168900216312761.

[35] DONUT Collaboration: *Observation of tau neutrino interactions.* Physics Letters B, 504(3):218 – 224, 2001, ISSN 0370-2693. http://www.sciencedirect.com/science/article/pii/S0370269301003070.

[36] Doss, N. and J. Tennyson: *Excitations to the electronic continuum of* $^3HeT^+$ *in investigations of* T_2 β*-decay experiments.* J. Phys. B, 41(12):125701+, 2008, ISSN 0953-4075.

[37] Doss, N. *et al.*: *Molecular effects in investigations of tritium molecule* β *decay endpoint experiments.* Physical Review C, 73:025502, 2006.

[38] Drewes, M. *et al.*: *A White Paper on keV Sterile Neutrino Dark Matter.* JCAP, 1701(01):025, 2017. http://arxiv.org/abs/1602.04816.

[39] Drexlin, G. *et al.*: *Current direct neutrino mass experiments.* Advances in High Energy Physics, 2013, 2013.

[40] Ellinger, E. *et al.*: *Monitoring the KATRIN source properties within the beamline.* Journal of Physics: Conference Series, 888(1):012229, 2017. http://stacks.iop.org/1742-6596/888/i=1/a=012229.

[41] Enomoto, S.: *Detection efficiency for first tritium.* Presentation at the KATRIN analysis workshop, 2018.

[42] Enomoto, S.: *Detector Count Corrections for First Tritium.* Internal KATRIN Report, 2019.

[43] Fermi, E.: *Versuch einer theorie der β-Strahlen.* Zeitschrift für Physik, 88(3–4):161–177, 1934.

[44] Fischer, S. *et al.*: *Monitoring of tritium purity during long-term circulation in the KATRIN test experiment LOOPINO using laser Raman spectroscopy.* Fusion Science and Technology, 60(3):925–930, 2011. http://www.ans.org/pubs/journals/fst/a_12567.

[45] Friedel, F. *et al.*: *Time dependent simulation of the flow reduction of D.* July 2018. https://arxiv.org/pdf/1807.10126v2.

[46] Fukuda, S. *et al.*: *The Super-Kamiokande detector.* Nuclear Instruments and Methods in Physics Research Section A: Accelerators, Spectrometers, Detectors and Associated Equipment, 501(2):418 – 462, 2003, ISSN 0168-9002. http://www.sciencedirect.com/science/article/pii/S016890020300425X.

[47] Förstner, E.: *Optimization of the KATRIN rear wallfor a keV-scale sterile neutrino search*, 2017.

[48] Gil, W. *et al.*: *The cryogenic pumping section of the KATRIN experiment*. IEEE Transactions on Applied Superconductivity, 20(3):316–319, 2010.

[49] Giunti, C. *et al.*: *Short-baseline electron neutrino oscillation length after troitsk*. Phys. Rev., D87(1):013004, 2013.

[50] Glück, F. *et al.*: *Electromagnetic design of the large-volume air coil system of the KATRIN experiment*. New Journal of Physics, 15(8):083025, 2013.

[51] Gninenko, S.N., D.S. Gorbunov, and M.E. Shaposhnikov: *Search for GeV-scale sterile neutrinos responsible for active neutrino oscillations and baryon asymmetry of the Universe*. Jan. 2013.

[52] Görhardt, S.: *Background Reduction Methods and Vacuum Technology at the KATRIN Spectrometers*. PhD thesis, Karlsruher Institut für Technologie (KIT), 2014. http://nbn-resolving.org/urn:nbn:de:swb:90-380506.

[53] Grohmann, S. *et al.*: *Precise temperature measurement at 30 K in the KATRIN source cryostat*. Cryogenics, 51(8):438–445, 2011.

[54] Group, P.D.: *Review of Particle Physics*. Phys. Rev. D, 98:030001, Aug 2018. https://link.aps.org/doi/10.1103/PhysRevD.98.030001.

[55] Gunion, J.F., D. Hooper, and B. McElrath: *Light Neutralino Dark Matter in the NMSSM*. Phys.Rev.D, 73:015011, 2006. https://arxiv.org/pdf/hep-ph/0509024.

[56] Hackenjos, M.: *Die differentielle pumpstrecke des KATRIN-experiments - inbetriebnahme und charakterisierung des supraleitenden magnetsystems*. Master thesis, Karlsruher Institut für Technologie (KIT), 2015. http://www.katrin.kit.edu/publikationen/MaT_Hackenjos.pdf.

[57] Harms, F.: *Assembly and first results of the KATRIN focal-plane detector system at KIT*. Diploma thesis, Karlsruher Institut für Technologie (KIT), 2012. http://www.katrin.kit.edu/publikationen/dth_Fabian_Harms.pdf.

[58] Harms, F.: *Characterization and Minimization of Background Processes in the KATRIN Main Spectrometer*. PhD thesis, Karlsruher Institut für Technologie (KIT), 2015. http://nbn-resolving.org/urn:nbn:de:swb:90-500274.

[59] Henning, R.: *Current status of neutrinoless double-beta decay searches*. Reviews in Physics, 1:29 – 35, 2016, ISSN 2405-4283. http://www.sciencedirect.com/science/article/pii/S2405428316000034.

[60] Hiddemann, K.H., H. Daniel, and O. Schwentker: *Limits on neutrino masses from the tritium beta spectrum*. J. Phys., G21:639–650, 1995.

[61] Hirata, K.S. *et al.*: *Real-time, directional measurement of* ^{8}B *solar neutrinos in the Kamiokande II detector*. Phys. Rev. D, 44:2241–2260, Oct 1991. https://link.aps.org/doi/10.1103/PhysRevD.44.2241.

[62] Holzschuh, E. *et al.*: *Search for heavy neutrinos in the beta spectrum of Ni-63*. Phys. Lett., B451:247–255, 1999.

[63] Houdy, T.: *Photography - TRISTAN SDD cube*, 2018.

[64] Huber, A.: *Search for kev-sterile neutrinos with katrin.* Master thesis, Karlsruher Institut für Technologie (KIT), 2015. https://www.katrin.kit.edu/publikationen/mth_huber_anton.pdf.

[65] Huber, A.: *Report on Adiabatic Transmission through the Main Spectrometer during the FT-Measurements.* Internal KATRIN Report, 2019.

[66] Jansen, A.: *The Cryogenic Pumping Section of the KATRIN Experiment - Design Studies and Experiments for the Commissioning.* PhD thesis, Karlsruher Institut für Technologie (KIT), 2015. http://nbn-resolving.org/urn:nbn:de:swb:90-471467.

[67] Kajita, T.: *Atmospheric neutrinos and discovery of neutrino oscillations.* Proceedings of the Japan Academy, Series B, 86(4):303–321, 2010.

[68] Kamiokande-II Collaboration: *Experimental Study of the Atmospheric Neutrino Flux.* Phys. Lett., B205:416, 1988.

[69] Karl, C.: *Analysis of First Tritium data of the KATRIN Experiment.* Master thesis, Technische Universtät München (TUM), 2018.

[70] Karl, C. *et al.*: *Dt fluctuation in first tritium data.* 2018.

[71] KATRIN collaboration: *KATRIN design report.* FZKA scientific report 7090, 2005. http://bibliothek.fzk.de/zb/berichte/FZKA7090.pdf.

[72] KATRIN collaboration: *First tritium.* in preparation.

[73] Kippenbrock, L.: *Electron peak position during penning trap measurements.* 2017.

[74] Kleesiek, M. *et al.*: *β-Decay Spectrum, Response Function and Statistical Model for Neutrino Mass Measurements with the KATRIN Experiment.* 2018. https://arxiv.org/abs/1806.00369.

[75] Korzeczek, M.: *ev & keV sterile neutrino studies with KATRIN.* Master thesis, Karlsruher Institut für Technologie (KIT), 2016. https://www.katrin.kit.edu/publikationen/MKorz-MA-eV-keV%20sterile%20Neutrinos.pdf.

[76] Kraus, C. *et al.*: *Final results from phase II of the mainz neutrino mass search in tritium β decay.* The European Physical Journal C - Particles and Fields, 40(4):447–468, 2005.

[77] Kraus, C. *et al.*: *Limit on sterile neutrino contribution from the Mainz Neutrino Mass Experiment.* Eur. Phys. J. C, 73:2323, 2013. https://arxiv.org/pdf/1210.4194.

[78] Kuckert, L.: *The Windowless Gaseous Tritium Source of the KATRIN Experiment – Characterisation of Gas Dynamical and Plasma Properties.* PhD thesis, Karlsruher Institut für Technologie (KIT), 2016. http://nbn-resolving.org/urn:nbn:de:swb:90-650776.

[79] Lovell, M.R. *et al.*: *The haloes of bright satellite galaxies in a warm dark matter universe.* Monthly Notices of the Royal Astronomical Society, 420(3):2318–2324, 2012. http://dx.doi.org/10.1111/j.1365-2966.2011.20200.x.

[80] Maki, Z., M. Nakagawa, and S. Sakata: *Remarks on the unified model of elementary particles.* Progress of Theoretical Physics, 28(5):870–880, 1962. http://dx.doi.org/10.1143/PTP.28.870.

[81] Marciano, W.J.: *Neutrino masses: Theory and experiment.* Comments Nucl. Part. Phys., 9(5):169–182, 1981.

[82] Mertens, S.: *Study of Background Processes in the Electrostatic Spectrometers of the KATRIN experiment.* PhD thesis, Karlsruher Institut für Technologie (KIT), 2012. http://nbn-resolving.org/urn:nbn:de:swb:90-270589.

[83] Mertens, S.: *Background Processes in the Electrostatic Spectrometers of the KATRIN Experiment.* Springer International Publishing, 2014, ISBN 978-3- 319-01176-9.

[84] Mertens, S. *et al.*: *A novel detector system for KATRIN to search for keV-scale sterile neutrinos.* Oct. 2018. https://arxiv.org/pdf/1810.06711.

[85] Miranda, O. and J. Valle: *Neutrino oscillations and the seesaw origin of neutrino mass.* Nuclear Physics B, 908:436 – 455, 2016, ISSN 0550-3213. http://www.sciencedirect.com/science/article/pii/S055032131630013X, Neutrino Oscillations: Celebrating the Nobel Prize in Physics 2015.

[86] MissMJ: *Standard Model of Elementary Particles.* https://en.wikipedia.org/wiki/Standard_Model.

[87] Nobel Media AB 2018: *The hunt for the muon neutrino.* https://www.nobelprize.org/prizes/physics/1988/9557-the-hunt-for-the-muon-neutrino/.

[88] Nobel Media AB 2018: *The Nobel Prize in Physics 2015 was awarded jointly to Takaaki Kajita and Arthur B. McDonald "for the discovery of neutrino oscillations, which shows that neutrinos have mass.".* https://www.nobelprize.org/prizes/physics/2015/press-release//.

[89] OPERA Collaboration: *Discovery of tau neutrino appearance in the CNGS neutrino beam with the OPERA experiment.* Phys. Rev. Lett., 115:121802, 2015. https://arxiv.org/pdf/1507.01417v1.

[90] P. A. R. Ade and *et al.*: *Planck2015 results.* Astronomy & Astrophysics, 594:A13, sep 2016. https://doi.org/10.1051/0004-6361/201525830.

[91] Patrignani, C. and P.D. Group: *Review of Particle Physics.* Chinese Physics C, 40(10):767–772, 2016. http://stacks.iop.org/1674-1137/40/i=10/a=100001.

[92] Pauli, W.E.F., R. Kronig, and V.F. Weisskopf: *Collected scientific papers.* Interscience, New York, NY, 1964. Offener Brief an die Gruppe der Radioaktiven bei der Gauvereinstagung zu Tübingen (datiert 4. Dez. 1930).

[93] Planck Collaboration: *Planck 2018 results. i. overview and the cosmological legacy of planck*, 2018. https://arxiv.org/abs/1807.06205.

[94] Pontecorvo, B.: *Mesonium and antimesonium.* Zhur. Eksptl'. i Teoret. Fiz., 33, 1957.

[95] Prall, M. *et al.*: *The KATRIN pre-spectrometer at reduced filter energy.* New Journal of Physics, 14(7):073054, 2012.

[96] Priester, F., M. Sturm, and B. Bornschein: *Commissioning and detailed results of KATRIN inner loop tritium processing system at tritium laboratory karlsruhe.* Vacuum, 116:42–47, 2015.

[97] Radford, D.: *Prototype 1 - final design options.* Presentation at the 32nd KATRIN Collaboration Meeting, 2017.

[98] Reines, F. and C.L. Cowan: *Detection of the free neutrino.* Physical Review, 92:830–831, 1953.

[99] Renschler, P.: *KESS - A new Monte Carlo simulation code for low-energy electron interactions in silicon detectors.* PhD thesis, Karlsruher Institut für Technologie (KIT), 2011. http://nbn-resolving.org/urn:nbn:de:swb:90-249597.

[100] Röllig, M. *et al.*: *Development of a compact tritium activity monitor and first tritium measurements.* Fusion Engineering and Design, 100(Supplement C):177 – 180, 2015, ISSN 0920-3796. http://www.sciencedirect.com/science/article/pii/S0920379615003531.

[101] Röllig, M. *et al.*: *Activity monitoring of a gaseous tritium source by beta induced X-ray spectrometry.* Fusion Engineering and Design, 88(6-8):1263–1266, 2013.

[102] Rutherford, E.: *Xv. the magnetic and electric deviation of the easily absorbed rays from radium.* The London, Edinburgh, and Dublin Philosophical Magazine and Journal of Science, 5(26):177–187, 1903.

[103] Saenz, A., S. Jonsell, and P. Froelich: *Improved molecular final-state distribution of HeT^+ for the β-decay process of T_2.* Physical Review Letters, 84:242–245, 2000.

[104] Salam, A.: *Weak and Electromagnetic Interactions.* Conf. Proc., C680519:367–377, 1968.

[105] Serenelli, A.: *Alive and well: A short review about standard solar models.* The European Physical Journal A, 52(4):78, Apr 2016, ISSN 1434-601X. https://doi.org/10.1140/epja/i2016-16078-1.

[106] SNO Collaboration: *Measurement of the rate of $\nu_e + d \rightarrow p + p + e^-$ interactions produced by ^8B solar neutrinos at the Sudbury Neutrino Observatory .* 2001. https://sno.phy.queensu.ca/sno/first_results/sno_first_results2.ps.

[107] SNO Collaboration: *Measurement of day and night neutrino energy spectra at sno and constraints on neutrino mixing parameters.* Phys. Rev. Lett., 89:011302, Jun 2002. https://link.aps.org/doi/10.1103/PhysRevLett.89.011302.

[108] The Borexino Collaboration: *Neutrinos from the primary proton–proton fusion process in the Sun.* Nature, 512:383–386, 2014. https://arxiv.org/abs/1507.02432.

[109] Tremaine, S. and J.E. Gunn: *Dynamical Role of Light Neutral Leptons in Cosmology.* Phys. Rev. Lett., 42:407–410, Feb 1979. https://link.aps.org/doi/10.1103/PhysRevLett.42.407.

[110] Ubieto Díaz, M.: *Off-line commissioning of a non-destructive FT-ICR detection system for monitoring the ion concentration in the KATRIN beamline.* PhD thesis, Ruperto-Carola University of Heidelberg, 2011. http://pubman.mpdl.mpg.de/pubman/item/escidoc:1255588:2/component/escidoc:1255587/2Ubieto_Thesis.pdf.

[111] Valerius, K.: *The wire electrode system for the KATRIN main spectrometer.* Progress in Particle and Nuclear Physics, 64(2):291–293, 2011. Neutrinos in Cosmology, in Astro, Particle and Nuclear Physics: International Workshop on Nuclear Physics, 31st course.

[112] Valerius, K. *et al.*: *Prototype of an angular-selective photoelectron calibration source for the KATRIN experiment.* Journal of Instrumentation, 6(1):P01002, 2011.

[113] Wandkowsky, N.: *Study of background and transmission properties of the KATRIN spectrometers*. PhD thesis, Karlsruher Institut für Technologie (KIT), 2013. http://nbn-resolving.org/urn:nbn:de:swb:90-366316.

[114] Wang, K.C.: *A suggestion on the detection of the neutrino*. Physical Review, 61:97–97, Jan 1942. https://link.aps.org/doi/10.1103/PhysRev.61.97.

[115] Weinberg, S.: *A model of leptons*. Phys. Rev. Lett., 19:1264–1266, Nov 1967. https://link.aps.org/doi/10.1103/PhysRevLett.19.1264.

[116] Zhang, J. and S. Zhou: *Relic Right-handed Dirac Neutrinos and Implications for Detection of Cosmic Neutrino Background*. 2015. https://arxiv.org/abs/1509.02274.

[117] Zwicky, F.: *Die Rotverschiebung von extragalaktischen Nebeln*. Helvetica Physica Acta, 6:110–127, 1933.

Acknowledgement

In the first instance I would like to thank Prof. Dr. Guido Drexlin for giving me the opportunity to be part of the KATRIN collaboration and to write my thesis at the KATRIN experiment.

I would also like to thank Prof. Dr. Susanne Mertens for the dedicated and friendly supervision. In all the discussions and from all the question that were asked I was able to learn a lot and enhance my research.

Furthermore I would like to thank:

- Anton Huber for the excellent and close supervision of my master thesis, who always had an open door whenever I ran into problems or had questions, and with whom it was a pleasure to work with. Additionally I would like to thank him for proof reading this thesis.
- Marc Korzeczek for his supervision as well and for always being happy to discuss and solve problems of any kind.
- Stephanie Hickford for proofreading this thesis and helping me with constructive and helpful ideas.
- Martin Slezák and Christian Karl, who were a major support regarding the Fitrium software and for providing the framework and answering my questions.
- Alexey Lokhov, with whom it was a pleasure to work with and who was always happy to explain and discuss physics models.
- Sanshiro Enomoto, for explaining in detail the many detector related effects.
- All people of the KATRIN climbing group, who shared my passion for climbing and for the after-climbing-beer.

Additionally I would like to thank all the people I worked within the KATRIN collaboration, for the friendly and enjoyable atmosphere.

Finally, I would like to thank my family for providing me with support and encouragement throughout my whole life and especially in the years during my studies. This accomplishment would have not been possible without their help. Thank you!